Received: Added at production | Revised: Added at production | Accepted: Added at production

DOI: xxx/xxxx

RESEARCH ARTICLE

Variational schemes and mixed finite elements for large strain isotropic elasticity in principal stretches: closed-form tangent eigensystems, convexity conditions and stabilised elasticity

Roman Poya[1] | Rogelio Ortigosa[2] | Antonio J. Gil[3]

[1]Siemens Digital Industries Software, Cambridge, United Kingdom
[2]Computational Mechanics and Scientific Computing Group, Technical University of Cartagena, Cartagena (Murcia), Spain
[3]Zienkiewicz Centre for Computational Engineering, Faculty of Science and Engineering, Swansea University, Swansea, United Kingdom

Correspondence
Roman Poya, Siemens Digital Industries Software, Cambridge, United Kingdom,
Email: roman.poya@siemens.com

Summary

A new computational framework for large strain elasticity in principal stretches is presented. Distinct from existing literature, the proposed formulation makes direct use of principal stretches rather than their squares i.e. eigenvalues of Cauchy-Green strain tensor. The proposed framework has three key features. First, the eigen-decomposition of the tangent elasticity and initial (geometric) stiffness operators is obtained in closed-form from principal information alone. Crucially, these newly found eigenvalues describe the general convexity conditions of isotropic hyperelastic energies. In other words, convexity is postulated concisely through tangent eigenvalues supplementing the original work of J. M. Ball[1]. Consequently, this novel finding opens the door for designing efficient automated Newton-style algorithms with stabilised tangents via *closed-form* semi-positive definite projection or spectral shifting that converge irrespective of mesh resolution, quality, loading scenario and without relying on path-following techniques. A critical study of closed-form tangent stabilisation in the context of isotropic hyperelasticity is therefore undertaken in this work. Second, in addition to high order displacement-based formulation, mixed Hu-Washizu variational principles are formulated in terms of principal stretches by introducing stretch work conjugate Lagrange multipliers that enforce principal stretch-stress compatibility. This is similar to enhanced strain methods. However, the resulting mixed finite element scheme is cost-efficient, specially compared to approximating the entire strain tensors since the formulation is in the scalar space of singular values. Third, the proposed framework facilitates simulating rigid and stiff systems and those that are nearly-inextensible in principal directions, a constituent of elasticity that cannot be easily studied using standard formulations.

KEYWORDS:
Large strain elasticity, principal stretches, convexity conditions, mixed finite elements

1 | INTRODUCTION

Large or finite strain elastic analysis by finite elements is now well established in many technical fields such as engineering analysis of materials and structures, study of soft biological tissues and simulation of purely animated response in computer

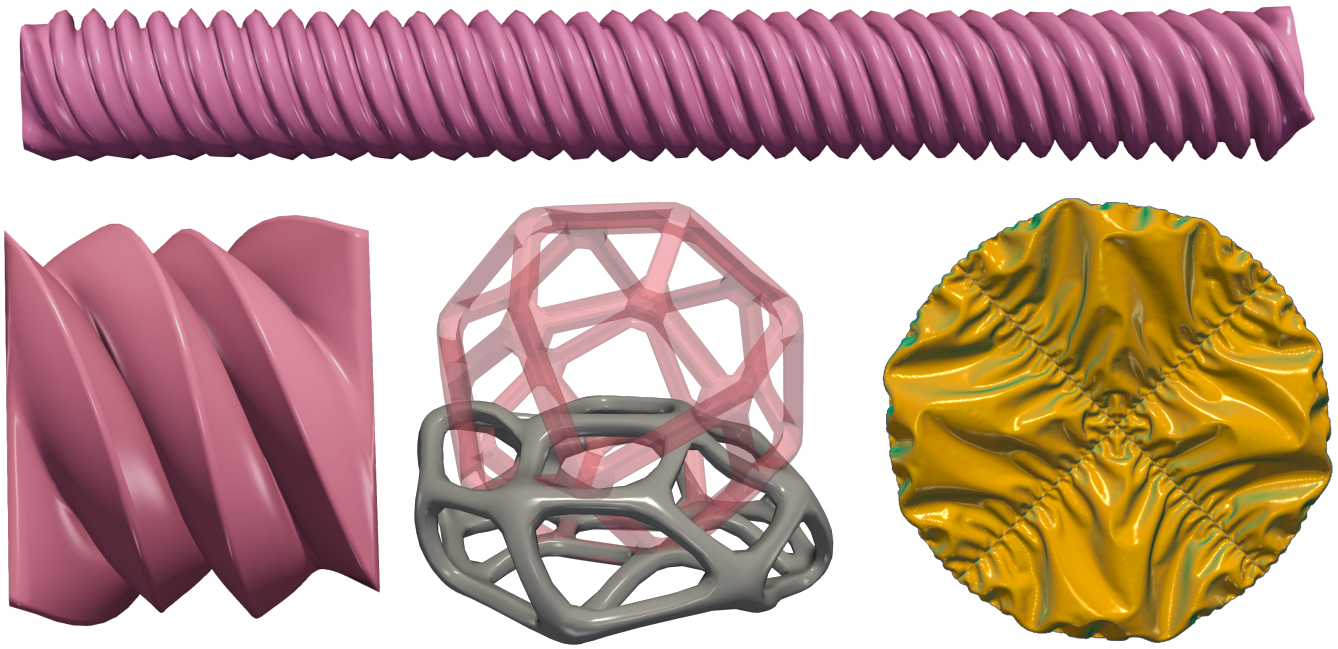

FIGURE 1 Selective examples of extreme deformations simulated using our proposed framework: infinite twist of a bar, slime morphing, complex buckling of a floating ball and wrinkling of an elastomeric sheet.

graphics, to name but a few. One aspect of large strain elasticity that has received considerable attention over the past is modelling of quasi-incompressible and truly incompressible media since many applications of practical interest happen in the quasi-incompressible regime. Away from quasi-incompressibility, computational aspects of large strain elasticity have received relatively less attention. In particular, two distinct issues still require further study, specifically in the nonlinear finite element community: 1) physically accurate and robust modelling of extreme deformations. Typically, a system is characterised to have undergone extreme deformation when the amount of displacements experienced by the system is orders of magnitude higher than the applied load[2]. A myriad of such examples can be found in nature such as the emergence of hierarchical wrinkles on elastomeric sheets and morphology of slime as seen in Fig. 1. Today's engineering and scientific simulation suites that are even equipped with continuation techniques and post-buckling analysis routines experience non-convergence when faced with such extreme deformations. 2) Simulation of *rigid*, *stiff* and *inextensible* systems. Like quasi-incompressibility, stiff materials have been traditionally modelled by decomposing the deformation into a rotation and a stretch component and by penalising the latter part[3]. Intuitively, and as studies in rigid body dynamics have shown, simulating stiff materials poses the same challenge as that of incompressibility, since rigidifying a deformable system through large penalty terms eventually either blows up the numerical routine and/or the accuracy of secondary variables, which reflects in stresses remains oscillatory or at best poor.

Recent advances in polyconvex large strain elasticity[4,5,6,7] provide a systematic way for designing strain energy functions that are *ab-initio* materially stable and hence, capable of modelling materials that can undergo extreme deformation. On one hand, polyconvexity guarantees both: 1) existence of real wave speeds within the medium, which has been shown to correspond to the fulfilment of Legendre-Hadamard condition, and 2) existence of unique minimisers when equipped with appropriate coercivity conditions[1]. On the other hand, polyconvexity eliminates all sources of constitutive instabilities which manifest themselves in the form of artefacts such as pathological mesh dependencies and visually odd-looking deformation patterns that emerge as a result of strain localisation. Polyconvexity is also a weaker restriction on strain energies implying that polyconvex energies can be easily constructed without limiting realistic response of the system. Material or constitutive instabilities are however, only one source of system instability. For systems undergoing extreme deformations, the other problematic source of instability (from a computational point of view), typically emanates from the structure itself, and is commonly known as geometric instability. Examples of geometric instability include, buckling, snap-throughs, wrinkles and pull-ins or a complex combination of these.

Models that preclude geometric instabilities are often too limiting. It is well known that indiscriminately pruning instabilities from material models leave out only linear and convex energies. Convexity (as opposed to polyconvexity) is a much stronger

and significantly hard-to-meet requirement for real-world applications. Lack of convexity (or non-convexity) on the other hand, leads to even more challenging numerical issues particularly in the context of second-order computational methods (such as Newton-Raphson like schemes) that take advantage of the Hessians and tangent operators since (in)-definiteness of the tangents dictates (non)-convergence of the nonlinear solvers. Traditionally, overcoming convergence issues while solving for non-convex problems has been tackled numerically after finite element discretisation and not in the smooth setting. Multiple techniques have been designed in this regard but, it is worth mentioning the two most powerful categories of techniques. In the first category lie path-following techniques and arc-length-based methods, which are typically employed by commercial finite element packages[8,9,10,11]. Generally, arc-length methods retain the quadratic convergence of Newton but they are hard to automate for complex deformation scenarios and across different finite element mesh resolutions. Manually modifying loading patterns is a common task between stress analysts in the FEA industry. The second category comprises of more prudent techniques as they modify the underlying energy and/or its derivatives through the commonly known technique called tangent stabilisation. Many stabilisation techniques have been proposed in the literature with some merits and shortcomings. Generally, stabilisation techniques drop the quadratic convergence of Newton in favour of a fully automated minimisation routine. However, they still remain second order (depending on the technique) in convergence. A rather simple but popular form of tangent stabilisation is Laplacian stabilisation employed for instance in ANSYS[8] and in many other works[12,13]. A more sophisticated tangent stabilisation technique, which to the best our knowledge was first advocated by Teran et. al.[14] in the context of nonlinear elasticity, is the notion of projection of tangent operators to semi-positive definite (SPD) cone. Originally, such projection relied on per-element numerical eigen-decomposition by clamping the negative eigenvalues of tangent operator to a small positive number ϵ. A plethora of projection techniques have since been proposed for hyperelastic energies[15,16,17,13,18,19,20]. Amongst these, the most powerful method is the one recently presented in[20], which obtains the tangent and initial stiffness operators eigen-decomposition in closed-form and in essence, comes cost-free. Finally, it is worth mentioning that, dynamic simulations have also been used as a means of stabilisation as the inclusion of always-positive inertia (mass) and damping (viscosity) terms stabilises the tangent[21,22,23,24]. However, such techniques in general do not guarantee that the tangent operators are always semi-positive definite and non-convergence is still expected. Moreover, they are mesh dependent in that, the time step has to be significantly decreased with mesh resolution.

Tangent stabilised large strain elasticity also finds application in many new promising fields away from engineering simulations, specifically in areas where elasticity is used as an analogy, for instance, in curved high order meshing[17,16,25], mesh smoothing and grid generation[26], surface parametrisation[18] and volumetric polycube parametrisation[27], to name but a few. In fact, many of these applications require only the constitutive tangent operator that is responsible for minimising certain distortion metrics, and the initial (geometric) terms are often discarded entirely.

In addition to the aforementioned issue, an area less studied in the nonlinear finite elements of solids is modelling of partially rigid and stiff (close-to-rigid) systems. Partially rigid systems (i.e. systems that are rigid in one or less than d principal direction(s)) in general cannot be modelled using strain invariants such as Cauchy-Greens. Nor can they be described in terms of the usual squares of principal stretches (i.e. eigen-values of Cauchy-Green), as rigidity constraint is linear in principal stretches. As mentioned earlier, penalty style techniques that enforce rigidity often lead to numerical issues similar to that of incompressibility. Intuitive numerical judgement suggests that rigid and stiff systems require Hu-Washizu-style mixed formulations in each principal direction. As will be discussed, our proposed formulation makes it particularly easy to simulate such systems.

This work describes a novel framework for large strain elasticity in principal stretches. The point of departure and a critical component of our formulation is the Singular-Value-Decomposition (SVD) of the deformation gradient tensor from which principal stretches are obtained. We then show that, knowing the principal stretches it is possible to obtain concise *closed-form* formula for the eigen-decomposition of both constitutive tangent operator and initial (geometric) stiffness operator. To this end, we start with the recently introduced stretch tensor invariants of Smith, B. et. al.[20] whose ingredients facilitate concise formulation for large strain elasticity in principal stretches without relying on SVD differentials. However, the realisation is that gradient and Hessian of energies when expressed in terms of singular-values are even simpler than those obtained through stretch tensor invariants. In fact, as will be shown later, the eigenvalues of tangent elasticity and initial stiffness operators obtained through our workflow are precisely the characterisation of convexity for isotropic hyperelastic energies. Our workflow has multiple novel features: 1) if a displacement-based formulation is desired, then numerical perturbation of the deformation gradient is avoided in case of equal principal stretches as performed in other works[28,29,30], and 2) the closest to our work and to the best of our knowledge the only other formulation of large strain elasticity directly in terms of principal stretches of the deformation gradient tensor appears in the work of Xu et. al.[29] for computer graphics applications, which relies on SVD differentials. In particular, the aforementioned work relies on numerically solving multiple 2×2 matrices for the directional derivatives of left and right singular matrices. Such SVD differentials are bypassed, unnecessary and contrary to the goal of our formulation. Due to

this numerical treatment, the work of[29] completely missed the notion of finding tangent eigen-decomposition from principal stretches. As a result, efforts to find analytic eigensystems using this line of work appear to be bolt-on[31] and missing the crucially revealing linkage to the underlying convexity conditions of energy. Furthermore, this formulation was developed for linear triangle/tetrahedral meshes to the point that the formulation cannot be easily decoupled from its corresponding discretisation. Our formulation is noticeably cleaner, and generalises to general polyhedral and arbitrary high order finite element meshes.

Having established the bases for large strain elasticity formulation in principal stretches suitable for standard displacement-based formulation, we further develop a series of mixed Hu-Washizu variational principles. More specifically, two further variational principles are presented namely: 1) a 7-field (5-field in 2-dimensions) mixed formulation by considering each principal stretch as a variable and introducing their energetically work conjugates and by imposing their compatibility through standard Lagrange multipliers. This results in a formulation similar to enhanced strain methods usually developed to alleviate bending and volumetric lockings. However, in addition to alleviating such locking phenomena, this formulation also accurately models rigidity and in-extensibility in principal directions, and 2) An initially 4-field (3-field in 2-dimensions) displacement-stretch formulation which further reduces to a simple formulation for truly rigid models suitable for rigid body simulations.

It is worth mentioning that, finite element simulations based on stretch formulations for finitely deformable solids have become more common in geometry processing applications and specifically in surface parametrisation[29,32,18,33]. In this regard, a set of popular algorithms have emerged over the past two decades commonly referred to as the "local-global“ algorithms[34,35,33,3,36]. On cursory examination, these algorithms have a noteworthy resemblance to P1-P0 mixed finite elements wherein displacements and rotations (from the polar decomposition of deformation gradient) are treated as separate variables. The rotations are then solved locally (discontinuously from a mixed variational formulation point of view) and displacements are solved globally. However, closer inspection reveals that these algorithms have emerged rather as a work-around for energies that explicitly feature the rotation tensor (in order to avoid its directional derivatives) than a full-fledged mixed variational formulation for rotation accurate analyses. In that, these algorithms cannot be recast as a second-order (e.g. Newton-Raphson) minimisation problem as rotations and displacements are solved in alternating fashion. Hence, they are at best first order staggered algorithms. Once again, given the application area, they are all designed for linear simplicial meshes which make them unsuitable for engineering simulation purposes. Moreover, when seen from a mixed variational formulation point, the stability of linear-constant ansatz functions for such displacement-rotation discretisations is not clear and has never been studied[37,38,39,40,41]. Our mixed variational framework in fact also formalises these approaches and provides a second-order alternative to them.

To summarise, the proposed framework introduces the following key contributions:

- A new formulation for large strain isotropic elasticity based on principal stretches (and not their squares).
- Closed-form eigensystems for both constitutive tangent and initial stiffness operators determined solely from principal information and consequently an optional tangent stabilisation technique to tackle extreme deformations beyond the onset of geometrical instabilities.
- High order displacement based and mixed Hu-Washizu variational formulations (and the subsequent finite element implementations) by treating principal stretches as independent variables and enforcing principal stretch-stress compatibility through additional Lagrange multipliers for locking-free and stress-accurate analyses.

The structure of the paper is as follows. In Section. 2, the mapping and kinematics of motion is introduced, followed by the ingredients that make up our formulation, mainly the SVD and polar decomposition of deformation gradient and how the principal stretches are obtained. Here, we briefly review the stretch tensor invariants of[20], the directional derivatives of principal stretches and explicit forms of tangent and initial stiffness operators. In Section. 3, we review general convexity conditions and other restrictions imposed on assumed strain energies such as growth conditions and coercivity which are critical to our development. We also lay out the tangent stabilisation strategy in this section. In Section. 4, the various variational principals described earlier are presented. Section. 5, describes finite element discretisation of the variational principles. The standard displacement-based formulation is discretised using arbitrary high order finite elements, whereas suitable finite element spaces are considered for the corresponding mixed formulations. In Section. 6, we describe a generalised Newton-Raphson procedure with a line search scheme that encompasses both standard Newton-Raphson and Quasi-Newton techniques such as Projected Newton and Modified Newton, tailored for simulating extreme deformation scenarios and the choice quadrature rules for further guaranteeing semi-positive definiteness in nonlinear elastic simulations. Various numerical examples are presented in Section. 7. Finally Section. 8 concludes the paper.

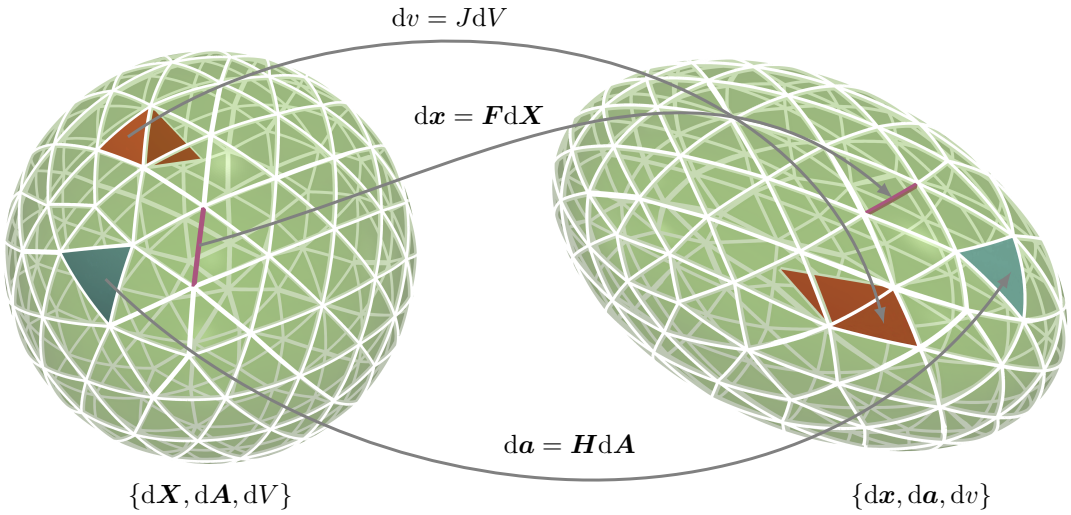

FIGURE 2 Mapping original and deformed configurations and fundamental kinematic measures of motion in $\mathbb{R}^3$ Euclidean space. $\{\boldsymbol{F}, \boldsymbol{H}, J\}$ map edges, areas and volumes from original $\{\mathrm{d}\boldsymbol{X}, \mathrm{d}\boldsymbol{A}, \mathrm{d}V\}$ to deformed $\{\mathrm{d}\boldsymbol{x}, \mathrm{d}\boldsymbol{a}, \mathrm{d}v\}$ configuration, respectively.

2 | CONTINUUM MECHANICS PRELIMINARIES

2.1 | Motion and deformation

Consider the 3-dimensional deformation of an elastic medium from its initial configuration occupying a volume V, of boundary ∂V, into a final configuration at volume v, of boundary ∂v (see Fig. 2). Following Bonet et. al.[4,5] the standard notation and definitions for fundamental kinematic measures namely, the deformation gradient $\boldsymbol{F}$, its cofactor $\boldsymbol{H}$ and its determinant J are used [1]

$$\boldsymbol{F} = \frac{\partial \boldsymbol{x}}{\partial \boldsymbol{X}} = \boldsymbol{\nabla}_0 \boldsymbol{x}, \quad \boldsymbol{H} = J\boldsymbol{F}^{-T} = \frac{1}{2}\boldsymbol{F} \times \boldsymbol{F}, \quad J = \det \boldsymbol{F}. \tag{1}$$

where $\boldsymbol{x}$ represents the current position of a particle originally at $\boldsymbol{X}$ and $\boldsymbol{\nabla}_0$ denotes the gradient with respect to material coordinates and $\times$ is the tensor cross product operator $[\boldsymbol{A} \times \boldsymbol{B}]_{ij} = \mathcal{E}_{ijk}\mathcal{E}_{IJK}A_{jJ}B_{kK}$ where $\mathcal{E}$ is the third order Levi-Civita tensor[42,5]. Virtual and incremental variations of $\boldsymbol{x}$ will be denoted by $\delta\boldsymbol{u}$ and $\Delta\boldsymbol{u}$, respectively. It is assumed that $\boldsymbol{x}, \delta\boldsymbol{u}$ and $\Delta\boldsymbol{u}$ satisfy appropriate displacement based boundary conditions in $\partial_u V$. Additionally, the body is under the action of certain body forces per unit undeformed volume $\boldsymbol{f}_0$ and traction per unit undeformed area $\boldsymbol{t}_0$ in $\partial_t V$, where $\partial_t V \cup \partial_u V = \partial V$ and $\partial_t V \cap \partial_u V = \emptyset$. Crucial to our development is the left polar decomposition of the deformation gradient tensor

$$\boldsymbol{F} = \boldsymbol{R}\boldsymbol{U}, \tag{2}$$

into a rotation tensor $\boldsymbol{R}$ and a stretch tensor $\boldsymbol{U}$. This decomposition is often obtained from the Singular-Value-Decomposition (SVD) of $\boldsymbol{F}$ as follows

$$\boldsymbol{F} = \hat{\boldsymbol{U}}\boldsymbol{\Lambda}\hat{\boldsymbol{V}}^T, \quad \boldsymbol{R} = \hat{\boldsymbol{U}}\hat{\boldsymbol{V}}^T, \quad \boldsymbol{U} = \hat{\boldsymbol{V}}\boldsymbol{\Lambda}\hat{\boldsymbol{V}}^T, \tag{3}$$

where $\hat{\boldsymbol{U}}$ and $\hat{\boldsymbol{V}}$ are orthogonal tensors namely left and right singular-matrices, respectively and the tensor $\boldsymbol{\Lambda}$ encodes the singular-values of $\boldsymbol{F}$ i.e. the principal stretches namely $\lambda_1 \geq \lambda_2 \geq \lambda_3 \geq 0$ such that $\lambda_i = \Lambda_{ii}$ (we have used the symbol $\hat{\boldsymbol{U}}$ for left singular matrix (and accordingly $\hat{\boldsymbol{V}}$ for right singular matrix) to distinguish with the stretch tensor $\boldsymbol{U}$). Note that, in mechanics

[1] Unless stated otherwise, throughout this work, lower case bold letters ($\boldsymbol{a}$) denote vectors, capital bold letters ($\boldsymbol{A}$) second order tensors and capital blackboard-bold letters ($\mathbb{A}$) fourth order tensors. Calligraphic letters ($\mathcal{A}$) are used to represent tangent elasticity operators, λ_is are used to denote the singular-values of the deformation gradient tensor (i.e. principal stretches) and $\bar{\lambda}_i$s are used to denote the eigenvalues of Hessian and tangent elasticity operators. Square brackets around bold letters with subscripts such as ($[N]_i$) indicate distinct vectors/tensors spanning in d-dimensional space as opposed to indices of the stated vector/tensor (N_i).

literature, the more standard definition for the stretch tensor $\boldsymbol{U}$ appears as

$$\boldsymbol{U} = \sum_{i=1}^{d} \lambda_i [\boldsymbol{N}]_i \otimes [\boldsymbol{N}]_i, \tag{4}$$

where $[\boldsymbol{N}]_i$ are the material principal directions in fact corresponding to the columns of $\hat{\boldsymbol{V}}$ which is obtained from the SVD and d denotes the Euclidean space dimension (i.e. 1,2,3). It follows that, the deformation gradient tensor $\boldsymbol{F}$ can be expressed alternatively as

$$\boldsymbol{F} = \sum_{i=1}^{d} \lambda_i [\boldsymbol{n}]_i \otimes [\boldsymbol{N}]_i, \tag{5}$$

where $[\boldsymbol{n}]_i$ are the spatial principal directions obtained from push-forward operation $[\boldsymbol{n}]_i = \boldsymbol{R}[\boldsymbol{N}]_i$.

2.2 | An overview of stretch tensor invariants

To facilitate the development of large strain elasticity formulation directly in terms of principal stretches (as opposed to their squares) it is necessary to first highlight the *stretch tensor invariants*. Recently, in Smith. B et. al.[20] a new set of invariants for nonlinear mechanics were introduced. These invariants are simply the trace, Frobenius norm (double contraction) and the determinant of the stretch tensor $\boldsymbol{U}$, respectively, in that,

$$I_1 = \mathrm{tr}(\boldsymbol{U}) = \sum_{i=1}^{d} \lambda_i, \quad I_2 = \boldsymbol{U} : \boldsymbol{U} = \boldsymbol{F} : \boldsymbol{F} = \sum_{i=1}^{d} \lambda_i^2, \quad I_5 = \det \boldsymbol{U} = J = \prod_{i=1}^{d} \lambda_i. \tag{6}$$

Remark 1. Since orthogonality dictates that, $[\boldsymbol{N}]_i \cdot [\boldsymbol{N}]_i = 1$ and $\det(\hat{\boldsymbol{V}}) = 1$ the stretch tensor invariants work out as

$$I_1 = \mathrm{tr}(\boldsymbol{U}) = \boldsymbol{U} : \boldsymbol{I} = \sum_{i=1}^{d} \lambda_i [\boldsymbol{N}]_i \cdot [\boldsymbol{N}]_i = \sum_{i=1}^{d} \lambda_i, \tag{7a}$$

$$I_2 = \boldsymbol{U} : \boldsymbol{U} = \sum_{i=1}^{d} \lambda_i ([\boldsymbol{N}]_i \cdot [\boldsymbol{N}]_i) \lambda_i ([\boldsymbol{N}]_i \cdot [\boldsymbol{N}]_i) = \sum_{i=1}^{d} \lambda_i^2, \tag{7b}$$

$$I_5 = \det(\boldsymbol{U}) = \det\left(\hat{\boldsymbol{V}} \boldsymbol{\Lambda} \hat{\boldsymbol{V}}^T\right) = \det(\boldsymbol{\Lambda}) = \prod_{i=1}^{d} \lambda_i. \tag{7c}$$

It is important to note that, compared to the more traditional invariants (such as Cauchy-Green $\boldsymbol{C} = \boldsymbol{F}^T \boldsymbol{F}$) used in nonlinear mechanics the stretch tensor invariants are "low-order" in that, I_1 being the sum of singular-values is linear in $\boldsymbol{F}$ and in essence represents a linear strain measure and I_2 is the first invariant of Cauchy-Green $I_2 = I_C = \boldsymbol{C} : \boldsymbol{I}$. To incorporate the remaining Cauchy-Green invariants and in light of the polyconvex strain measures $\{\boldsymbol{F}, \boldsymbol{H}, J\}$[6,4,5,43] Poya et. al.[44] further introduced the extended stretch tensor invariants family which also included the cofactor invariants as follows

$$I_3 = \mathrm{tr}(\boldsymbol{U}_{\boldsymbol{H}}) = \sum_{i,j;i\neq j}^{d} \lambda_i \lambda_j, \quad I_4 = \boldsymbol{H} : \boldsymbol{H} = \sum_{i,j;i\neq j}^{d} \lambda_i^2 \lambda_j^2, \tag{8}$$

where $\boldsymbol{U}_{\boldsymbol{H}}$ is the stretch tensor of the cofactor $\boldsymbol{H}$ in that the following relationships hold

$$\boldsymbol{H} = \hat{\boldsymbol{U}} \boldsymbol{\Lambda}_{\boldsymbol{H}} \hat{\boldsymbol{V}}^T = \boldsymbol{R} \boldsymbol{U}_{\boldsymbol{H}}; \qquad \boldsymbol{U}_{\boldsymbol{H}} = J \boldsymbol{U}^{-1}; \qquad \Lambda_{H_{ii}} = \Lambda_{ii}^{-1} \prod_{j=1}^{d} \lambda_j = J \Lambda_{ii}^{-1}, \tag{9}$$

Revealing that, the polar decomposition of $\boldsymbol{H}$ is already available given the polar decomposition of $\boldsymbol{F}$ since $\boldsymbol{F}$ and $\boldsymbol{H}$ are coaxial. Further note that, I_4 represents the second Cauchy-Green invariant i.e. $I_4 = I I_C = I_5 \boldsymbol{C}^{-1} : \boldsymbol{I}$. As presented in[44], the two cofactor invariants are however redundant in 2-dimensions since $\boldsymbol{H} : \boldsymbol{I} = \boldsymbol{F} : \boldsymbol{I}$ and $\boldsymbol{H} : \boldsymbol{H} = \boldsymbol{F} : \boldsymbol{F}$ hence, $I_3 = I_1$ and $I_4 = I_2$ and in 3-dimensions they can be expressed as a combination of the other three invariants as

$$I_3 = \frac{1}{2}(I_1^2 - I_2), \tag{10a}$$

$$I_4 = I_3^2 - 2 I_1 I_5. \tag{10b}$$

The first directional derivative of these invariants with respect to geometry changes can be obtained in a straight-forward fashion. The most important one which would be used heavily in our development is the first and second directional derivatives of I_1 [20]

$$D I_1[\delta \boldsymbol{u}] = \boldsymbol{R} : \boldsymbol{\nabla}_0 \delta \boldsymbol{u}, \tag{11}$$

which reveals that the first directional derivative of I_1 yields the rotation tensor $\boldsymbol{R}$ itself. Similarly, the second directional derivative follows [20]

$$D^2 I_1[\delta \boldsymbol{u}, \Delta \boldsymbol{u}] = \boldsymbol{\nabla}_0 \delta \boldsymbol{u} : \mathbb{T}_{\boldsymbol{R}} : \boldsymbol{\nabla}_0 \Delta \boldsymbol{u}, \tag{12}$$

where $\mathbb{T}_{\boldsymbol{R}}$ is to be defined below. Critical to the development of stretch tensor invariants in [20] was the discovery that rotation gradients are orthogonal to the deformation gradient tensor ($\frac{\partial \boldsymbol{R}}{\partial \boldsymbol{F}} : \boldsymbol{F} = \boldsymbol{0}$) which led to novel concise expressions for derivatives and rates of rotation and stretch tensors. Such Gateaux derivatives had previously been found to be forbiddingly long and complex to numerically implement [45,46,47,48]. In particular, the fourth order tensor $\mathbb{T}_{\boldsymbol{R}}$ has the following succinct form

$$\mathbb{T}_{\boldsymbol{R}} = \frac{\partial \boldsymbol{R}}{\partial \boldsymbol{F}} = \sum_{i=1}^{k} \bar{\lambda}_i [\boldsymbol{T}]_i \otimes [\boldsymbol{T}]_i, \quad \text{where} \quad k = 1 \text{ in 2D}; \;\; k = 3 \text{ in 3D} \tag{13}$$

such that

$$[\boldsymbol{T}]_1 = \frac{1}{\sqrt{2}} \hat{\boldsymbol{U}} \begin{bmatrix} 0 & -1 \\ 1 & 0 \end{bmatrix} \hat{\boldsymbol{V}}^T, \quad \text{in 2D,} \tag{14a}$$

$$[\boldsymbol{T}]_1 = \frac{1}{\sqrt{2}} \hat{\boldsymbol{U}} \begin{bmatrix} 0 & 0 & 0 \\ 0 & 0 & -1 \\ 0 & 1 & 0 \end{bmatrix} \hat{\boldsymbol{V}}^T, \quad [\boldsymbol{T}]_2 = \frac{1}{\sqrt{2}} \hat{\boldsymbol{U}} \begin{bmatrix} 0 & 0 & -1 \\ 0 & 0 & 0 \\ 1 & 0 & 0 \end{bmatrix} \hat{\boldsymbol{V}}^T, \quad [\boldsymbol{T}]_3 = \frac{1}{\sqrt{2}} \hat{\boldsymbol{U}} \begin{bmatrix} 0 & -1 & 0 \\ 1 & 0 & 0 \\ 0 & 0 & 0 \end{bmatrix} \hat{\boldsymbol{V}}^T, \quad \text{in 3D,} \tag{14b}$$

where $[\boldsymbol{T}]_i$s are called the *twist* tensors and the corresponding eigenvalues $\bar{\lambda}$ are

$$\bar{\lambda}_1 = \frac{2}{\lambda_1 + \lambda_2} \quad \text{in 2D,} \tag{15a}$$

$$\bar{\lambda}_1 = \frac{2}{\lambda_2 + \lambda_3}, \quad \bar{\lambda}_2 = \frac{2}{\lambda_1 + \lambda_3} \quad \bar{\lambda}_3 = \frac{2}{\lambda_1 + \lambda_2}, \quad \text{in 3D.} \tag{15b}$$

As will be discussed in the next section, the analytic eigensystem of *all* isotropic hyperelastic energies feature the structure of tensor $\mathbb{T}_{\boldsymbol{R}}$.

2.3 | Directional derivatives of principal stretches

With the above algebra we have essentially obtained the directional derivatives of rotation and stretch tensors. This information is critical as it allows us to formulate problems directly in terms of principal stretches. The directional derivatives of principal stretches can now be obtained in a straight-forward fashion. In 2-dimensions the first directional derivatives take the form

$$D\lambda_1[\delta \boldsymbol{u}] = \frac{\partial \lambda_1}{\partial \boldsymbol{F}} : \boldsymbol{\nabla}_0 \delta \boldsymbol{u}, \qquad \frac{\partial \lambda_1}{\partial \boldsymbol{F}} = [\boldsymbol{n}]_1 \otimes [\boldsymbol{N}]_1 = \hat{\boldsymbol{U}} \begin{bmatrix} 1 & 0 \\ 0 & 0 \end{bmatrix} \hat{\boldsymbol{V}}^T \tag{16a}$$

$$D\lambda_2[\delta \boldsymbol{u}] = \frac{\partial \lambda_2}{\partial \boldsymbol{F}} : \boldsymbol{\nabla}_0 \delta \boldsymbol{u}, \qquad \frac{\partial \lambda_2}{\partial \boldsymbol{F}} = [\boldsymbol{n}]_2 \otimes [\boldsymbol{N}]_2 = \hat{\boldsymbol{U}} \begin{bmatrix} 0 & 0 \\ 0 & 1 \end{bmatrix} \hat{\boldsymbol{V}}^T \tag{16b}$$

and similarly in 3-dimensions

$$D\lambda_1[\delta \boldsymbol{u}] = \frac{\partial \lambda_1}{\partial \boldsymbol{F}} : \boldsymbol{\nabla}_0 \delta \boldsymbol{u}, \qquad \frac{\partial \lambda_1}{\partial \boldsymbol{F}} = [\boldsymbol{n}]_1 \otimes [\boldsymbol{N}]_1 = \hat{\boldsymbol{U}} \begin{bmatrix} 1 & 0 & 0 \\ 0 & 0 & 0 \\ 0 & 0 & 0 \end{bmatrix} \hat{\boldsymbol{V}}^T \tag{17a}$$

$$D\lambda_2[\delta \boldsymbol{u}] = \frac{\partial \lambda_2}{\partial \boldsymbol{F}} : \boldsymbol{\nabla}_0 \delta \boldsymbol{u}, \qquad \frac{\partial \lambda_2}{\partial \boldsymbol{F}} = [\boldsymbol{n}]_2 \otimes [\boldsymbol{N}]_2 = \hat{\boldsymbol{U}} \begin{bmatrix} 0 & 0 & 0 \\ 0 & 1 & 0 \\ 0 & 0 & 0 \end{bmatrix} \hat{\boldsymbol{V}}^T \tag{17b}$$

$$D\lambda_3[\delta \boldsymbol{u}] = \frac{\partial \lambda_3}{\partial \boldsymbol{F}} : \boldsymbol{\nabla}_0 \delta \boldsymbol{u}, \qquad \frac{\partial \lambda_3}{\partial \boldsymbol{F}} = [\boldsymbol{n}]_3 \otimes [\boldsymbol{N}]_3 = \hat{\boldsymbol{U}} \begin{bmatrix} 0 & 0 & 0 \\ 0 & 0 & 0 \\ 0 & 0 & 1 \end{bmatrix} \hat{\boldsymbol{V}}^T \tag{17c}$$

Notice that, the derivatives $\frac{\partial \lambda_i}{\partial \boldsymbol{F}}$ include simple rank-one (only one non-zero column) *scaling* tensors which are indeed useful in the study of rank-one convexity. From above equations it is apparent that principal stretches are linear in $\boldsymbol{F}$. The second directional derivatives can be worked out further in 2-dimensions as

$$D^2\lambda_1[\delta\boldsymbol{u};\Delta\boldsymbol{u}] = \boldsymbol{\nabla}_0\delta\boldsymbol{u} : \frac{\partial^2\lambda_1}{\partial\boldsymbol{F}\partial\boldsymbol{F}} : \boldsymbol{\nabla}_0\Delta\boldsymbol{u}, \qquad \frac{\partial^2\lambda_1}{\partial\boldsymbol{F}\partial\boldsymbol{F}} = \frac{1}{\lambda_1-\lambda_2}\left(\bar{\mathbb{I}} - \lambda_2\mathbb{T}_{\boldsymbol{R}}\right), \tag{18a}$$

$$D^2\lambda_2[\delta\boldsymbol{u};\Delta\boldsymbol{u}] = \boldsymbol{\nabla}_0\delta\boldsymbol{u} : \frac{\partial^2\lambda_2}{\partial\boldsymbol{F}\partial\boldsymbol{F}} : \boldsymbol{\nabla}_0\Delta\boldsymbol{u}, \qquad \frac{\partial^2\lambda_2}{\partial\boldsymbol{F}\partial\boldsymbol{F}} = \frac{-1}{\lambda_1-\lambda_2}\left(\bar{\mathbb{I}} - \lambda_1\mathbb{T}_{\boldsymbol{R}}\right). \tag{18b}$$

Similarly in 3-dimensions we obtain

$$D^2\lambda_1[\delta\boldsymbol{u};\Delta\boldsymbol{u}] = \boldsymbol{\nabla}_0\delta\boldsymbol{u} : \frac{\partial^2\lambda_1}{\partial\boldsymbol{F}\partial\boldsymbol{F}} : \boldsymbol{\nabla}_0\Delta\boldsymbol{u}, \quad \frac{\partial^2\lambda_1}{\partial\boldsymbol{F}\partial\boldsymbol{F}} = \frac{1}{(\lambda_1-\lambda_2)(\lambda_1-\lambda_3)}\left(\lambda_1\bar{\mathbb{I}} - (\lambda_1\lambda_2+\lambda_1\lambda_3)\mathbb{T}_{\boldsymbol{R}} + \mathbb{H}_{\boldsymbol{J}}\right), \tag{19a}$$

$$D^2\lambda_2[\delta\boldsymbol{u};\Delta\boldsymbol{u}] = \boldsymbol{\nabla}_0\delta\boldsymbol{u} : \frac{\partial^2\lambda_2}{\partial\boldsymbol{F}\partial\boldsymbol{F}} : \boldsymbol{\nabla}_0\Delta\boldsymbol{u}, \quad \frac{\partial^2\lambda_2}{\partial\boldsymbol{F}\partial\boldsymbol{F}} = \frac{-1}{(\lambda_1-\lambda_2)(\lambda_2-\lambda_3)}\left(\lambda_2\bar{\mathbb{I}} - (\lambda_1\lambda_2+\lambda_2\lambda_3)\mathbb{T}_{\boldsymbol{R}} + \mathbb{H}_{\boldsymbol{J}}\right), \tag{19b}$$

$$D^2\lambda_3[\delta\boldsymbol{u};\Delta\boldsymbol{u}] = \boldsymbol{\nabla}_0\delta\boldsymbol{u} : \frac{\partial^2\lambda_2}{\partial\boldsymbol{F}\partial\boldsymbol{F}} : \boldsymbol{\nabla}_0\Delta\boldsymbol{u}, \quad \frac{\partial^2\lambda_2}{\partial\boldsymbol{F}\partial\boldsymbol{F}} = \frac{1}{(\lambda_1-\lambda_3)(\lambda_2-\lambda_3)}\left(\lambda_3\bar{\mathbb{I}} - (\lambda_1\lambda_3+\lambda_2\lambda_3)\mathbb{T}_{\boldsymbol{R}} + \mathbb{H}_{\boldsymbol{J}}\right), \tag{19c}$$

where $\bar{\mathbb{I}}$ is a simple fourth order tensor $\bar{\mathbb{I}} = \mathbb{I} - \sum_{i=1}^{d}\frac{\partial\lambda_i}{\partial\boldsymbol{F}}\otimes\frac{\partial\lambda_i}{\partial\boldsymbol{F}}$ (where $\mathbb{I}$ is the fourth order identity tensor, with $[\mathbb{I}]_{iIjJ} = \delta_{iI}\delta_{jJ}$, where δ_{ab} represents the ab-th component of the Kronecker delta tensor) and $\mathbb{H}_{\boldsymbol{J}} = \mathbb{I}\times\boldsymbol{F}$ is the Hessian of $J = I_5$. Note that, the above relationships are obtained in a straight-forward fashion by realising that

$$\frac{\partial^2 I_1}{\partial\boldsymbol{F}\partial\boldsymbol{F}} = \frac{\partial^2\left(\lambda_1+\lambda_2+\lambda_3\right)}{\partial\boldsymbol{F}\partial\boldsymbol{F}} = \mathbb{T}_{\boldsymbol{R}}; \quad \frac{\partial^2 I_2}{\partial\boldsymbol{F}\partial\boldsymbol{F}} = \frac{\partial^2\left(\lambda_1^2+\lambda_2^2+\lambda_3^2\right)}{\partial\boldsymbol{F}\partial\boldsymbol{F}} = 2\mathbb{I}; \quad \frac{\partial^2 I_5}{\partial\boldsymbol{F}\partial\boldsymbol{F}} = \frac{\partial^2\left(\lambda_1\lambda_2\lambda_3\right)}{\partial\boldsymbol{F}\partial\boldsymbol{F}} = \mathbb{H}_{\boldsymbol{J}}. \tag{20}$$

As will be revealed later however, these second directional derivatives can be expressed alternatively in a more concise form via an analytic eigen-decomposition.

2.4 | Isotropic large strain elasticity in principal stretches

There is often a set of fundamental mathematical requirements that must be satisfied by admissible strain energy functions used to describe elastic materials in the large strain regime. One such requirement is polyconvexity which dictates that, the strain energy e per unit undeformed volume must be a function of the deformation gradient $\boldsymbol{F}$ via a convex multi-variable function W such as

$$e(\boldsymbol{\nabla}_0\boldsymbol{x}) = \hat{W}(\boldsymbol{F},\boldsymbol{H},J) \tag{21}$$

where $\hat{W}$ is convex with respect to its 19 variables, namely, J and the 3×3 components of $\boldsymbol{F}$ and $\boldsymbol{H}$. Suitable formulations and numerical implementations have been developed for polyconvex elasticity for instance in Bonet. et. al.[4,5]. To facilitate our development, it is desirable to start with *ab-initio* polyconvex energies such as $\hat{W}$, to be then re-expressed in terms of principal stretches, taking advantage of the isotropy of the material. In what follows, we work out the directional derivatives of these re-expressed energies in a 3-dimensional Euclidean space and then give out the general expressions in d-dimensions in boxed equations. Following this rationale, an energy $W(\lambda_1,\lambda_2,\lambda_3)$ can be expressed as

$$e(\boldsymbol{\nabla}_0\boldsymbol{x}) = \hat{W}(\boldsymbol{F},\boldsymbol{H},J) = W(\lambda_1,\lambda_2,\lambda_3) = W(\mathcal{A}), \tag{22}$$

where for brevity we have defined the set of principal stretches as $\mathcal{A} = \{\lambda_1,\cdots,\lambda_d\}$. Furthermore, a set of work conjugate stresses $\mathcal{S} = \{\Sigma_{\lambda_1},\cdots,\Sigma_{\lambda_d}\}$ can be introduced for each principal stretch such that

$$\Sigma_{\lambda_1} = \frac{\partial W}{\partial\lambda_1}, \quad \Sigma_{\lambda_2} = \frac{\partial W}{\partial\lambda_2}, \quad \Sigma_{\lambda_3} = \frac{\partial W}{\partial\lambda_3}. \tag{23}$$

The conjugate stresses defined above can now be used to obtain the more standard first Piola-Kirchhoff stress tensor $\boldsymbol{P}$. To do so, recall first that the first Piola-Kirchoff tensor is defined by the equation

$$De[\delta\boldsymbol{u}] = \boldsymbol{P} : \boldsymbol{\nabla}_0\delta\boldsymbol{u}; \qquad \boldsymbol{P} = \left.\frac{\partial e}{\partial\boldsymbol{F}}\right|_{\boldsymbol{F}=\boldsymbol{\nabla}_0\boldsymbol{x}}. \tag{24}$$

With the help of theses equations, the chain rule and Eqns. 16-17 it is possible to express the virtual internal work as

$$\begin{aligned}\boldsymbol{P} : \boldsymbol{\nabla}_0\delta\boldsymbol{u} &= De[\delta\boldsymbol{u}] \\ &= DW[D\lambda_1[\delta\boldsymbol{u}], D\lambda_2[\delta\boldsymbol{u}], D\lambda_3[\delta\boldsymbol{u}]] \\ &= \Sigma_{\lambda_1}\frac{\partial\lambda_1}{\partial\boldsymbol{F}} : \boldsymbol{\nabla}_0\delta\boldsymbol{u} + \Sigma_{\lambda_2}\frac{\partial\lambda_2}{\partial\boldsymbol{F}} : \boldsymbol{\nabla}_0\delta\boldsymbol{u} + \Sigma_{\lambda_3}\frac{\partial\lambda_3}{\partial\boldsymbol{F}} : \boldsymbol{\nabla}_0\delta\boldsymbol{u} \\ &= \left(\Sigma_{\lambda_1}\frac{\partial\lambda_1}{\partial\boldsymbol{F}} + \Sigma_{\lambda_2}\frac{\partial\lambda_2}{\partial\boldsymbol{F}} + \Sigma_{\lambda_3}\frac{\partial\lambda_3}{\partial\boldsymbol{F}}\right) : \boldsymbol{\nabla}_0\delta\boldsymbol{u}. \end{aligned} \tag{25}$$

which leads to the evaluation of the first Piola-Kirchhoff tensor in d-dimensions as

$$\boxed{\boldsymbol{P} = \sum_{i=1}^{d}\Sigma_{\lambda_i}\frac{\partial\lambda_i}{\partial\boldsymbol{F}} = \sum_{i=1}^{d}\Sigma_{\lambda_i}[\boldsymbol{n}]_i \otimes [\boldsymbol{N}]_i = \hat{\boldsymbol{U}}\boldsymbol{\Lambda}_{\boldsymbol{P}}\hat{\boldsymbol{V}}^T} \tag{26}$$

where $\Lambda_{P_{ii}} = \Sigma_{\lambda_i}$ is the diagonal principal stress tensor revealing that, the first Piola Kirchhoff stress tensor $\boldsymbol{P}$ is coaxial with $\boldsymbol{F}$. In the context of second order optimisation methods, such as Newton-Raphson-like schemes, the tangent elasticity operator is also often required. To evaluate this, first recall that, the fourth order tangent elasticity tensor is defined as

$$D^2e[\delta\boldsymbol{u};\Delta\boldsymbol{u}] = \boldsymbol{\nabla}_0\delta\boldsymbol{u} : D\boldsymbol{P}[\Delta\boldsymbol{u}] = \boldsymbol{\nabla}_0\delta\boldsymbol{u} : \boldsymbol{C} : \boldsymbol{\nabla}_0\Delta\boldsymbol{u}; \qquad \boldsymbol{C} = \left.\frac{\partial\boldsymbol{P}}{\partial\boldsymbol{F}}\right|_{\boldsymbol{F}=\boldsymbol{\nabla}_0\boldsymbol{x}} = \left.\frac{\partial^2 e}{\partial\boldsymbol{F}\partial\boldsymbol{F}}\right|_{\boldsymbol{F}=\boldsymbol{\nabla}_0\boldsymbol{x}}. \tag{27}$$

With the help of theses equations, the chain rule and Eqns. 18-19 and further using Eqn. 26 we obtain:

$$\begin{aligned} D^2e[\delta\boldsymbol{u};\Delta\boldsymbol{u}] &= \boldsymbol{\nabla}_0\delta\boldsymbol{u} : D\boldsymbol{P}[\Delta\boldsymbol{u}] \\ &= \left(\Sigma_{\lambda_1}\frac{\partial\lambda_1}{\partial\boldsymbol{F}} : \boldsymbol{\nabla}_0\delta\boldsymbol{u}\right)D\Sigma_{\lambda_1}[\Delta\boldsymbol{u}] + \left(\Sigma_{\lambda_2}\frac{\partial\lambda_2}{\partial\boldsymbol{F}} : \boldsymbol{\nabla}_0\delta\boldsymbol{u}\right)D\Sigma_{\lambda_2}[\Delta\boldsymbol{u}] + \left(\Sigma_{\lambda_3}\frac{\partial\lambda_3}{\partial\boldsymbol{F}} : \boldsymbol{\nabla}_0\delta\boldsymbol{u}\right)D\Sigma_{\lambda_3}[\Delta\boldsymbol{u}] \\ &+ \boldsymbol{\nabla}_0\delta\boldsymbol{u} : \left(\Sigma_{\lambda_1}\frac{\partial^2\lambda_1}{\partial\boldsymbol{F}\partial\boldsymbol{F}} + \Sigma_{\lambda_2}\frac{\partial^2\lambda_2}{\partial\boldsymbol{F}\partial\boldsymbol{F}} + \Sigma_{\lambda_3}\frac{\partial^2\lambda_3}{\partial\boldsymbol{F}\partial\boldsymbol{F}}\right) : \boldsymbol{\nabla}_0\Delta\boldsymbol{u}. \end{aligned} \tag{28}$$

In general, the above equation can be grouped into two set of terms namely, the first derivatives and the second derivatives of energy

$$\begin{aligned} D^2e[\delta\boldsymbol{u};\Delta\boldsymbol{u}] = \left[\left(\frac{\partial\lambda_1}{\partial\boldsymbol{F}} : \boldsymbol{\nabla}_0\delta\boldsymbol{u}\right), \left(\frac{\partial\lambda_2}{\partial\boldsymbol{F}} : \boldsymbol{\nabla}_0\delta\boldsymbol{u}\right), \left(\frac{\partial\lambda_3}{\partial\boldsymbol{F}} : \boldsymbol{\nabla}_0\delta\boldsymbol{u}\right)\right][\boldsymbol{H}_W]\begin{bmatrix}\left(\frac{\partial\lambda_1}{\partial\boldsymbol{F}} : \boldsymbol{\nabla}_0\Delta\boldsymbol{u}\right)\\ \left(\frac{\partial\lambda_2}{\partial\boldsymbol{F}} : \boldsymbol{\nabla}_0\Delta\boldsymbol{u}\right)\\ \left(\frac{\partial\lambda_3}{\partial\boldsymbol{F}} : \boldsymbol{\nabla}_0\Delta\boldsymbol{u}\right)\end{bmatrix} \\ + \boldsymbol{\nabla}_0\delta\boldsymbol{u} : \left(\sum_{i=1}^{3}\Sigma_{\lambda_i}\frac{\partial^2\lambda_i}{\partial\boldsymbol{F}\partial\boldsymbol{F}}\right) : \boldsymbol{\nabla}_0\Delta\boldsymbol{u} \end{aligned} \tag{29}$$

where $\boldsymbol{H}_W$ denotes the $d\times d$ Hessian operator containing the second derivatives of W with respect to principal stretches which by Clairaut's theorem is always symmetric

$$\boldsymbol{H}_W = \begin{bmatrix}\frac{\partial^2 W}{\partial\lambda_1\partial\lambda_1} & \cdots & \frac{\partial^2 W}{\partial\lambda_1\partial\lambda_d}\\ & \ddots & \vdots \\ sym & & \frac{\partial^2 W}{\partial\lambda_d\partial\lambda_d}\end{bmatrix}. \tag{30}$$

and the last term in Eqn. 29 is the "initial stress" term. In comparison to the fourth order Hessian operator that emerges in polyconvex formulations in terms $\{\boldsymbol{F},\boldsymbol{H},J\}$ (see Bonet et. al.[4] for instance) the above operator is only second order and hence simpler to understand its structure. Eqn. 29 leads to the evaluation of total elasticity operator as an algebraic summation of

constitutive $\boldsymbol{C}_k$ and initial stiffness $\boldsymbol{C}_p$ components such that

$$\boldsymbol{C} = \boldsymbol{C}_k + \boldsymbol{C}_p = \begin{bmatrix} \frac{\partial \lambda_1}{\partial \boldsymbol{F}}, & \cdots, & \frac{\partial \lambda_d}{\partial \boldsymbol{F}} \end{bmatrix} [\boldsymbol{H}_W] \begin{bmatrix} \frac{\partial \lambda_1}{\partial \boldsymbol{F}} \\ \vdots \\ \frac{\partial \lambda_d}{\partial \boldsymbol{F}} \end{bmatrix} + \sum_{i=1}^{d} \Sigma_{\lambda_i} \frac{\partial^2 \lambda_i}{\partial \boldsymbol{F} \partial \boldsymbol{F}} = \underbrace{\sum_{i=1}^{d} \sum_{j=1}^{d} \frac{\partial^2 W}{\partial \lambda_i \lambda_j} \frac{\partial \lambda_i}{\partial \boldsymbol{F}} \otimes \frac{\partial \lambda_j}{\partial \boldsymbol{F}}}_{\boldsymbol{C}_k} + \underbrace{\sum_{i=1}^{d} \Sigma_{\lambda_i} \frac{\partial^2 \lambda_i}{\partial \boldsymbol{F} \partial \boldsymbol{F}}}_{\boldsymbol{C}_p}. \tag{31}$$

The initial stiffness operator $\boldsymbol{C}_p$ involves second directional derivatives of principal stretches but as mentioned earlier, it is not necessary to compute them through Eqns.18-19. This is due to the fact that, the eigensystem of the initial stiffness operator can be obtained in *closed-form*. To obtain it, we once again, refer to the stretch tensor invariants and their analytical eigensystem presented in [20]. Note that, for brevity, we have refrained from presenting the analytical eigensystem of elasticity operators in terms of stretch tensor invariants and refer the interested reader to Smith. B.[20]. Using the ingredients of[20] however, and reworking them through some lengthy but simple algebra by using Eqn. 20, it turns out that the analytical eigensystem of the initial stiffness operator is simpler than that of the stretch tensor invariants. Unlike the analytical eigensystem obtained through stretch tensor invariants in[20], the initial stiffness operator and the constitutive tangent operator are completely decoupled in principal stretch formulation. The initial stiffness has a null space of 2 in 2-dimensions and a null space of 3 in 3-dimensions. More specifically, in 2-dimensions the only two eigenvalues of the initial stiffness can be written concisely as

$$\bar{\lambda}_1^{\boldsymbol{C}_p} = \frac{\Sigma_{\lambda_1} - \Sigma_{\lambda_2}}{\lambda_1 - \lambda_2}, \qquad \bar{\lambda}_2^{\boldsymbol{C}_p} = \frac{\Sigma_{\lambda_1} + \Sigma_{\lambda_2}}{\lambda_1 + \lambda_2} \tag{32}$$

and similarly in 3-dimensions the 6 eigenvalues of the initial stiffness can be written concisely as

$$\bar{\lambda}_1^{\boldsymbol{C}_p} = \frac{\Sigma_{\lambda_2} - \Sigma_{\lambda_3}}{\lambda_2 - \lambda_3}, \qquad \bar{\lambda}_2^{\boldsymbol{C}_p} = \frac{\Sigma_{\lambda_1} - \Sigma_{\lambda_3}}{\lambda_1 - \lambda_3}, \qquad \bar{\lambda}_3^{\boldsymbol{C}_p} = \frac{\Sigma_{\lambda_1} - \Sigma_{\lambda_2}}{\lambda_1 - \lambda_2} \tag{33}$$

$$\bar{\lambda}_4^{\boldsymbol{C}_p} = \frac{\Sigma_{\lambda_2} + \Sigma_{\lambda_3}}{\lambda_2 + \lambda_3}, \qquad \bar{\lambda}_5^{\boldsymbol{C}_p} = \frac{\Sigma_{\lambda_1} + \Sigma_{\lambda_3}}{\lambda_1 + \lambda_3}, \qquad \bar{\lambda}_6^{\boldsymbol{C}_p} = \frac{\Sigma_{\lambda_1} + \Sigma_{\lambda_2}}{\lambda_1 + \lambda_2} \tag{34}$$

The fourth order initial stiffness operator is then obtained simply as an algebraic summation of the eigenvalues multiplied with their corresponding eigen-matrices as

$$\boldsymbol{C}_p = \sum_{i=1}^{k} \bar{\lambda}_i^{\boldsymbol{C}_p} [\boldsymbol{L}]_i \otimes [\boldsymbol{L}]_i + \sum_{i=1}^{k} \bar{\lambda}_{i+k}^{\boldsymbol{C}_p} [\boldsymbol{T}]_i \otimes [\boldsymbol{T}]_i, \quad \text{where} \quad k = 1 \text{ in 2D}; \; k = 3 \text{ in 3D} \tag{35}$$

where $[\boldsymbol{T}]_i$ are *twist* tensors already described in Eqn. 14 and $[\boldsymbol{L}]_i$ are *flip* tensors which have similar structure only with signs switched

$$[\boldsymbol{L}]_1 = \frac{1}{\sqrt{2}} \hat{\boldsymbol{U}} \begin{bmatrix} 0 & 1 \\ 1 & 0 \end{bmatrix} \hat{\boldsymbol{V}}^T, \quad \text{in 2D}, \tag{36a}$$

$$[\boldsymbol{L}]_1 = \frac{1}{\sqrt{2}} \hat{\boldsymbol{U}} \begin{bmatrix} 0 & 0 & 0 \\ 0 & 0 & 1 \\ 0 & 1 & 0 \end{bmatrix} \hat{\boldsymbol{V}}^T, \quad [\boldsymbol{L}]_2 = \frac{1}{\sqrt{2}} \hat{\boldsymbol{U}} \begin{bmatrix} 0 & 0 & 1 \\ 0 & 0 & 0 \\ 1 & 0 & 0 \end{bmatrix} \hat{\boldsymbol{V}}^T, \quad [\boldsymbol{L}]_3 = \frac{1}{\sqrt{2}} \hat{\boldsymbol{U}} \begin{bmatrix} 0 & 1 & 0 \\ 1 & 0 & 0 \\ 0 & 0 & 0 \end{bmatrix} \hat{\boldsymbol{V}}^T, \quad \text{in 3D}. \tag{36b}$$

As the names suggest, the twist and flip tensors contribute to geometrical behaviour of the system and are detached from deformation caused by the constitutive term.

2.5 | Partially rigid, truly rigid and stiff material models in principal stretches

Similar to the notion of incompressibility, materials that exhibit inextensibility in one or more principal directions are called partially rigid (truly rigid or just rigid if not deformable at all). Analogously, materials with very high shear modulus which are

close-to-rigid are called stiff. A classic mathematical example of such a model is the so-called *As-Rigid-As-Possible (ARAP)* model[34] commonly used in geometry processing applications[35]

$$W_{\text{ARAP}}(\lambda_i) = \frac{C_c}{2}\sum_{i=1}^{d}(\lambda_i - 1)^2 = \frac{C_c}{2}\sum_{i=1}^{d}(\lambda_i^2 - 2\lambda_i) + \frac{C_c d}{2}, \tag{37}$$

where C_c is a rigidity constant. It is evident that, this behaviour can be easily modelled using our proposed principal stretch formulation. On the other hand, it is forbiddingly complex to model this behaviour using principal stretch formulations based on the singular-values of Cauchy-Green strain tensor (i.e. squares of principal stretches) since the energy has terms that are linear in λ_is (as opposed to quadratic).

Notice that, similar to isochoric-volumetric splits in incompressibility, the polar decomposition of the deformation gradient itself serves as the multiplicative decomposition of $\boldsymbol{F}$ into a deformable (stretch) and non-deformable (rotation) component. Hence, as will be shown in Section 4 variational formulation for such models is straight-forward.

3 | GENERAL CONVEXITY CONDITIONS

3.1 | Convexity, rank-one convexity, and polyconvexity

The notion of polyconvexity was already hinted in the previous section when we made the assumption on $W(\mathcal{A})$ as a suitable energy functional. In particular, the assumption of $W(\mathcal{A})$ being a re-expression of a polyconvex energy $\hat{W}(\boldsymbol{F}, \boldsymbol{H}, J)$ implies that W is convex in $\boldsymbol{F}$, $\boldsymbol{H}$, and J, independently. However, and unfortunately, this notion does not extend to when W is expressed in terms of principal stretches in that, W is not *multi-variable convex* in individual principal stretches in the sense of Gil and Ortigosa[49]. In order to formalise a framework for convex large strain elasticity, we first recall some definitions:

Convexity: Convexity implies that for energy function $e(\boldsymbol{F})$ the following condition should be met[50,51,52]

$$e(\theta\boldsymbol{F}_1 + (1-\theta)\boldsymbol{F}_2) \leq \theta e(\boldsymbol{F}_1) + (1-\theta)e(\boldsymbol{F}_2); \quad \forall \boldsymbol{F}_1, \boldsymbol{F}_2; \quad \theta \in [0,1]. \tag{38}$$

which for differentiable functions can be expressed alternatively as

$$\left(\frac{\partial e(\boldsymbol{F}_1)}{\partial \boldsymbol{F}} - \frac{\partial e(\boldsymbol{F}_2)}{\partial \boldsymbol{F}}\right) : \left(\boldsymbol{F}_1 - \boldsymbol{F}_2\right) \geq 0; \qquad \forall \boldsymbol{F}_1, \boldsymbol{F}_2 \in \mathbb{R}^{d\times d} \tag{39}$$

and for twice differentiable functions can be expressed alternatively as

$$D^2 e(\boldsymbol{F})[\delta\boldsymbol{F}; \delta\boldsymbol{F}] = \delta\boldsymbol{F} \bullet \boldsymbol{C} \bullet \delta\boldsymbol{F} \geq 0; \quad \forall \boldsymbol{F}, \delta\boldsymbol{F}, \tag{40}$$

where $\bullet$ is the dual product. Eqn. 40 essentially mandates positive definiteness of the elasticity tensor $\boldsymbol{C}$ in Eqn. 27. For energies expressed in terms of the principlal stretches, convexity with respect to the latter (which is not to be confused with convexity with respect to $\boldsymbol{F}$) requires[53,54] the following condition on $W(\mathcal{A})$

$$W(\theta\mathcal{A}_1 + (1-\theta)\mathcal{A}_2) \leq \theta W(\mathcal{A}_1) + (1-\theta)W(\mathcal{A}_2); \quad \forall \mathcal{A}_1, \mathcal{A}_2; \quad \theta \in [0,1], \tag{41}$$

which once again for twice differentiable functions can be expressed alternatively as

$$D^2 W(\mathcal{A})[\delta\mathcal{A}; \delta\mathcal{A}] = \delta\mathcal{A} \bullet [\boldsymbol{H}_W] \bullet \delta\mathcal{A} \geq 0; \quad \forall \mathcal{A}, \delta\mathcal{A}. \tag{42}$$

Equation 42 mandates positive definiteness of the Hessian operator $[\boldsymbol{H}_W]$, which entails positive definiteness of the constitutive component $\boldsymbol{C}_k$ in 31. Similarly to equation 39, an equivalent condition to 42 can be established as

$$\left(\boldsymbol{\nabla} W(\mathcal{A}_1) - \boldsymbol{\nabla} W(\mathcal{A}_2)\right) \cdot \left(\mathcal{A}_1 - \mathcal{A}_2\right) \geq 0; \qquad \boldsymbol{\nabla} W = \left[\begin{array}{ccc} \frac{\partial W}{\partial \lambda_1} & \cdots & \frac{\partial W}{\partial \lambda_n} \end{array}\right]^T, \qquad \mathcal{A}_p = \left[\begin{array}{ccc} (\lambda_p)_1 & \ldots & (\lambda_p)_n \end{array}\right]^T \tag{43}$$

As already stated, convexity with respect to principal stretches and with respect to $\boldsymbol{F}$ is not equivalent. This can clearly be observed by replacing $\delta\mathcal{A}$ with $D\mathcal{A}[\delta\boldsymbol{F}]$ in 42, yielding

$$D^2W(\mathcal{A})[\delta\mathcal{A}[\delta\boldsymbol{F}];\delta\mathcal{A}[\delta\boldsymbol{F}]] = \delta\boldsymbol{F}\bullet\Bigg[\underbrace{\begin{bmatrix}\frac{\partial\lambda_1}{\partial\boldsymbol{F}},&\cdots,&\frac{\partial\lambda_d}{\partial\boldsymbol{F}}\end{bmatrix}[\boldsymbol{H}_W]\begin{bmatrix}\frac{\partial\lambda_1}{\partial\boldsymbol{F}}\\ \vdots\\ \frac{\partial\lambda_d}{\partial\boldsymbol{F}}\end{bmatrix}}_{\boldsymbol{C}_k}+\underbrace{\sum_{i=1}^{d}\Sigma_{\lambda_i}\frac{\partial^2\lambda_i}{\partial\boldsymbol{F}\partial\boldsymbol{F}}}_{\boldsymbol{C}_p}\Bigg]\bullet\delta\boldsymbol{F}\geq 0;\quad\forall\boldsymbol{F},\delta\boldsymbol{F}. \tag{44}$$

Clearly, Eqn. 44 mandates positive definiteness of the elasticity tensor $\boldsymbol{C}$ in Eqn. 31, and hence, of both constitutive and initial contributions $\boldsymbol{C}_k$ and $\boldsymbol{C}_p$. In general, this is a stringent condition to meet since in most cases it prohibits realistic behaviour of material away from the origin.

For energies which are convex with respect to the principal stretches, the constitutive component $\boldsymbol{C}_k$ is always semi-positive definite[4] (implied by Eqn. 42). Despite the non-realistic physical behaviour of convex energies with respect to $\boldsymbol{F}$, in the following, we will derive the conditions that $W(\mathcal{A})$ need to satisfy, by carefully analysing the initial stiffness contribution $\boldsymbol{C}_p$, for $W(\mathcal{A})$ to be convex with respect to $\boldsymbol{F}$. Essentially, this entails the following condition to be satisfied

$$\delta\boldsymbol{F}:\boldsymbol{C}_p:\delta\boldsymbol{F}=\delta\boldsymbol{F}:\left[\sum_{i=1}^{d}\Sigma_{\lambda_i}\frac{\partial^2\lambda_i}{\partial\boldsymbol{F}\partial\boldsymbol{F}}\right]:\delta\boldsymbol{F}\geq 0. \tag{45}$$

Substituting for Eqn. 35 in the above equation leads to

$$\begin{aligned}\delta\boldsymbol{F}:\boldsymbol{C}_p:\delta\boldsymbol{F}&=\delta\boldsymbol{F}:\left[\sum_{i=1}^{k}\bar{\lambda}_i^{\boldsymbol{C}_p}[\boldsymbol{L}]_i\otimes[\boldsymbol{L}]_i+\sum_{i=1}^{k}\bar{\lambda}_{i+k}^{\boldsymbol{C}_p}[\boldsymbol{T}]_i\otimes[\boldsymbol{T}]_i\right]:\delta\boldsymbol{F}\\&=\sum_{i=1}^{k}\bar{\lambda}_i^{\boldsymbol{C}_p}\left(\delta\boldsymbol{F}:[\boldsymbol{L}]_i\right)^2+\sum_{i=1}^{k}\bar{\lambda}_{i+k}^{\boldsymbol{C}_p}\left(\delta\boldsymbol{F}:[\boldsymbol{T}]_i\right)^2\end{aligned} \tag{46}$$

From the above relations we observe that above inequality holds (i.e. semi-positive definiteness of initial stiffness is guaranteed) if $\bar{\lambda}_i^{\boldsymbol{C}_p}\geq 0$. This is evident since, $\bar{\lambda}_i^{\boldsymbol{C}_p}$ are the eigenvalues of the initial stiffness operator. This result permits to establish the conditions that guarantee convexity with respect to $\boldsymbol{F}$ for energies written in terms of the principal stretches, i.e. $W(\mathcal{A})$.

Corollary 1: A sufficiently smooth and twice differentiable two-dimensional energy function $e(\boldsymbol{F})$ is convex in $\boldsymbol{F}$ if and only if there exists a function $W(\lambda_1,\lambda_2)=e(\boldsymbol{F})$ that satisfies

$$\boxed{\frac{\Sigma_{\lambda_1}+\Sigma_{\lambda_2}}{\lambda_1+\lambda_2}\geq 0,\qquad\frac{\Sigma_{\lambda_1}-\Sigma_{\lambda_2}}{\lambda_1-\lambda_2}\geq 0,\qquad\frac{\partial^2W}{\partial\lambda_1\partial\lambda_1}\frac{\partial^2W}{\partial\lambda_2\partial\lambda_2}\geq\left(\frac{\partial^2W}{\partial\lambda_1\partial\lambda_2}\right)^2.} \tag{47}$$

Corollary 2: A sufficiently smooth and twice differentiable three-dimensional energy function $e(\boldsymbol{F})$ is convex in $\boldsymbol{F}$ if and only if there exists a function $W(\lambda_1,\lambda_2,\lambda_3)=e(\boldsymbol{F})$ that satisfies

$$\boxed{\begin{aligned}&\frac{\Sigma_{\lambda_1}+\Sigma_{\lambda_2}}{\lambda_1+\lambda_2}\geq 0,\quad\frac{\Sigma_{\lambda_1}+\Sigma_{\lambda_3}}{\lambda_1+\lambda_3}\geq 0,\quad\frac{\Sigma_{\lambda_2}+\Sigma_{\lambda_3}}{\lambda_2+\lambda_3}\geq 0,\\&\frac{\Sigma_{\lambda_1}-\Sigma_{\lambda_2}}{\lambda_1-\lambda_2}\geq 0,\quad\frac{\Sigma_{\lambda_1}-\Sigma_{\lambda_3}}{\lambda_1-\lambda_3}\geq 0,\quad\frac{\Sigma_{\lambda_2}-\Sigma_{\lambda_3}}{\lambda_2-\lambda_3}\geq 0,\\&\frac{\partial^2W}{\partial\lambda_1\partial\lambda_1}\frac{\partial^2W}{\partial\lambda_2\partial\lambda_2}\frac{\partial^2W}{\partial\lambda_3\partial\lambda_3}+2\frac{\partial^2W}{\partial\lambda_1\partial\lambda_2}\frac{\partial^2W}{\partial\lambda_1\partial\lambda_3}\frac{\partial^2W}{\partial\lambda_2\partial\lambda_3}\geq\\&\frac{\partial^2W}{\partial\lambda_1\partial\lambda_1}\left(\frac{\partial^2W}{\partial\lambda_2\partial\lambda_3}\right)^2+\frac{\partial^2W}{\partial\lambda_2\partial\lambda_2}\left(\frac{\partial^2W}{\partial\lambda_1\partial\lambda_3}\right)^2+\frac{\partial^2W}{\partial\lambda_3\partial\lambda_3}\left(\frac{\partial^2W}{\partial\lambda_1\partial\lambda_2}\right)^2.\end{aligned}} \tag{48}$$

The proof of above convexity condition is presented in Appendix A.

Rank-one convexity, ellipticity condition and Legendre-Hardamard condition: A weaker requirement than convexity is that

of *rank-one convexity* of $e(\boldsymbol{F})$, which implies that for energy function $e(\boldsymbol{F})$, the following condition should be met[50,51,53]

$$e(\boldsymbol{F}+\theta\boldsymbol{u}\otimes\boldsymbol{V}) \leq \theta e(\boldsymbol{F}+\boldsymbol{u}\otimes\boldsymbol{V}) + (1-\theta)e(\boldsymbol{F}); \quad \forall \boldsymbol{F}\in\mathbb{R}^{d\times d}, \boldsymbol{u},\boldsymbol{V}\in\mathbb{R}^{d}; \quad \theta\in[0,1], \tag{49}$$

Notice that (49) is simply a particularisation of (38) using $\boldsymbol{F}_1 = \boldsymbol{F}+\boldsymbol{u}\otimes\boldsymbol{V}$ and $\boldsymbol{F}_2 = \boldsymbol{F}$. For twice differentiable functions this condition can be expressed alternatively as

$$D^2 e(\boldsymbol{F})[\boldsymbol{u}\otimes\boldsymbol{V};\boldsymbol{u}\otimes\boldsymbol{V}] = (\boldsymbol{u}\otimes\boldsymbol{V})\bullet\boldsymbol{C}\bullet(\boldsymbol{u}\otimes\boldsymbol{V}) \geq 0; \quad \forall \boldsymbol{u},\boldsymbol{V}\in\mathbb{R}^{d}. \tag{50}$$

Similarly, following[53,54], the rank-one convexity condition in Eqn. 50 can also be written for energies expressed in terms of principal stretches such as $W(\mathcal{A})$ which for twice functions leads to

$$\begin{aligned} D^2 W(\mathcal{A})[D\mathcal{A}[\boldsymbol{u}\otimes\boldsymbol{V}];D\mathcal{A}[\boldsymbol{u}\otimes\boldsymbol{V}]] = (\boldsymbol{u}\otimes\boldsymbol{V})\bullet\left[\left[\frac{\partial\lambda_1}{\partial\boldsymbol{F}},\ \cdots,\ \frac{\partial\lambda_d}{\partial\boldsymbol{F}}\right][\boldsymbol{H}_W]\begin{bmatrix}\frac{\partial\lambda_1}{\partial\boldsymbol{F}}\\ \vdots\\ \frac{\partial\lambda_d}{\partial\boldsymbol{F}}\end{bmatrix}\right]\bullet(\boldsymbol{u}\otimes\boldsymbol{V}) \\ + (\boldsymbol{u}\otimes\boldsymbol{V})\bullet\left[\sum_{i=1}^{d}\Sigma_{\lambda_i}\frac{\partial^2\lambda_i}{\partial\boldsymbol{F}\partial\boldsymbol{F}}\right]\bullet(\boldsymbol{u}\otimes\boldsymbol{V}) \geq 0; \quad \forall \boldsymbol{u},\boldsymbol{V}\in\mathbb{R}^{d}. \end{aligned} \tag{51}$$

The condition in Eqn. 51 is analogously referred to as the *Legendre-Hadamard* condition or *ellipticity* of W, linked to the propagation of travelling plane wave within the material defined by a vector $\boldsymbol{V}$ at speed c. Clearly, convexity of W with respect to principal stretches automatically yields positiveness of the constitutive term (i.e. first term on the right-hand side of 51). However, convexity in principal stretches is not a sufficient condition guaranteeing the rank-one condition, as it can be seen by inspecting the initial term (i.e. second term on the right-hand side of 51), i.e.

$$(\boldsymbol{u}\otimes\boldsymbol{V})\bullet\left[\sum_{i=1}^{d}\Sigma_{\lambda_i}\frac{\partial^2\lambda_i}{\partial\boldsymbol{F}\partial\boldsymbol{F}}\right]\bullet(\boldsymbol{u}\otimes\boldsymbol{V}) = \sum_{i=1}^{k}\bar{\lambda}_i^{\mathcal{C}_p}\left(\boldsymbol{u}\cdot[\boldsymbol{L}]_i\boldsymbol{V}\right)^2 + \sum_{i=1}^{k}\bar{\lambda}_{i+k}^{\mathcal{C}_p}\left(\boldsymbol{u}\cdot[\boldsymbol{T}]_i\boldsymbol{V}\right)^2, \tag{52}$$

whose positiveness is subject to positiveness of the eigenvalues of the initial component of the constitutive model, which are essentially the same conditions required for the satisfaction of convexity.

Polyconvexity: It is well-known that, ***polyconvexity*** is a sufficient condition guaranteeing the ellipticity condition in 50[1,50]. Polyconvexity requires $e(\boldsymbol{\nabla}_0\boldsymbol{x})$ to be expressed as

$$e(\boldsymbol{\nabla}_0\boldsymbol{x}) = \hat{W}(\boldsymbol{\mathcal{V}}); \qquad \boldsymbol{\mathcal{V}} = \{\boldsymbol{F},\boldsymbol{H},J\},\ (d=3) \tag{53}$$

where $\hat{W}(\boldsymbol{\mathcal{V}})$ must be convex with respect to its arguments, namely

$$\hat{W}(\theta\boldsymbol{\mathcal{V}}_1 + (1-\theta)\boldsymbol{\mathcal{V}}_2) \leq \theta\hat{W}(\boldsymbol{\mathcal{V}}_1) + (1-\theta)\hat{W}(\boldsymbol{\mathcal{V}}_2); \quad \forall\boldsymbol{\mathcal{V}}_1,\boldsymbol{\mathcal{V}}_2,\ \theta\in[0,1], \tag{54}$$

which for twice differentiable functions can be expressed alternatively as

$$D^2\hat{W}(\boldsymbol{\mathcal{V}})[\delta\boldsymbol{\mathcal{V}};\delta\boldsymbol{\mathcal{V}}] = \delta\boldsymbol{\mathcal{V}}\bullet[\boldsymbol{H}_{\hat{W}}]\bullet\delta\boldsymbol{\mathcal{V}} \geq 0; \quad \forall\delta\boldsymbol{\mathcal{V}}; \qquad \boldsymbol{H}_{\hat{W}} = \begin{bmatrix}\frac{\partial^2\hat{W}}{\partial\boldsymbol{F}\partial\boldsymbol{F}} & \frac{\partial^2\hat{W}}{\partial\boldsymbol{F}\partial\boldsymbol{H}} & \frac{\partial^2\hat{W}}{\partial\boldsymbol{F}\partial J}\\ & \frac{\partial^2\hat{W}}{\partial\boldsymbol{H}\partial\boldsymbol{H}} & \frac{\partial^2\hat{W}}{\partial\boldsymbol{H}\partial J}\\ sym & & \frac{\partial^2\hat{W}}{\partial J^2}\end{bmatrix}. \tag{55}$$

Eqn. 55 essentially mandates positive definiteness of the Hessian operator $\boldsymbol{H}_{\hat{W}}$. It is well-known that polyconvexity does not entail convexity with respect to $\boldsymbol{F}$. This can clearly be observed when particularising $\delta\mathcal{V}$ with $D\mathcal{V}[\delta\boldsymbol{F}]$ in 55, yielding [2].

$$D^2\hat{W}(\mathcal{V})[\delta\mathcal{V}[\delta\boldsymbol{F}];\delta\mathcal{V}[\delta\boldsymbol{F}]] = \delta\boldsymbol{F}\bullet\Bigg[\underbrace{\left[\mathbb{I},\ \mathbb{I}\times\boldsymbol{F},\ \boldsymbol{H}\right][\boldsymbol{H}_{\hat{W}}]\begin{bmatrix}\mathbb{I}\\ \mathbb{I}\times\boldsymbol{F}\\ \boldsymbol{H}\end{bmatrix}}_{\hat{\mathcal{C}}_k} + \underbrace{\mathbb{I}\times\left(\frac{\partial\hat{W}}{\partial\boldsymbol{H}}+\frac{\partial\hat{W}}{\partial J}\boldsymbol{F}\right)}_{\hat{\mathcal{C}}_p}\Bigg]\bullet\delta\boldsymbol{F} \geq 0; \quad \forall\delta\boldsymbol{F}. \tag{56}$$

[2] Refer to [55] for a derivation of the tangent operator shown in equation 56.

It is possible to see the similarity between the principal stretch representation $W(\mathcal{A})$ and the polyconvex representaton $\hat{W}(\mathcal{V})$. This is reflected in the additive split of the tangent operator of both representations between constitutive and initial components, namely $\{\boldsymbol{C}_k, \boldsymbol{C}_p\}$ in 44 and $\{\hat{\boldsymbol{C}}_k, \hat{\boldsymbol{C}}_p\}$ in 56. Clearly, the constitutive contributions in both representations, namely $\boldsymbol{C}_k$ and $\hat{\boldsymbol{C}}_k$ would yield a positive contribution provided that $W(\mathcal{A})$ is convex with respect to $\mathcal{A}$ and $\hat{W}(\mathcal{V})$ is convex with respect to $\mathcal{V}$. However, polyconvexity of $\hat{W}(\mathcal{V})$ entails a crucial difference from the rank-one convexity standpoint. This can be seen when replacing $\delta\boldsymbol{F}$ with rank-one tensors $\boldsymbol{u}\otimes\boldsymbol{V}$ in 56. As shown by[56], this specification yields a vanishing contribution from $\hat{\boldsymbol{C}}_p$, which permits to particularise 56 to rank-one tensors as

$$D^2\hat{W}(\mathcal{V})[\boldsymbol{u}\otimes\boldsymbol{V};\boldsymbol{u}\otimes\boldsymbol{V}] = \boldsymbol{u}\otimes\boldsymbol{V}\bullet\hat{\boldsymbol{C}}_k\bullet\boldsymbol{u}\otimes\boldsymbol{V}\geq 0;\quad \forall\boldsymbol{u},\boldsymbol{V}. \tag{57}$$

Above equation 57 is consequence that polyconvexity is a sufficient condition that fulfils the ellipticity condition, since the constitutive component is always semi-positive definite[4]. However, for the principal stretch representation $W(\mathcal{A})$, the initial stiffness operator in 51 (second term on the right-hand side) does not necessarily vanish (unlike in polyconvex formulations) which implies the ellipticity condition cannot be met based on the semi-positive definiteness of the Hessian operator $\boldsymbol{H}_W$ alone. While certainly ellipticity condition cannot be determined based on the Hessian alone in the principal stretch setting, the separation of constitutive and initial stiffness operators in 44 are still advantageous since it lets us study their eigen structure individually. It is straight-forward to determine that the Hessian operator $\boldsymbol{H}_W$ is not always semi-positive definite through a counter-example.

Example 1: Consider the plane strain volumetric function $f(J)=\frac{\kappa}{2}(J-1)^2$ convex $\forall J\geq 0$ such that $f:\mathbb{R}\to\mathbb{R}$ and $\kappa>0$. For simplicity, consider a purely scaling deformation $\boldsymbol{F}=[\gamma_1,0;0,\gamma_2]$. The re-expressed function in terms of principal stretches i.e. $\tilde{W}=\frac{\kappa}{2}(\lambda_1\lambda_2-1)^2$ is not semi-positive definite for all ranges of deformation (i.e. $\forall\gamma_1,\gamma_2$) as we have

$$\boldsymbol{H}_{\tilde{W}}=\begin{bmatrix}\dfrac{\partial^2\tilde{W}}{\partial\lambda_1\partial\lambda_1} & \dfrac{\partial^2\tilde{W}}{\partial\lambda_1\partial\lambda_2}\\ \dfrac{\partial^2\tilde{W}}{\partial\lambda_2\partial\lambda_1} & \dfrac{\partial^2\tilde{W}}{\partial\lambda_2\partial\lambda_2}\end{bmatrix}=\kappa\begin{bmatrix}\gamma_2^2 & 2\gamma_1\gamma_2-1\\ 2\gamma_1\gamma_2-1 & \gamma_1^2\end{bmatrix}, \tag{58}$$

whose semi-positive definiteness leads to the inequality $(\gamma_1\gamma_2)^2\geq(2\gamma_1\gamma_2-1)^2$ which clearly does not hold for $\gamma_1\gamma_2=J<\frac{1}{3}$.

3.2 | Stabilisation of the Hessian $\boldsymbol{H}_W$

One advantage of the principal stretch formulation is that the resulting Hessian operator $\boldsymbol{H}_W$ is only a second order tensor of dimensions $d\times d$ and simple to manipulate. In fact, it is possible to find the exact points of Hessian indefiniteness by performing *closed-form* eigenvalue analysis. In the following, we describe multiple possible approaches that such energies can be stabilised.

1. Stabilisation through Laplacian stabilisation: One popular technique to stabilise the Hessian operator is through Laplacian stabilisation. This can be achieved in many ways. For instance, by adding a fraction of the Laplacian matrix to the Hessian or even to the resulting tangent elasticity tensor or even to the per-element resulting finite element stiffness matrix[8]. A more consistent technique in our setting would be to add or increase the contribution of the term $I_2=\boldsymbol{F}:\boldsymbol{F}$ in the energy as the Hessian of I_2 is the Laplacian. Consider the function $W_{Lapl}(\mathcal{A})$ in 2-dimensions

$$W_{Lapl}(\mathcal{A})=\frac{\tau}{2}I_2=\frac{\tau}{2}(\lambda_1^2+\lambda_2^2);\qquad \boldsymbol{H}_{W_{Lapl}}=\begin{bmatrix}\dfrac{\partial^2 W_{Lapl}}{\partial\lambda_1\partial\lambda_1} & \dfrac{\partial^2 W_{Lapl}}{\partial\lambda_1\partial\lambda_2}\\ \dfrac{\partial^2 W_{Lapl}}{\partial\lambda_2\partial\lambda_1} & \dfrac{\partial^2 W_{Lapl}}{\partial\lambda_2\partial\lambda_2}\end{bmatrix}=\tau\begin{bmatrix}1&0\\0&1\end{bmatrix}=\tau\boldsymbol{I},$$

whose Hessian is a constant scaling matrix and where τ serves as the stabilisation parameter. The downside of Laplacian stabilisation however is that, it is a rule-of-thumb procedure as the exact amount of stabilisation to add to the system is not known in advance.

2. Stabilisation through spectral shifting: A method recently advocated by Poya et. al.[44] spectrally shifts the singular-values of $\boldsymbol{F}$ from λ_i to $\lambda_i+\beta$ to obtain a regularised deformation gradient $\boldsymbol{F}_r=\hat{\boldsymbol{U}}\boldsymbol{\Lambda}_r\hat{\boldsymbol{V}}^T$ (s.t. $\Lambda_{r_{ii}}=\lambda_i+\beta$) through a carefully chosen

constant β. Consequently, performing linearisation around the regularised deformation gradient $\boldsymbol{F}_r$ results in energies that are convex in a selected range. For instance, using such arrangement the volumetric term considered earlier in Example 1 leads to inequality $(\gamma_1+\beta)^2(\gamma_2+\beta)^2 \geq \big(2(\gamma_1+\beta)(\gamma_2+\beta)-1\big)^2$ which can be convexified for $J \in [0, \frac{1}{3}]$ by choosing $\beta = -\frac{1}{3}$. The benefit of this approach is that it retains the quadratic convergence of Newton-Raphson. However, such spectral shifts cannot be applied globally as they adversely affect other deformation ranges wherein the energy may have been already convex. Poya et. al.[44] advocates locally applying the shift and considering different βs for different ranges of deformation.

3. Stabilisation through projection to semi-positive definite cone: A more prudent way to guarantee semi-positive definiteness of $\boldsymbol{H}_W$ is by performing an L^2 projection to semi-positive definite cone. This has traditionally been achieved numerically by performing eigen-decomposition on the much larger tangent elasticity tensor $\boldsymbol{C}_k$ and clamping the negative eigenvalues to zeros[14,15]. This technique has been applied successfully for many optimisation problems and it leads to a second order method usually referred to as the Projected Newton or PN in short.

$$\boldsymbol{H}_W^{\text{SPD}} = \sum_{i=1}^{d} \max(\bar{\lambda}_i^{\boldsymbol{H}_W}, 0)\ \boldsymbol{e}_i \otimes \boldsymbol{e}_i, \tag{59}$$

where $\bar{\lambda}_i^{\boldsymbol{H}_W}$ are the eigenvalues and $\boldsymbol{e}_i$ are the eigenvectors of the Hessian $\boldsymbol{H}_W$. Fortunately, the eigenvalues of the constitutive part of the elasticity tensor $\boldsymbol{C}_k$ can be found in closed-form through analytic eigen-decomposition of $\boldsymbol{H}_W$ since $\boldsymbol{C}_k$ has a null space of 2 in 2-dimensions and 6 in 3-dimensions. In particular, the eigen-decomposition of $\boldsymbol{H}_W$ is simple to find in 2-dimensions:

$$\bar{\lambda}_1^{\boldsymbol{H}_W} = \frac{1}{2}\left(\partial^2_{\lambda_1\lambda_1} W + \partial^2_{\lambda_2\lambda_2} W - \sqrt{\left(\partial^2_{\lambda_1\lambda_1} W - \partial^2_{\lambda_2\lambda_2} W\right)^2 + 4\partial^2_{\lambda_1\lambda_2} W}\right) \tag{60a}$$

$$\bar{\lambda}_2^{\boldsymbol{H}_W} = \frac{1}{2}\left(\partial^2_{\lambda_1\lambda_1} W + \partial^2_{\lambda_2\lambda_2} W + \sqrt{\left(\partial^2_{\lambda_1\lambda_1} W - \partial^2_{\lambda_2\lambda_2} W\right)^2 + 4\partial^2_{\lambda_1\lambda_2} W}\right) \tag{60b}$$

with the eigenvectors $\boldsymbol{e}_i$ emerging as

$$\boldsymbol{e}_1 = [\frac{\bar{\lambda}_1^{\boldsymbol{H}_W} - \partial^2_{\lambda_2\lambda_2} W}{\partial^2_{\lambda_1\lambda_2} W}, 1]^T_n, \qquad \boldsymbol{e}_2 = [\frac{\bar{\lambda}_2^{\boldsymbol{H}_W} - \partial^2_{\lambda_2\lambda_2} W}{\partial^2_{\lambda_1\lambda_2} W}, 1]^T_n \tag{61}$$

where we have used the notation $\partial^2_{\partial\lambda_i\partial\lambda_j} W = \frac{\partial^2 W}{\partial\lambda_i\partial\lambda_j}$ and the subscript n indicates normalisation of the eigenvectors. Similar albeit more lengthy formula exist for closed-form eigen-decompositions in 3-dimensions (i.e. for 3×3 symmetric matrices) as shown in the Appendix in Eqns. B13-B16; c.f. Golub and Van Loan[57] and Deledalle et. al.[58]. For certain isotropic models $\boldsymbol{H}_W$ is already diagonal and the above decomposition is not needed. Finally, once $\boldsymbol{H}_W^{\text{SPD}}$ has been obtained the semi-positive definite constitutive tangent elasticity tensor $\boldsymbol{C}_k^{\text{SPD}}$ can be built in d-dimensions simply as

$$\boldsymbol{C}_k^{\text{SPD}} = \left[\frac{\partial\lambda_1}{\partial\boldsymbol{F}}, \cdots, \frac{\partial\lambda_d}{\partial\boldsymbol{F}}\right] [\boldsymbol{H}_W^{\text{SPD}}] \begin{bmatrix} \frac{\partial\lambda_1}{\partial\boldsymbol{F}} \\ \vdots \\ \frac{\partial\lambda_d}{\partial\boldsymbol{F}} \end{bmatrix} \tag{62}$$

Given the scaling nature of $\dfrac{\partial\lambda_i}{\partial\boldsymbol{F}}$ presented in Eqns. 16 - 17 such reconstruction is trivially obtained.

3.3 | Stabilisation of initial stiffness operator (total stabilisation)

The hallmark of the proposed formulation is the fact that, eigenvalues of both the initial stiffness and Hessian operators are found analytically. Hence, a similar semi-positive definite projection can be performed on the initial stiffness term. This is an easier case as the eigensystem of initial stiffness operator is already obtained in a decomposed form as presented in Eqn. 35. Consequently, semi-positive definite projection is obtained via

$$\boldsymbol{C}_p^{\text{SPD}} = \sum_{i=1}^{k} \max(\bar{\lambda}_i^{\boldsymbol{C}_p}, 0)[\boldsymbol{L}]_i \otimes [\boldsymbol{L}]_i + \sum_{i=1}^{k} \max(\bar{\lambda}_{i+k}^{\boldsymbol{C}_p}, 0)[\boldsymbol{T}]_i \otimes [\boldsymbol{T}]_i. \tag{63}$$

Finally the semi-positive definite total tangent elasticity operator is constructed as

$$\boldsymbol{C}^{\text{SPD}} = \boldsymbol{C_k}^{\text{SPD}} + \boldsymbol{C_p}^{\text{SPD}} = \left[\frac{\partial \lambda_1}{\partial \boldsymbol{F}}, \cdots, \frac{\partial \lambda_d}{\partial \boldsymbol{F}}\right] [\boldsymbol{H}_W^{\text{SPD}}] \begin{bmatrix} \frac{\partial \lambda_1}{\partial \boldsymbol{F}} \\ \vdots \\ \frac{\partial \lambda_d}{\partial \boldsymbol{F}} \end{bmatrix} + \sum_{i=1}^{k} \max(\bar{\lambda}_i^{\boldsymbol{C}_p}, 0)[\boldsymbol{L}]_i \otimes [\boldsymbol{L}]_i + \sum_{i=1}^{k} \max(\bar{\lambda}_{i+k}^{\boldsymbol{C}_p}, 0)[\boldsymbol{T}]_i \otimes [\boldsymbol{T}]_i, \tag{64}$$

which leads to a complete stabilisation of the system. Unlike the standard nonlinear finite element procedures where loading is applied in increments, the above stabilisation strategy enables solving nonlinear problems in a single loading increment. However, using single increment can result in an overtly smooth profile and applying increments is still advised. The observation is that projecting the elasticity operators amounts to approximating the tangent direction as compared to using the actual one and the resulting nonlinear minimisation algorithm falls under the umbrella of Quasi-Newton techniques. Hence, buckling and other geometrical instabilities can then be simulated by using a small number of increments as shown in Fig. 4. Similar nonlinear algorithms that use different flavours of approximated tangents with the use of increments have appeared in the literature for instance the consistently linearised elasticity [17] and electro-elasticity [21]. Finally, for clarity, the complete procedure for obtaining the closed-form eigensystem of elasticity operators using principal stretch ingredients is consolidated in Fig. 3.

Growth condition and coercivity: Another restrictions imposed on hyperelastic energies is that of growth condition which dictates that the assumed strain energy should satisfy

$$e(\boldsymbol{F}) \begin{cases} \geq \boldsymbol{C}\left(||\boldsymbol{F}||^p + \boldsymbol{J}^r\right) & \text{if } \boldsymbol{J} > 0, \\ = +\infty, & \text{otherwise} \end{cases} \tag{65}$$

for $p > 2$, $r > 1$ and some constant $C > 0$. Casting this in terms of principal stretches results in

$$W(\mathcal{A}) \begin{cases} \geq \boldsymbol{C}\left(\sum_{i=d}^{d} ||\lambda_i||^p + \left(\prod_{i=1}^{d} \lambda_i\right)^r\right) & \text{if } \left(\prod_{i=1}^{d} \lambda_i\right) > 0, \\ = +\infty, & \text{otherwise} \end{cases} \tag{66}$$

It is important to note that, a suitable growth condition *and* polyconvexity of W guarantees the existence of minimisers [1]. Coercivity is a growth condition imposed on strain energies. Let $\Pi(\boldsymbol{x}) = \int_V e(\boldsymbol{F})\, \mathrm{d}V$ be the elastic potential energy functional. Then, Π is said to be q-coercive (for $q \geq 1$) whenever for all $K > 0$ there is some $\tilde{K} > 0$ such that

$$||\Pi(\boldsymbol{x})|| \leq K \;\Rightarrow\; ||e(\boldsymbol{F})||_{L^q} \leq \tilde{K}, \tag{67}$$

where $||\bullet||_{L^q}$ denotes the q Sobolov norm. Coercivity has an important role in large strain elasticity as it dictates that the energy increase should be bounded from above. Conformal energies that are used as isochoric part of incompressible elasticity are well-known to be coercive [50,53,54]. Coercivity is even more important in the context of tangent stabilised large strain elasticity since it is closely related to the notion of "flip-prevention" (energies that tend to infinity as $J \to 0$ are often called flip-preventing). In fact, coercivity is an indispensable part of tangent stabilised large strain elasticity as otherwise the stabilised nature of the problem allows for simulations to proceed even when inter-penetration occurs which invalidates the fundamental assumption of continuity of matter. The past decade has seen many applications of flip-preventing nonlinear material design using stabilised tangents in geometry processing and computer graphics applications [14,15,13,18,59,20].

Example 2: Inspired by the preceding discussion, for the rest of this work, we consider two material models and work out their Hessian and initial stiffness eigensystems. The 2-dimensional case is worked out and written here as they are shorter. The 3-dimensional eigensystems can be similarly found symbolically using the script provided in the appendix. The first model considered is the compressible Mooney-Rivlin energy defined as

$$W_{MR} = \mu_1 I_2 + \mu_2 I_4 - 2(\mu_1 + 2\mu_2)\ln(I_5) + \frac{\kappa}{2}(I_5 - 1)^2, \tag{68}$$

Eigensystem of tangent elasticity tensor (2D)

Given the Singular-Value-Decomposition (SVD) of $\boldsymbol{F}$

$$\boldsymbol{F} = \hat{\boldsymbol{U}}\boldsymbol{\Lambda}\hat{\boldsymbol{V}}^T, \quad \text{with} \quad \lambda_i = \Lambda_{ii} \quad i = 1,2$$

The first derivatives of principal stretches are

$$\frac{\partial \lambda_1}{\partial \boldsymbol{F}} = \hat{\boldsymbol{U}}\begin{bmatrix}1 & 0\\ 0 & 0\end{bmatrix}\hat{\boldsymbol{V}}^T, \qquad \frac{\partial \lambda_2}{\partial \boldsymbol{F}} = \hat{\boldsymbol{U}}\begin{bmatrix}0 & 0\\ 0 & 1\end{bmatrix}\hat{\boldsymbol{V}}^T$$

For a given isotropic energy $W(\lambda_1, \lambda_2)$ expressed in terms of principal stretches, the Hessian operator is

$$\boldsymbol{H}_W = \begin{bmatrix}\partial^2_{\lambda_1\lambda_1} W & \partial^2_{\lambda_1\lambda_2} W\\ sym & \partial^2_{\lambda_2\lambda_2} W\end{bmatrix}$$

If $\partial^2_{\lambda_1\lambda_2} W = 0$, then the eigen-decomposition of the Hessian is simply

$$\bar{\lambda}_1^{\boldsymbol{H}_W} = \partial^2_{\lambda_1\lambda_1} W, \qquad \boldsymbol{e}_1 = [1,0]^T$$
$$\bar{\lambda}_2^{\boldsymbol{H}_W} = \partial^2_{\lambda_2\lambda_2} W, \qquad \boldsymbol{e}_2 = [0,1]^T$$

otherwise the eigen-decomposition of $\boldsymbol{H}_W$ is obtained in closed-form as

$$\bar{\lambda}_1^{\boldsymbol{H}_W} = \frac{1}{2}\left(\partial^2_{\lambda_1\lambda_1} W + \partial^2_{\lambda_2\lambda_2} W - \sqrt{\left(\partial^2_{\lambda_1\lambda_1} W - \partial^2_{\lambda_2\lambda_2} W\right)^2 + 4\partial^2_{\lambda_1\lambda_2} W}\right)$$
$$\bar{\lambda}_2^{\boldsymbol{H}_W} = \frac{1}{2}\left(\partial^2_{\lambda_1\lambda_1} W + \partial^2_{\lambda_2\lambda_2} W + \sqrt{\left(\partial^2_{\lambda_1\lambda_1} W - \partial^2_{\lambda_2\lambda_2} W\right)^2 + 4\partial^2_{\lambda_1\lambda_2} W}\right)$$
$$\boldsymbol{e}_1 = [\frac{\bar{\lambda}_1^{\boldsymbol{H}_W} - \partial^2_{\lambda_2\lambda_2} W}{\partial^2_{\lambda_1\lambda_2} W}, 1]^T_n, \qquad \boldsymbol{e}_2 = [\frac{\bar{\lambda}_2^{\boldsymbol{H}_W} - \partial^2_{\lambda_2\lambda_2} W}{\partial^2_{\lambda_1\lambda_2} W}, 1]^T_n$$

The semi-positive definite Hessian operator is then constructed as

$$\boldsymbol{H}_W^{\text{SPD}} = \sum_{i=1}^{2} \max(\bar{\lambda}_i^{\boldsymbol{H}_W}, 0)\ \boldsymbol{e}_i \otimes \boldsymbol{e}_i$$

The semi-positive definite constitutive tangent elasticity operator $\boldsymbol{\mathcal{C}}_k^{\text{SPD}}$ is then constructed as

$$\boldsymbol{\mathcal{C}}_k^{\text{SPD}} = \left[\frac{\partial \lambda_1}{\partial \boldsymbol{F}}, \ \frac{\partial \lambda_2}{\partial \boldsymbol{F}}\right][\boldsymbol{H}_W^{\text{SPD}}]\begin{bmatrix}\frac{\partial \lambda_1}{\partial \boldsymbol{F}}\\ \frac{\partial \lambda_2}{\partial \boldsymbol{F}}\end{bmatrix}$$

For the initial stiffness tensor the eigenvalues cleanly separate as

$$\bar{\lambda}_1^{\boldsymbol{\mathcal{C}}_p} = \frac{\Sigma_{\lambda_1} - \Sigma_{\lambda_2}}{\lambda_1 - \lambda_2}, \qquad \bar{\lambda}_2^{\boldsymbol{\mathcal{C}}_p} = \frac{\Sigma_{\lambda_1} + \Sigma_{\lambda_2}}{\lambda_1 + \lambda_2}$$

with eigenmatrices as

$$[\boldsymbol{L}]_1 = \frac{1}{\sqrt{2}}\hat{\boldsymbol{U}}\begin{bmatrix}0 & 1\\ 1 & 0\end{bmatrix}\hat{\boldsymbol{V}}^T, \qquad [\boldsymbol{T}]_1 = \frac{1}{\sqrt{2}}\hat{\boldsymbol{U}}\begin{bmatrix}0 & -1\\ 1 & 0\end{bmatrix}\hat{\boldsymbol{V}}^T$$

where $\Sigma_{\lambda_i} = \partial_{\lambda_i} W$.
The semi-positive definite initial stiffness operator $\boldsymbol{\mathcal{C}}_p^{\text{SPD}}$ is then constructed as

$$\boldsymbol{\mathcal{C}_p}^{\text{SPD}} = \max(\bar{\lambda}_1^{\boldsymbol{\mathcal{C}_p}}, 0)[\boldsymbol{L}]_1 \otimes [\boldsymbol{L}]_1 + \max(\bar{\lambda}_2^{\boldsymbol{\mathcal{C}_p}}, 0)[\boldsymbol{T}]_1 \otimes [\boldsymbol{T}]_1$$

Note that, in 2-dimensions $\boldsymbol{F}$ is assumed to be 2×2 as for plane strain problems

$$\boldsymbol{F}_{\text{PLANE\_STRAIN}} = \begin{bmatrix}\boldsymbol{F}_{\text{2D}} & 0\\ 0 & 1\end{bmatrix}$$

the 3rd dimension decouples and does not contribute in SVD.

Eigensystem of tangent elasticity tensor (3D)

Given the Singular-Value-Decomposition (SVD) of $\boldsymbol{F}$

$$\boldsymbol{F} = \hat{\boldsymbol{U}}\boldsymbol{\Lambda}\hat{\boldsymbol{V}}^T, \quad \text{with} \quad \lambda_i = \Lambda_{ii} \quad i = 1,2,3$$

The first derivatives of principal stretches are

$$\frac{\partial \lambda_1}{\partial \boldsymbol{F}} = \hat{\boldsymbol{U}}\begin{bmatrix}1 & 0 & 0\\ 0 & 0 & 0\\ 0 & 0 & 0\end{bmatrix}\hat{\boldsymbol{V}}^T, \ \frac{\partial \lambda_2}{\partial \boldsymbol{F}} = \hat{\boldsymbol{U}}\begin{bmatrix}0 & 0 & 0\\ 0 & 1 & 0\\ 0 & 0 & 0\end{bmatrix}\hat{\boldsymbol{V}}^T, \ \frac{\partial \lambda_3}{\partial \boldsymbol{F}} = \hat{\boldsymbol{U}}\begin{bmatrix}0 & 0 & 0\\ 0 & 0 & 0\\ 0 & 0 & 1\end{bmatrix}\hat{\boldsymbol{V}}^T$$

For a given isotropic energy $W(\lambda_1, \lambda_2, \lambda_3)$ expressed in terms of principal stretches, the Hessian operator is

$$\boldsymbol{H}_W = \begin{bmatrix}\partial^2_{\lambda_1\lambda_1} W & \partial^2_{\lambda_1\lambda_2} W & \partial^2_{\lambda_1\lambda_3} W\\ & \partial^2_{\lambda_2\lambda_2} W & \partial^2_{\lambda_2\lambda_3} W\\ sym & & \partial^2_{\lambda_3\lambda_3} W\end{bmatrix}$$

If $\partial^2_{\lambda_1\lambda_2} W = \partial^2_{\lambda_1\lambda_3} W = \partial^2_{\lambda_2\lambda_3} W = 0$, then the eigen-decomposition of the Hessian is simply

$$\bar{\lambda}_1^{\boldsymbol{H}_W} = \partial^2_{\lambda_1\lambda_1} W, \qquad \boldsymbol{e}_1 = [1,0,0]^T$$
$$\bar{\lambda}_2^{\boldsymbol{H}_W} = \partial^2_{\lambda_2\lambda_2} W, \qquad \boldsymbol{e}_2 = [0,1,0]^T$$
$$\bar{\lambda}_3^{\boldsymbol{H}_W} = \partial^2_{\lambda_3\lambda_3} W, \qquad \boldsymbol{e}_3 = [0,0,1]^T$$

otherwise the eigen-decomposition of $\boldsymbol{H}_W$ is obtained in closed-form as (see Appendix B for analytical formula)

$$[\bar{\lambda}_i^{\boldsymbol{H}_W}, \boldsymbol{e}_i] = \texttt{eig}(\boldsymbol{H}_W)$$

The semi-positive definite Hessian operator is then constructed as

$$\boldsymbol{H}_W^{\text{SPD}} = \sum_{i=1}^{3} \max(\bar{\lambda}_i^{\boldsymbol{H}_W}, 0)\ \boldsymbol{e}_i \otimes \boldsymbol{e}_i$$

The semi-positive definite constitutive tangent elasticity operator $\boldsymbol{\mathcal{C}}_k^{\text{SPD}}$ is then constructed as

$$\boldsymbol{\mathcal{C}}_k^{\text{SPD}} = \left[\frac{\partial \lambda_1}{\partial \boldsymbol{F}}, \ \frac{\partial \lambda_2}{\partial \boldsymbol{F}}, \ \frac{\partial \lambda_3}{\partial \boldsymbol{F}}\right][\boldsymbol{H}_W^{\text{SPD}}]\begin{bmatrix}\frac{\partial \lambda_1}{\partial \boldsymbol{F}}\\ \frac{\partial \lambda_2}{\partial \boldsymbol{F}}\\ \frac{\partial \lambda_3}{\partial \boldsymbol{F}}\end{bmatrix}$$

For the initial stiffness tensor the eigenvalues cleanly separate as

$$\bar{\lambda}_1^{\boldsymbol{\mathcal{C}}_p} = \frac{\Sigma_{\lambda_2} - \Sigma_{\lambda_3}}{\lambda_2 - \lambda_3}, \qquad \bar{\lambda}_2^{\boldsymbol{\mathcal{C}}_p} = \frac{\Sigma_{\lambda_1} - \Sigma_{\lambda_3}}{\lambda_1 - \lambda_3}, \qquad \bar{\lambda}_3^{\boldsymbol{\mathcal{C}}_p} = \frac{\Sigma_{\lambda_1} - \Sigma_{\lambda_2}}{\lambda_1 - \lambda_2}$$
$$\bar{\lambda}_4^{\boldsymbol{\mathcal{C}}_p} = \frac{\Sigma_{\lambda_2} + \Sigma_{\lambda_3}}{\lambda_2 + \lambda_3}, \qquad \bar{\lambda}_5^{\boldsymbol{\mathcal{C}}_p} = \frac{\Sigma_{\lambda_1} + \Sigma_{\lambda_3}}{\lambda_1 + \lambda_3}, \qquad \bar{\lambda}_6^{\boldsymbol{\mathcal{C}}_p} = \frac{\Sigma_{\lambda_1} + \Sigma_{\lambda_2}}{\lambda_1 + \lambda_2}$$

with eigenmatrices as

$$[\boldsymbol{L}]_1 = \frac{1}{\sqrt{2}}\hat{\boldsymbol{U}}\begin{bmatrix}0 & 0 & 0\\ 0 & 0 & 1\\ 0 & 1 & 0\end{bmatrix}\hat{\boldsymbol{V}}^T, \quad [\boldsymbol{T}]_1 = \frac{1}{\sqrt{2}}\hat{\boldsymbol{U}}\begin{bmatrix}0 & 0 & 0\\ 0 & 0 & -1\\ 0 & 1 & 0\end{bmatrix}\hat{\boldsymbol{V}}^T,$$
$$[\boldsymbol{L}]_2 = \frac{1}{\sqrt{2}}\hat{\boldsymbol{U}}\begin{bmatrix}0 & 0 & 1\\ 0 & 0 & 0\\ 1 & 0 & 0\end{bmatrix}\hat{\boldsymbol{V}}^T, \quad [\boldsymbol{T}]_2 = \frac{1}{\sqrt{2}}\hat{\boldsymbol{U}}\begin{bmatrix}0 & 0 & -1\\ 0 & 0 & 0\\ 1 & 0 & 0\end{bmatrix}\hat{\boldsymbol{V}}^T,$$
$$[\boldsymbol{L}]_3 = \frac{1}{\sqrt{2}}\hat{\boldsymbol{U}}\begin{bmatrix}0 & 1 & 0\\ 1 & 0 & 0\\ 0 & 0 & 0\end{bmatrix}\hat{\boldsymbol{V}}^T, \quad [\boldsymbol{T}]_3 = \frac{1}{\sqrt{2}}\hat{\boldsymbol{U}}\begin{bmatrix}0 & -1 & 0\\ 1 & 0 & 0\\ 0 & 0 & 0\end{bmatrix}\hat{\boldsymbol{V}}^T$$

where $\Sigma_{\lambda_i} = \partial_{\lambda_i} W$.
The semi-positive definite initial stiffness operator $\boldsymbol{\mathcal{C}}_p^{\text{SPD}}$ is then constructed as

$$\boldsymbol{\mathcal{C}_p}^{\text{SPD}} = \sum_{i=1}^{3} \max(\bar{\lambda}_i^{\boldsymbol{\mathcal{C}_p}}, 0)[\boldsymbol{L}]_i \otimes [\boldsymbol{L}]_i + \sum_{i=1}^{3} \max(\bar{\lambda}_{i+3}^{\boldsymbol{\mathcal{C}_p}}, 0)[\boldsymbol{T}]_i \otimes [\boldsymbol{T}]_i$$

FIGURE 3 Complete procedure to construct *closed-form* eigensytems for constitutive tangent elasticity and initial stiffness operators in 2 and 3 dimensions from principal information. Note that, **tangent operators are symmetric**. Using $\bar{\lambda}_i^{\boldsymbol{\mathcal{C}}_p}$ and $\bar{\lambda}_i^{\boldsymbol{H}_W}$ for buidling the operators results in a standard Newton-Raphson (NR) scheme whereas using $\max(\bar{\lambda}_i^{\boldsymbol{\mathcal{C}}_p}, 0)$ and $\max(\bar{\lambda}_i^{\boldsymbol{H}_W}, 0)$ results in Projected Newton (PN). In other words, **the tangent stabilisation step is completely optional**.

in 3-dimensions. We can further reduce this to (by noting that $I_4 = I_2$) in 2-dimensions

$$W_{MR} = \alpha I_2 - 2\alpha \ln(I_5) + \frac{\kappa}{2}(I_5 - 1)^2, \tag{69}$$

with $\mu_1, \mu_2, \alpha, \kappa > 0$ being material parameters. The energy further expands in terms of principal stretches to

$$W_{MR} = \alpha(\lambda_1^2 + \lambda_2^2) - 2\alpha \ln(\lambda_1\lambda_2) + \frac{\kappa}{2}(\lambda_1\lambda_2 - 1)^2. \tag{70}$$

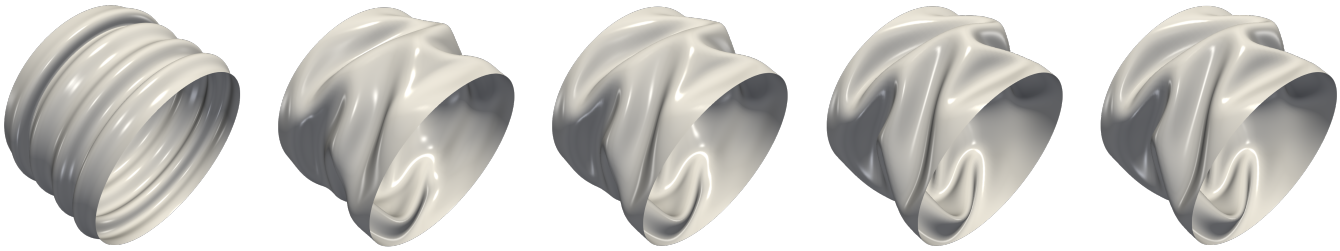

a) 1 increment b) 5 increments c) 10 increments d) 25 increments e) 50 increments

FIGURE 4 Simulating buckling of a pipe using tangent stabilised large strain elasticity. Tangent stabilisation makes it possible to apply the entire load at once however, at times, due to severe nonlinearity, Newton with tangent stabilisation (or without) can converge to a higher frequency eigen-mode of the system. However, the realisation is that stabilised tangent operators are merely a tight approximation to the real ones. By coupling the concept of load increments with tangent stabilisation it becomes possible to quickly recover the accurate buckling profile. In this example, buckled configuration is already captured within 3-5 load increments and the relative L^2 norm of difference in displacements between 25 and 50 increment is less than 10^{-8}.

The $\boldsymbol{H}_W$ tensor for this energy is then simply obtained as

$$\boldsymbol{H}_{W_{MR}} = \begin{bmatrix} \alpha(1+\frac{1}{\lambda_1^2}) + \kappa\lambda_2^2 & \kappa\left(2\lambda_1\lambda_2 - 1\right) \\ \kappa\left(2\lambda_1\lambda_2 - 1\right) & \alpha(1+\frac{1}{\lambda_2^2}) + \kappa\lambda_1^2 \end{bmatrix}, \tag{71}$$

and the two eigenvalues of the initial stiffness tensor are given by

$$\bar{\lambda}^{\boldsymbol{C}_p}_{MR_1} = \alpha(1 - \frac{1}{\lambda_1\lambda_2}) + \kappa(\lambda_1\lambda_2 - 1), \tag{72a}$$

$$\bar{\lambda}^{\boldsymbol{C}_p}_{MR_2} = \alpha(1 + \frac{1}{\lambda_1\lambda_2}) - \kappa(\lambda_1\lambda_2 - 1). \tag{72b}$$

The second energy which we will use for most of the example is the polyconvex, coercive, incompressible Moony-Rivlin model

$$W_{IMR} = \mu_1 {I_5}^{-2/3} I_2 + \mu_2 {I_5}^{-2} I_4^{3/2} + \kappa(I_5^{\eta} + I_5^{-\eta} - 2), \tag{73}$$

where $\eta > 1$ and $U(I_5) = \kappa(I_5^{\eta} + I_5^{-\eta} - 2)$ is the volumetric part. One specialisation of this energy in 2-dimensions is given by[60,61,62,44].

$$W_{IMR} = \alpha {I_5}^{-1} I_2 + \kappa(I_5 + I_5^{-1} - 2), \tag{74}$$

which in the context of quasi-conformal mappings[63,64] is typically referred to as MIPS energy[65]. This energy further expands in terms of principal stretches in dimensions to

$$W_{IMR} = \alpha(\frac{\lambda_1}{\lambda_2} + \frac{\lambda_2}{\lambda_1}) + \kappa\left((\lambda_1\lambda_2) + (\lambda_1\lambda_2)^{-1} - 2\right). \tag{75}$$

The $\boldsymbol{H}_W$ tensor for this energy is then simply obtained as

$$\boldsymbol{H}_{W_{IMR}} = \begin{bmatrix} 2\left(\frac{\kappa\lambda_2}{\lambda_1^3} - \frac{\alpha}{\lambda_2\lambda_1^3}\right), & \kappa\left(1 + \frac{1}{\lambda_1^2\lambda_2^2}\right) - \alpha(\frac{1}{\lambda_1^2} + \frac{1}{\lambda_2^2}), \\ \kappa\left(1 + \frac{1}{\lambda_1^2\lambda_2^2}\right) - \alpha(\frac{1}{\lambda_1^2} + \frac{1}{\lambda_2^2}) & 2\left(\frac{\kappa\lambda_1}{\lambda_2^3} - \frac{\alpha}{\lambda_1\lambda_2^3}\right) \end{bmatrix}, \tag{76}$$

and the two eigenvalues of the initial stiffness tensor are given by

$$\bar{\lambda}^{\boldsymbol{C}_p}_{IMR_1} = \alpha\left(\frac{-1}{\lambda_1^2} + \frac{-1}{\lambda_2^2} + \frac{2}{\lambda_1\lambda_2}\right) + \kappa\left(1 - \frac{1}{\lambda_1^2\lambda_2^2}\right), \tag{77a}$$

$$\bar{\lambda}^{\boldsymbol{C}_p}_{IMR_2} = \alpha\left(\frac{1}{\lambda_1^2} + \frac{1}{\lambda_2^2} + \frac{2}{\lambda_1\lambda_2}\right) - \kappa\left(1 - \frac{1}{\lambda_1^2\lambda_2^2}\right). \tag{77b}$$

In Figs. 5 and 6 we show the convex regions for compressible (first model) and incompressible (second model) Mooney-Rivlin material by plotting $\det(\boldsymbol{H}_W) = \prod \bar{\lambda}_i^{\boldsymbol{H}_W}$ as function of principal stretches λ_1 and λ_2 for standard (i.e. non-stabilised) and

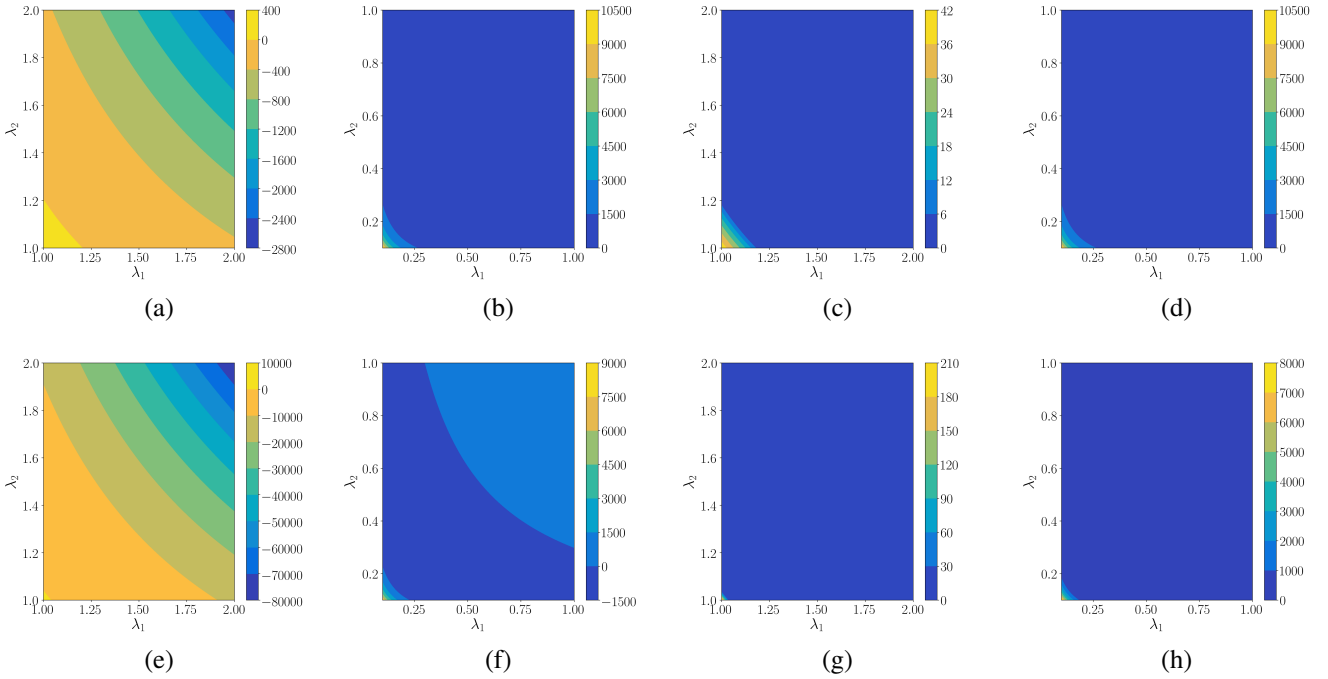

FIGURE 5 Effect of tangent stabilisation : original (non-convex) compressible Mooney-Rivlin model with indefinite Hessian $\boldsymbol{H}_{W_{MR}}$ (a,b,e,f) from Eqn. 71 and stabilised version with projected Hessian $\boldsymbol{H}^{\mathtt{SPD}}_{W_{MR}}$ (c,d,g,h) as a function of principal stretches. Plots (a,b,c,d) are for Poisson's ratio $\nu = 0.45$ and (e,f,g,h) for Poisson's ratio $\nu = 0.49$. Plots (a,c,e,g) are for compression scenario $\lambda_1, \lambda_2 < 1$ and plots (b,d,f,h) for tension scenario $\lambda_1, \lambda_2 > 1$. Colours can be loosely interpreted as matrix conditioning with regions above zero indicating semi-positive definiteness of the operator.

stabilised (i.e. SPD) Hessian for two Poisson's ratios ($\nu = 0.45$ and $\nu = 0.49$) and fixed $\alpha = 1$. As can be observed convexity zone shrinks as Poisson's ratio is pushed towards the incompressible limit and matrix conditioning also deteriorates but stabilisation also helps with conditioning. Compression and tension scenarios are depicted separately. It can be seen that, stabilisation does not impact zones where energy is already convex which is advantageous from numerical stand-point as quadratic convergence of Newton-Raphson is retained in such scenarios.

Similarly, In Figs. 7 and 8 we show the convexity of the initial stiffness operator $\boldsymbol{C}_p$ that is $\det(\boldsymbol{C}_p) = \prod \bar{\lambda}_i^{\boldsymbol{C}_p}$ for compressible (first model) and incompressible (second model) Mooney-Rivlin material as function of principal stretches λ_1 and λ_2 and the subsequent stabilised (i.e. SPD) initial stiffness for two Poisson's ratios ($\nu = 0.45$ and $\nu = 0.49$) and fixed $\alpha = 1$. As can be observed stabilisation does not impact zones where the initial stiffness is already positive definite however eliminates all sources of geometric instability when the matrix is not semi-positive definite.

4 | VARIATIONAL FORMULATIONS

4.1 | Standard displacement-based variational principle

The solution of large strain elastic problems is often expressed by means of the total energy minimisation variational principle as

$$\Pi(\boldsymbol{x}^\star) = \min_{\boldsymbol{x}} \int_V W(\mathcal{A}_{\boldsymbol{x}})\, \mathrm{d}V - \int_V \boldsymbol{f}_0 \cdot \boldsymbol{x}\, \mathrm{d}V - \int_{\partial_t V} \boldsymbol{t}_0 \cdot \boldsymbol{x}\, \mathrm{d}A, \tag{78}$$

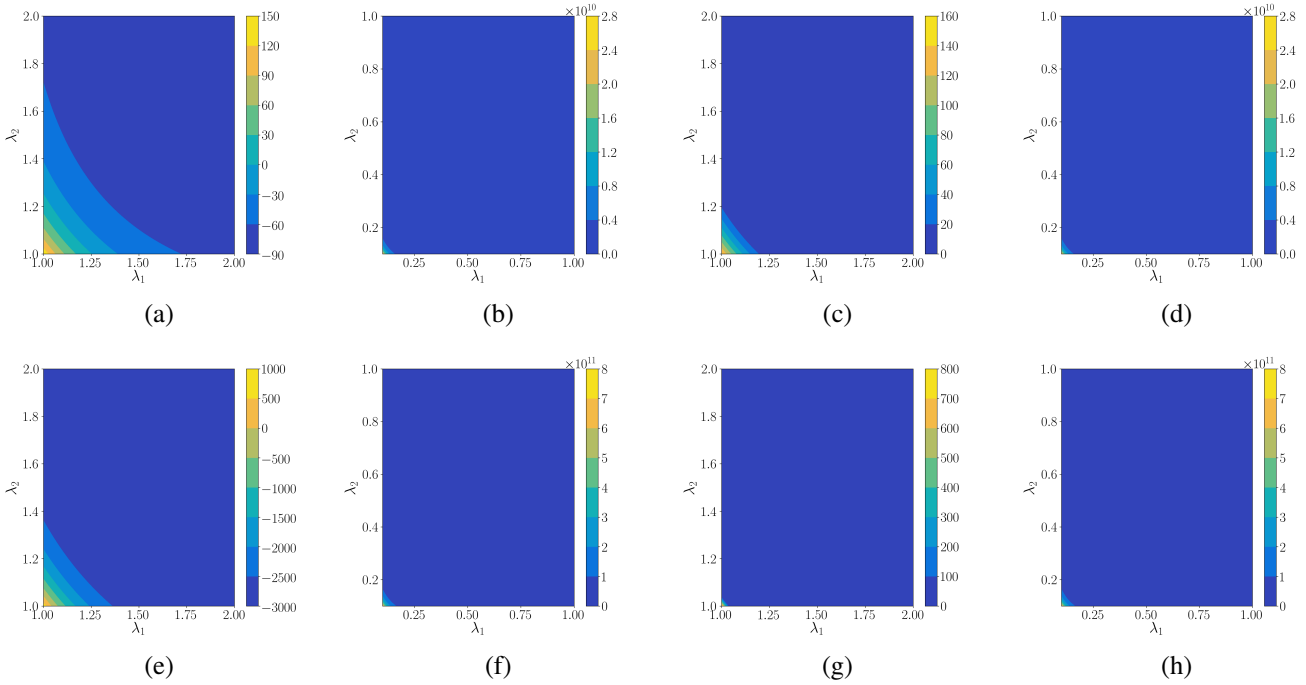

FIGURE 6 Effect of tangent stabilisation : original (non-convex) incompressible Mooney-Rivlin model with indefinite Hessian $\boldsymbol{H}_{W_{IMR}}$ (a,b,e,f) from Eqn. 76 and stabilised version with projected Hessian $\boldsymbol{H}^{\mathrm{SPD}}_{W_{IMR}}$ (c,d,g,h) as a function of principal stretches. Plots (a,b,c,d) are for Poisson's ratio $\nu = 0.45$ and (e,f,g,h) for Poisson's ratio $\nu = 0.49$. Plots are (a,c,e,g) for compression scenario $\lambda_1, \lambda_2 < 1$ and plots (b,d,f,h) for tension scenario $\lambda_1, \lambda_2 > 1$. Colours can be loosely interpreted as matrix conditioning with regions above zero indicating semi-positive definiteness of the operator.

where $\boldsymbol{x}^\star$ denotes the exact solution. The stationary condition of this functional leads to the principle of virtual work, commonly written as

$$D\Pi[\delta\boldsymbol{u}] = \int_V \boldsymbol{P}^{\boldsymbol{x}} : \delta\boldsymbol{\nabla}_0\boldsymbol{u}\, \mathrm{d}V - \int_V \boldsymbol{f}_0 \cdot \delta\boldsymbol{u}\, \mathrm{d}V - \int_{\partial_t V} \boldsymbol{t}_0 \cdot \delta\boldsymbol{u}\, \mathrm{d}A = 0. \tag{79}$$

In this expression, the first Piola-Kirchhoff tensor $\boldsymbol{P}^{\boldsymbol{x}}$ is evaluated in the standard fashion using Eqn. 26 in terms of the gradient of the deformation $\boldsymbol{\nabla}_0\boldsymbol{x}$ and in our setting its singular-values. For better clarification of the notation, it is useful to introduce the definition of the geometrically compatible strain and stretch measures as

$$\boldsymbol{F}_{\boldsymbol{x}} = \hat{\boldsymbol{U}}_{\boldsymbol{x}}\boldsymbol{\Lambda}_{\boldsymbol{x}}\hat{\boldsymbol{V}}_{\boldsymbol{x}}^{\,T} = \boldsymbol{\nabla}_0\boldsymbol{x}, \quad \boldsymbol{R}_{\boldsymbol{x}} = \hat{\boldsymbol{U}}_{\boldsymbol{x}}\hat{\boldsymbol{V}}_{\boldsymbol{x}}^{\,T}, \quad \boldsymbol{U}_{\boldsymbol{x}} = \hat{\boldsymbol{V}}_{\boldsymbol{x}}\boldsymbol{\Lambda}_{\boldsymbol{x}}\hat{\boldsymbol{V}}_{\boldsymbol{x}}^{\,T}, \quad \text{and} \quad \lambda_{\boldsymbol{x}_i} = \Lambda_{x_{ii}}. \tag{80}$$

In this manner, the first Piola-Kirchhoff tensor $\boldsymbol{P}^{\boldsymbol{x}}$ becomes

$$\boldsymbol{P}^{\boldsymbol{x}} = \sum_{i=1}^{d} \Sigma^{\boldsymbol{x}}_{\lambda_i} \frac{\partial \lambda_{\boldsymbol{x}_i}}{\partial \boldsymbol{F}_{\boldsymbol{x}}} = \hat{\boldsymbol{U}}_{\boldsymbol{x}}\boldsymbol{\Lambda}_{\boldsymbol{P}^{\boldsymbol{x}}}\hat{\boldsymbol{V}}_{\boldsymbol{x}}^{\,T}, \tag{81}$$

where the superscript (subscript) $\boldsymbol{x}$ is used for stresses (strains) to indicate that they are evaluated in terms of geometry

$$\Sigma^{x}_{\lambda_i} = \Sigma_{\lambda_i}(\lambda_{x_i}). \tag{82}$$

An iterative Newton-Raphson process to converge towards the solution is usually established by solving a linearised system for the increment $\Delta\boldsymbol{u}$ as

$$D^2\Pi[\delta\boldsymbol{u}; \Delta\boldsymbol{u}] = -D\Pi(\boldsymbol{x})[\delta\boldsymbol{u}], \qquad \boldsymbol{x}_{k+1} = \boldsymbol{x}_k + \Delta\boldsymbol{u}, \tag{83}$$

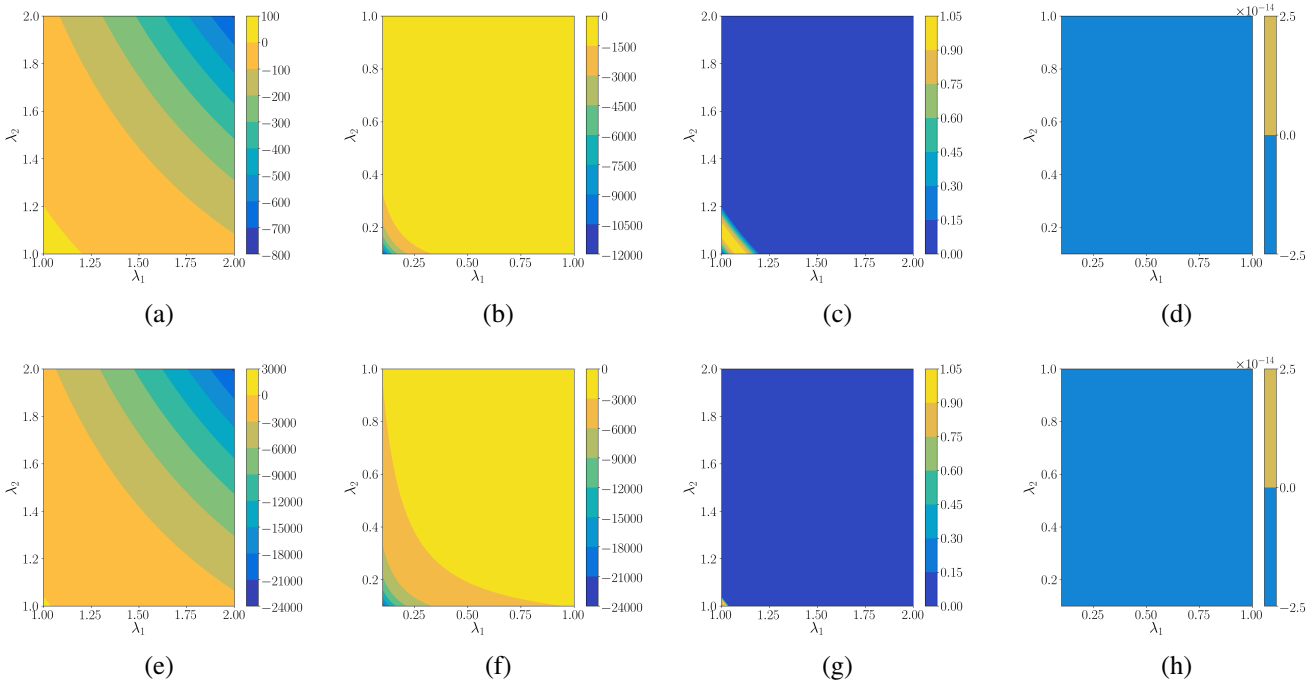

FIGURE 7 Effect of initial stiffness stabilisation : original (non-convex) compressible Mooney-Rivlin model with indefinite initial stiffness $\boldsymbol{C}_{P_{MR}}$ (a,b,e,f) from Eqn. 72 and stabilised version with projected initial stiffness $\boldsymbol{C}^{\text{SPD}}_{P_{MR}}$ (c,d,g,h) as a function of principal stretches. Plots (a,b,c,d) are for Poisson's ratio $\nu = 0.45$ and (e,f,g,h) for Poisson's ratio $\nu = 0.49$. plots (a,c,e,g) are for compression scenario $\lambda_1, \lambda_2 < 1$ and Plots (b,d,f,h) for tension scenario $\lambda_1, \lambda_2 > 1$. Colours can be loosely interpreted as matrix conditioning with regions above zero indicating semi-positive definiteness of the operator.

where, in the absence of follower forces, the second derivative of the total energy functional is given by

$$D^2\Pi[\delta\boldsymbol{u}; \Delta\boldsymbol{u}] = \int_V D^2 e[\delta\boldsymbol{u}, \Delta\boldsymbol{u}] \, \mathrm{d}V. \tag{84}$$

The tangent operator is evaluated taking $\boldsymbol{F}_{\boldsymbol{x}} = \boldsymbol{\nabla}_0 \boldsymbol{x}$ and $\lambda_{\boldsymbol{x}_i}$ concisely as it appears in Fig. 3.

4.2 | Mixed variational principle

An equivalent but alternative expression for the total energy variational principle can be written in terms of the geometry and principal stretches as a constrained minimisation problem in the form:

$$\Pi(\boldsymbol{x}^\star) = \min_{\boldsymbol{x},\mathcal{A}} \int_V W(\mathcal{A}) \, \mathrm{d}V - \int_V \boldsymbol{f}_0 \cdot \boldsymbol{x} \, \mathrm{d}V - \int_{\partial_t V} \boldsymbol{t}_0 \cdot \boldsymbol{x} \, \mathrm{d}A. \tag{85}$$

Using a standard Lagrange multiplier approach to enforce the compatibility constraints gives the following augmented mixed variational principle:

$$\Pi_M(\boldsymbol{x}^\star, \mathcal{A}^\star, S^\star) = \min_{\boldsymbol{x},\mathcal{A}} \left\{ \max_{S} \left\{ \int_V W(\mathcal{A}) \, \mathrm{d}V + \sum_{i=1}^{d} \int_V \Sigma_{\lambda_i} (\lambda_{\boldsymbol{x}_i} - \lambda_i) \, \mathrm{d}V - \int_V \boldsymbol{f}_0 \cdot \boldsymbol{x} \, \mathrm{d}V - \int_{\partial_t V} \boldsymbol{t}_0 \cdot \boldsymbol{x} \, \mathrm{d}A \right\} \right\}. \tag{86}$$

This expression belongs to the general class of Hu-Washizu type of mixed variational principles which have been widely used for the development of enhanced finite element formulations. Note that, the conjugate variables Σ_{λ_i} in this expression, at this stage, are simply Lagrange multipliers and are as yet unconnected to the principal stretch variables. The stationary condition of the above augmented Lagrangian with respect to the first variable enforces equilibrium in the form of the principle of virtual

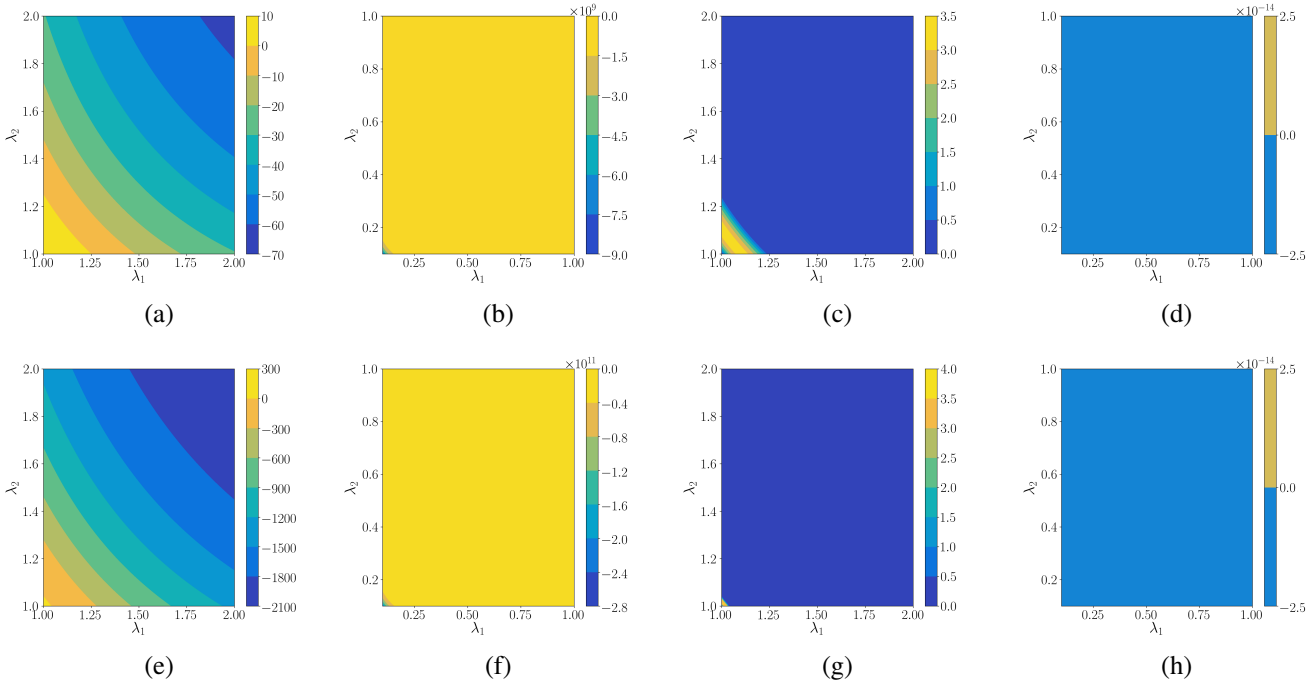

FIGURE 8 Effect of initial stiffness stabilisation : original (non-convex) incompressible Mooney-Rivlin model with indefinite initial stiffness $\boldsymbol{C}_{P_{IMR}}$ (a,b,e,f) from Eqn. 77 and stabilised version with projected initial stiffness $\boldsymbol{C}^{\text{SPD}}_{P_{IMR}}$ (c,d,g,h) as a function of principal stretches. Plots (a,b,c,d) are for Poisson's ratio $\nu = 0.45$ and (e,f,g,h) for Poisson's ratio $\nu = 0.49$. Plots (a,c,e,g) are for compression scenario $\lambda_1, \lambda_2 < 1$ and plots (b,d,f,h) for tension scenario $\lambda_1, \lambda_2 > 1$. Colours can be loosely interpreted as matrix conditioning with regions above zero indicating semi-positive definiteness of the operator.

work as

$$D_1\Pi_M[\delta\boldsymbol{u}] = \int_V \boldsymbol{P}^M \,:\, \boldsymbol{\nabla}_0\delta\boldsymbol{u}\,\mathrm{d}V - \int_V \boldsymbol{f}_0\cdot\delta\boldsymbol{u}\,\mathrm{d}V - \int_{\partial_t V}\boldsymbol{t}_0\cdot\delta\boldsymbol{u}\,\mathrm{d}A = 0, \tag{87}$$

where the first Piola-Kirchhoff stress now emerges as

$$\boldsymbol{P}^M = \sum_{i=1}^{d}\Sigma_{\lambda_i}\frac{\partial\lambda_i^{\boldsymbol{x}}}{\partial\boldsymbol{F}} = \hat{\boldsymbol{U}}_{\boldsymbol{x}}\boldsymbol{\Lambda}_{\boldsymbol{P}}\hat{\boldsymbol{V}}_{\boldsymbol{x}}^{\,T}. \tag{88}$$

Note that, in sharp contrast to enhanced formulations in terms of $\boldsymbol{F}$ (and/or its minors) as pursued in[6,4] in our setting the left and right singular-matrices namely $\hat{\boldsymbol{U}}_{\boldsymbol{x}}$ and $\hat{\boldsymbol{V}}_{\boldsymbol{x}}$ are still computed from the geometry. The stationary conditions with respect to the principal stretches enforce the constitute relationships between the conjugates and the derivatives of the energy in a weak form

$$D_2\Pi_M[\delta\mathcal{A}] = \sum_{i=1}^{d}\int_V\left(\frac{\partial W}{\partial\lambda_i} - \Sigma_{\lambda_i}\right)\cdot\delta\lambda_i\,\mathrm{d}V = 0. \tag{89}$$

Finally, the stationary conditions with respect to the stress variables enforce the geometric compatibility conditions between strains and geometry

$$D_3\Pi_M[\delta S] = \sum_{i=1}^{d}\int_V \delta\Sigma_{\lambda_i}\cdot(\lambda_{\boldsymbol{x}_i} - \lambda_i)\,\mathrm{d}V. \tag{90}$$

Once again, for second order iterative methods the appropriate tangent operators are needed. An equivalent process to displacement-based formulation can be followed for the extended set of variables to obtain a linear system for the increments of

variables $\{\Delta\boldsymbol{u}, \Delta\mathcal{A}, \Delta\mathcal{S}\}$ as

$$D^2_{1,2,3;1,2,3}\Pi_M[\delta\boldsymbol{u}, \delta\mathcal{A}, \delta\mathcal{S}; \Delta\boldsymbol{u}, \Delta\mathcal{A}, \Delta\mathcal{S}] = -D_{1,2,3}\Pi_M[\delta\boldsymbol{u}, \delta\mathcal{A}, \delta\mathcal{S}]. \tag{91}$$

The second derivatives that make up the linear operator in equation (97) can be derived with relative ease component by component. For instance, the second derivative with respect to the geometry, is obtained differentiating again the principle of virtual work, equation (92), with the help of equation (93) to give the "initial stress" component of the tangent operator as

$$\begin{aligned} D^2_{1;1}\Pi_M[\delta\boldsymbol{u}; \Delta\boldsymbol{u}] &= \int_V \boldsymbol{\nabla}_0\delta\boldsymbol{u} : \left(\sum_{i=1}^{d} \Sigma_{\lambda_i} \frac{\partial^2 \lambda_{\boldsymbol{x}_i}}{\partial \boldsymbol{F}_{\boldsymbol{x}} \partial \boldsymbol{F}_{\boldsymbol{x}}}\right)^{\text{SPD}} : \boldsymbol{\nabla}_0\Delta\boldsymbol{u}\, \mathrm{d}V \\ &= \int_V \boldsymbol{\nabla}_0\delta\boldsymbol{u} : \left(\sum_{i=1}^{k} \max(\bar{\lambda}^{\boldsymbol{C}_p}_{x_i}, 0)[\boldsymbol{L}]_i \otimes [\boldsymbol{L}]_i + \max(\bar{\lambda}^{\boldsymbol{C}_p}_{x_{i+k}}, 0)[\boldsymbol{T}]_i \otimes [\boldsymbol{T}]_i\right) : \boldsymbol{\nabla}_0\Delta\boldsymbol{u}\, \mathrm{d}V, \end{aligned} \tag{92}$$

where $\bar{\lambda}^{\boldsymbol{C}_p}_{x_i}$ indicates the evaluation initial stiffness eigensystem with respect to geometry. More specifically, this implies that in 2-dimensions the initial stiffness eigenvalues should be computed as

$$\bar{\lambda}^{\boldsymbol{C}_p}_{x_1} = \frac{\Sigma_{\lambda_1} + \Sigma_{\lambda_2}}{\lambda_{\boldsymbol{x}_1} + \lambda_{\boldsymbol{x}_2}}, \qquad \bar{\lambda}^{\boldsymbol{C}_p}_{x_2} = \frac{\Sigma_{\lambda_1} - \Sigma_{\lambda_2}}{\lambda_{\boldsymbol{x}_1} - \lambda_{\boldsymbol{x}_2}}, \tag{93}$$

and in 3-dimensions

$$\bar{\lambda}^{\boldsymbol{C}_p}_{x_1} = \frac{\Sigma_{\lambda_2} + \Sigma_{\lambda_3}}{\lambda_{\boldsymbol{x}_2} + \lambda_{\boldsymbol{x}_3}}, \qquad \bar{\lambda}^{\boldsymbol{C}_p}_{x_2} = \frac{\Sigma_{\lambda_1} + \Sigma_{\lambda_3}}{\lambda_{\boldsymbol{x}_1} + \lambda_{\boldsymbol{x}_3}}, \qquad \bar{\lambda}^{\boldsymbol{C}_p}_{x_3} = \frac{\Sigma_{\lambda_1} + \Sigma_{\lambda_2}}{\lambda_{\boldsymbol{x}_1} + \lambda_{\boldsymbol{x}_2}}, \tag{94a}$$

$$\bar{\lambda}^{\boldsymbol{C}_p}_{x_4} = \frac{\Sigma_{\lambda_2} - \Sigma_{\lambda_3}}{\lambda_{\boldsymbol{x}_2} - \lambda_{\boldsymbol{x}_3}}, \qquad \bar{\lambda}^{\boldsymbol{C}_p}_{x_5} = \frac{\Sigma_{\lambda_1} - \Sigma_{\lambda_3}}{\lambda_{\boldsymbol{x}_1} - \lambda_{\boldsymbol{x}_3}}, \qquad \bar{\lambda}^{\boldsymbol{C}_p}_{x_6} = \frac{\Sigma_{\lambda_1} - \Sigma_{\lambda_2}}{\lambda_{\boldsymbol{x}_1} - \lambda_{\boldsymbol{x}_2}}. \tag{94b}$$

The terms involving second derivatives with respect to the strain variables emerge from the Hessian of the energy function $W(\mathcal{A})$ as

$$D^2_{2;2}\Pi_M[\delta\mathcal{A}; \Delta\mathcal{A}] = \int_V [\delta\lambda_i, \cdots, \delta\lambda_d][\boldsymbol{H}^{\text{SPD}}_W] \begin{bmatrix} \Delta\lambda_1 \\ \vdots \\ \Delta\lambda_d \end{bmatrix} \mathrm{d}V. \tag{95}$$

The second derivative with respect to stresses vanishes as the functional is linear with respect to the stress tensors. There are, however, a number of cross derivative terms that do not vanish. These are, the cross derivatives with respect to stretches and stresses and their symmetric counterpart, which are easily derived from either Equation (89) or (90) to give:

$$D^2_{2;3}\Pi_M[\delta\mathcal{A}; \Delta\mathcal{S}] = -\sum_{i=1}^{d} \int_V \delta\lambda_i \cdot \Delta\Sigma_{\lambda_i}\, \mathrm{d}V, \tag{96}$$

$$D^2_{3;2}\Pi_M[\delta\mathcal{S}; \Delta\mathcal{A}] = -\sum_{i=1}^{d} \int_V \delta\Sigma_{\lambda_i} \cdot \delta\lambda_i\, \mathrm{d}V. \tag{97}$$

And the cross derivatives with respect to geometry and stresses, which emerge after some simple algebra

$$D^2_{1;3}\Pi_M[\delta\boldsymbol{u}; \Delta\mathcal{S}] = \sum_{i=1}^{d} \int_V \left(\frac{\partial \lambda_{\boldsymbol{x}_i}}{\partial \boldsymbol{F}_{\boldsymbol{x}}} \boldsymbol{\nabla}_0\delta\boldsymbol{u}\right) : \Delta\Sigma_{\lambda_i}\, \mathrm{d}V, \tag{98}$$

$$D^2_{3;1}\Pi_M[\delta\mathcal{S}; \Delta\boldsymbol{u}] = \sum_{i=1}^{d} \int_V \delta\Sigma_{\lambda_i} : \left(\frac{\partial \lambda_{\boldsymbol{x}_i}}{\partial \boldsymbol{F}_{\boldsymbol{x}}} \boldsymbol{\nabla}_0\Delta\boldsymbol{u}\right) \mathrm{d}V, \tag{99}$$

where $\frac{\partial \lambda_{\boldsymbol{x}_i}}{\partial \boldsymbol{F}_{\boldsymbol{x}}}$ are simply the scaling vectors from Eqns. 16-17.

4.2.1 | Variational principles for partially rigid, truly rigid and stiff material models

A variational principle can be easily established as particular case of the already described one for the case of truly rigid materials as

$$\Pi_M^R(\boldsymbol{x}^\star, S^\star) = \min_{\boldsymbol{x}} \left\{ \max_{S} \left\{ \int_V \bar{W}(\mathcal{A}_x)\, \mathrm{d}V + \sum_{i=1}^{k} \int_V \Sigma_{\lambda_i}(\lambda_{\boldsymbol{x}_i} - 1) - \frac{1}{2C_c}\Sigma_{\lambda_i}^2\, \mathrm{d}V - \int_V \boldsymbol{f}_0 \cdot \boldsymbol{x}\, \mathrm{d}V - \int_{\partial_t V} \boldsymbol{t}_0 \cdot \boldsymbol{x}\, \mathrm{d}A \right\} \right\}, \quad (100)$$

where $k \leq d$ implies partial rigidity i.e. rigidity can be considered in a particular principal direction(s) too. The most practically relevant case is however, the truly rigid (or just rigid) and stiff formulation ($k = d$). Rigid models in generals do not have a deformable part and as mentioned earlier the polar decomposition of $\boldsymbol{F}$ itself provides the right (deformational-rotational) decomposition and it possible to drop the $\bar{W}(\mathcal{A}_x)$ all together to arrive at

$$\Pi_M^R(\boldsymbol{x}^\star, S^\star) = \min_{\boldsymbol{x}} \left\{ \max_{S} \left\{ \sum_{i=1}^{d} \int_V \Sigma_{\lambda_i}(\lambda_{\boldsymbol{x}_i} - 1) - \frac{1}{2C_c}\Sigma_{\lambda_i}^2\, \mathrm{d}V - \int_V \boldsymbol{f}_0 \cdot \boldsymbol{x}\, \mathrm{d}V - \int_{\partial_t V} \boldsymbol{t}_0 \cdot \boldsymbol{x}\, \mathrm{d}A \right\} \right\}, \quad (101)$$

where $C_c > 0$ is an additional penalty term to avoid saddle point problem and the formulation above falls under the general category of Perturbed Lagrangian formulation. Note that, this formulation can be treated as linear in λ_is and Σ_{λ_i}s hence, resulting in an efficient implementation. The stationary conditions of this hybrid functional is evaluated in the same fashion as previous formulation. For instance, the first derivative with respect to geometry gives the principle of virtual work as

$$D_1\Pi_M^R[\delta\boldsymbol{u}] = \int_V \boldsymbol{P}^R : \boldsymbol{\nabla}_0\delta\boldsymbol{u}\, \mathrm{d}V - \int_V \boldsymbol{f}_0 \cdot \delta\boldsymbol{u}\, \mathrm{d}V - \int_{\partial_t V} \boldsymbol{t}_0 \cdot \delta\boldsymbol{u}\, \mathrm{d}A = 0, \quad (102)$$

where the first Piola-Kirchoff stress tensor is now evaluated as

$$\boldsymbol{P}^R = \sum_{i=1}^{d} \Sigma_{\lambda_i} \frac{\partial \lambda_{\boldsymbol{x}_i}}{\partial \boldsymbol{F}_{\boldsymbol{x}}}. \quad (103)$$

The first derivative with respect to Σ_{λ_i} enforces the rigidity constraint

$$D_2\Pi_M^R[\delta\Sigma_{\lambda_i}] = \sum_{i=1}^{d} \int_V \delta\Sigma_{\lambda_i} \left((\lambda_{x_i} - 1) - \frac{1}{C_c}\Sigma_{\lambda_i} \right) \mathrm{d}V. \quad (104)$$

The evaluation of second derivatives required for a Newton-Raphson process proceeds along the same lines. For instance, the second derivative with respect to geometry leads to the initial stiffness operator

$$\begin{aligned} D_{1;1}^2\Pi_M^R[\delta\boldsymbol{u}; \Delta\boldsymbol{u}] &= \int_V \boldsymbol{\nabla}_0\delta\boldsymbol{u} : \left(\sum_{i=1}^{d} \Sigma_{\lambda_i} \frac{\partial^2 \lambda_{\boldsymbol{x}_i}}{\partial \boldsymbol{F}_{\boldsymbol{x}} \partial \boldsymbol{F}_{\boldsymbol{x}}} \right)^{\mathrm{SPD}} : \boldsymbol{\nabla}_0\Delta\boldsymbol{u}\, \mathrm{d}V \\ &= \int_V \boldsymbol{\nabla}_0\delta\boldsymbol{u} : \left(\sum_{i=1}^{k} \max(\bar{\lambda}_{x_i}^{\boldsymbol{C}_p}, 0)[\boldsymbol{L}]_i \otimes [\boldsymbol{L}]_i + \max(\bar{\lambda}_{x_{i+k}}^{\boldsymbol{C}_p}, 0)[\boldsymbol{T}]_i \otimes [\boldsymbol{T}]_i \right) : \boldsymbol{\nabla}_0\Delta\boldsymbol{u}\, \mathrm{d}V, \end{aligned} \quad (105)$$

which is exactly the same as Eqn. 92. The second derivative with respect to Σ_{λ_i} has a standard Galerkin mass matrix format

$$D_{2;2}^2\Pi_M^R[\delta\Sigma_{\lambda_i}; \Delta\Sigma_{\lambda_i}] = -\frac{1}{C_c} \sum_{i=1}^{d} \int_V \delta\Sigma_{\lambda_i} \cdot \Delta\Sigma_{\lambda_i}\, \mathrm{d}V, \quad (106)$$

and the cross terms are also exactly the same as Eqns. 98-99

$$D_{1;3}^2\Pi_M^R[\delta\boldsymbol{u}; \Delta S] = \sum_{i=1}^{d} \int_V \left(\frac{\partial \lambda_{\boldsymbol{x}_i}}{\partial \boldsymbol{F}_{\boldsymbol{x}}} \boldsymbol{\nabla}_0\delta\boldsymbol{u} \right) : \Delta\Sigma_{\lambda_i}\, \mathrm{d}V, \quad (107)$$

$$D_{3;1}^2\Pi_M^R[\delta S; \Delta\boldsymbol{u}] = \sum_{i=1}^{d} \int_V \delta\Sigma_{\lambda_i} : \left(\frac{\partial \lambda_{\boldsymbol{x}_i}}{\partial \boldsymbol{F}_{\boldsymbol{x}}} \boldsymbol{\nabla}_0\Delta\boldsymbol{u} \right) \mathrm{d}V. \quad (108)$$

5 | FINITE ELEMENT DISCRETISATION

The implementation of the various variational principles described in the previous section is based on a finite element partition of the domain into a set of elements. Inside each element the problem variables are interpolated in terms of a set of shape functions N_a as

$$\boldsymbol{x} = \sum_{a=1}^{n_x} \boldsymbol{x}_a N_a^x, \quad \lambda_i = \sum_{a=1}^{n_{\lambda_i}} \lambda_{i_a} N_a^{\lambda_i}, \quad \Sigma_{\lambda_i} = \sum_{a=1}^{n_{\Sigma_{\lambda_i}}} \lambda_{i_a} N_a^{\Sigma_{\lambda_i}}, \tag{109}$$

where a denotes the nodes or other degrees of freedom used in the interpolation of the above variables. In general, different interpolations are often used to describe different variables. However, the same interpolation space will invariably be used for strain-stress conjugate pairs; that is, $N_a^{\lambda_i} = N_a^{\Sigma_{\lambda_i}}$, etc. The virtual and incremental equivalents of the variables are also interpolated using the same spaces as

$$\begin{aligned}
\delta\boldsymbol{u} &= \sum_{a=1}^{n_x} \delta\boldsymbol{u}_a N_a^x, \quad \delta\lambda_i = \sum_{a=1}^{n_{\lambda_i}} \delta\lambda_{i_a} N_a^{\lambda_i}, \quad \delta\Sigma_{\lambda_i} = \sum_{a=1}^{n_{\Sigma_{\lambda_i}}} \delta\Sigma_{\lambda_{i_a}} N_a^{\Sigma_{\lambda_i}}, \\
\Delta\boldsymbol{u} &= \sum_{a=1}^{n_x} \Delta\boldsymbol{u}_a N_a^x, \quad \Delta\lambda_i = \sum_{a=1}^{n_{\lambda_i}} \Delta\lambda_{i_a} N_a^{\lambda_i}, \quad \Delta\Sigma_{\lambda_i} = \sum_{a=1}^{n_{\Sigma_{\lambda_i}}} \Delta\Sigma_{\lambda_{i_a}} N_a^{\Sigma_{\lambda_i}}.
\end{aligned} \tag{110}$$

Finite element equations are derived by simply substituting the above expressions into the functional expressions provided in the previous section. In many cases this is a rather standard process and leads to well established equations. For instance, substituting the above interpolation for the virtual displacements into any of the virtual work statements given in the previous section leads to residual forces as

$$D_1\Pi[\delta\boldsymbol{u}] = \sum_a \boldsymbol{R}_a^{\boldsymbol{x}} \cdot \delta\boldsymbol{u}, \qquad \boldsymbol{R}_a^{\boldsymbol{x}} = \int_{V^e} \boldsymbol{P}\boldsymbol{\nabla}_0 N_a^x \, \mathrm{d}V^e - \int_{V^e} \boldsymbol{f}_0 N_a^x \, \mathrm{d}V^e - \int_{\partial_t V^e} \boldsymbol{t}_0 N_a^x \, \mathrm{d}A^e, \tag{111}$$

where the first Piola-Kirchhoff stress tensor above will be evaluated in accordance with each of the formulations presented in the previous section and V^e and A^e denote the volume and area of element e in the original configuration. Similar expressions for other residual terms can be easily derived. For instance, the geometric compatibility residuals $\boldsymbol{R}_a^{\lambda_i}$ emerge from the discretisation of Eqns. 89 and 90 and similar equations emerge in the case of the mixed potential for the constitutive equation residuals $\boldsymbol{R}_a^{\Sigma_{\lambda_i}}$

$$\boldsymbol{R}_a^{\lambda_i} = \int_{V^e} \begin{bmatrix} (\frac{\partial W}{\partial \lambda_1} - \Sigma_{\lambda_1}) N_a^{\lambda_1} \\ \vdots \\ (\frac{\partial W}{\partial \lambda_d} - \Sigma_{\lambda_d}) N_a^{\lambda_d} \end{bmatrix} \mathrm{d}V^e, \qquad \boldsymbol{R}_a^{\Sigma_{\lambda_i}} = \int_{V^e} \begin{bmatrix} (\lambda_{\boldsymbol{x}_1} - \lambda_1) N_a^{\Sigma_{\lambda_1}} \\ \vdots \\ (\lambda_{\boldsymbol{x}_d} - \lambda_d) N_a^{\Sigma_{\lambda_d}} \end{bmatrix} \mathrm{d}V^e. \tag{112}$$

In order to complete the finite element formulation it is necessary to derive equations for the components of the tangent matrix by discretising the tangent operators defined in the previous section. For the case of principal stretch mixed formulation for instance, the resulting tangent operator can be represented as

$$D^2\Pi_M[\delta\boldsymbol{u}, \delta\mathcal{A}, \delta\mathcal{S}; \Delta\boldsymbol{u}, \Delta\mathcal{A}, \Delta\mathcal{S}] = \begin{bmatrix} \delta\boldsymbol{u} & \delta\mathcal{A} & \delta\mathcal{S} \end{bmatrix} \begin{bmatrix} \boldsymbol{K}_{\boldsymbol{xx}} & \boldsymbol{0} & \boldsymbol{K}_{\boldsymbol{x}\mathcal{S}} \\ \boldsymbol{0} & \boldsymbol{K}_{\mathcal{A}\mathcal{A}} & \boldsymbol{K}_{\mathcal{A}\mathcal{S}} \\ \boldsymbol{K}_{\mathcal{S}\boldsymbol{x}} & \boldsymbol{K}_{\mathcal{S}\mathcal{A}} & \boldsymbol{0} \end{bmatrix} \begin{bmatrix} \Delta\boldsymbol{u} \\ \Delta\mathcal{A} \\ \Delta\mathcal{S} \end{bmatrix}. \tag{113}$$

The individual matrices terms in the above tangent matrix are straightforward to obtain. The $\boldsymbol{K}_{\boldsymbol{xx}}$ is the initial stiffness matrix which is obtained in indicial form as

$$[\boldsymbol{K}_{\boldsymbol{xx}}^{ab}]_{ij} = \int_{V^e} [\boldsymbol{\nabla}_0 N_a^x]_k \left[\sum_{i=1}^{k} \max(\bar{\lambda}_{x_i}^{\boldsymbol{C}_p}, 0) [\boldsymbol{L}]_i \otimes [\boldsymbol{L}]_i + \max(\bar{\lambda}_{x_{i+k}}^{\boldsymbol{C}_p}, 0) [\boldsymbol{T}]_i \otimes [\boldsymbol{T}]_i \right]_{ikjl} [\boldsymbol{\nabla}_0 N_b^x]_l \mathrm{d}V^e. \tag{114}$$

Similarly, the term relating to the Hessian, namely $\boldsymbol{K}_{\mathcal{A}\mathcal{A}}$ can be written in indicial form

$$\boldsymbol{K}_{\mathcal{A}\mathcal{A}}^{ab} = \int_{V^e} \begin{bmatrix} N_a^{\lambda_1} N_b^{\lambda_1} \partial^2_{\lambda_1\lambda_1} W & \cdots & N_a^{\lambda_1} N_b^{\lambda_d} \partial^2_{\lambda_1\lambda_d} W \\ \vdots & \ddots & \vdots \\ sym & \cdots & N_a^{\lambda_d} N_b^{\lambda_d} \partial^2_{\lambda_d\lambda_d} W \end{bmatrix}^{\mathrm{SPD}} \mathrm{d}V^e, \tag{115}$$

or alternatively in matrix form

$$\boldsymbol{K}^{ab}_{\mathcal{A}\mathcal{A}} = \int_{V^e} \boldsymbol{M}\, \boldsymbol{H}^{\text{SPD}}_{W} \boldsymbol{M}^T \mathrm{d}V^e, \tag{116}$$

where $\boldsymbol{M}$ is the commonly used matrix of shape functions arranged as

$$\boldsymbol{M} = \begin{bmatrix} N_1 & 0 & 0 & N_2 & 0 & 0 & \cdots & N_{n_{\lambda_1}} & 0 & 0 \\ 0 & N_1 & 0 & 0 & N_2 & 0 & \cdots & 0 & N_{n_{\lambda_2}} & 0 \\ 0 & 0 & N_1 & 0 & 0 & N_2 & \cdots & 0 & 0 & N_{n_{\lambda_3}} \end{bmatrix}, \tag{117}$$

in 3-dimensions and

$$\boldsymbol{M} = \begin{bmatrix} N_1 & 0 & N_2 & 0 & \cdots & N_{n_{\lambda_1}} & 0 \\ 0 & N_1 & 0 & N_2 & \cdots & 0 & N_{n_{\lambda_2}} \end{bmatrix}, \tag{118}$$

in 2-dimensions. Finally, the two cross terms in the principal stretch mixed formulation are obtained as

$$\boldsymbol{K}^{ab}_{\mathcal{A}\mathcal{S}} = -\int_{V^e} \begin{bmatrix} N_a^{\lambda_1} N_b^{\Sigma_{\lambda_1}} & & \\ & \ddots & \\ & & N_a^{\lambda_d} N_b^{\Sigma_{\lambda_d}} \end{bmatrix} \mathrm{d}V^e, \tag{119}$$

$$\boldsymbol{K}^{ab}_{\boldsymbol{x}\mathcal{S}} = \int_{V^e} \left[\frac{\partial \lambda_{\boldsymbol{x}_1}}{\partial \boldsymbol{F}_x} \boldsymbol{\nabla}_0 N^x_a, \cdots, \frac{\partial \lambda_{\boldsymbol{x}_d}}{\partial \boldsymbol{F}_x} \boldsymbol{\nabla}_0 N^x_a \right] N_b^{\Sigma_{\lambda_i}} \mathrm{d}V^e. \tag{120}$$

For rigid and stiff formulations a slightly modified residual $\boldsymbol{R}_{\mathcal{S}}$ and a diagonal term relating to the perturbed Lagrangian $\boldsymbol{K}^{ab}_{\mathcal{S}\mathcal{S}}$ also emerge

$$\boldsymbol{R}^{ab}_{\mathcal{S}} = -\frac{1}{C_c} \int_{V^e} \begin{bmatrix} \left((\lambda_{\boldsymbol{x}_1} - 1 - \frac{\Sigma_{\lambda_1}}{C_c}) \right) N_a^{\Sigma_{\lambda_1}} \\ \vdots \\ \left((\lambda_{\boldsymbol{x}_d} - 1 - \frac{\Sigma_{\lambda_d}}{C_c}) \right) N_a^{\Sigma_{\lambda_d}} \end{bmatrix} \mathrm{d}V^e, \tag{121}$$

$$\boldsymbol{K}^{ab}_{\mathcal{S}\mathcal{S}} = -\frac{1}{C_c} \int_{V^e} \begin{bmatrix} N_a^{\Sigma_{\lambda_1}} N_b^{\Sigma_{\lambda_1}} & & \\ & \ddots & \\ & & N_a^{\Sigma_{\lambda_d}} N_b^{\Sigma_{\lambda_d}} \end{bmatrix} \mathrm{d}V^e. \tag{122}$$

The equations provided above can be implemented using a variety of finite element spaces. Certainly, not all choices will lead to effective or valid finite element formulations[37,39,40,41,66,67,68,69,70,71]. Moreover, the cost of implementation of mixed formulation may be significantly higher than that of standard displacement based approaches given the number of additional unknowns created. However, careful analysis of the continuity required for each of the variables, shows that only displacements need to be continuous across elements[72,73,74,75]. Stretches and their work conjugate variables can be discretised independently on each element of the mesh. This enables a static condensation process to be carried out before assembly of the global tangent matrix. The choice of function spaces are shown in Fig. 9 for triangular and tetrahedral elements. In particular, quadratic bases are used for the geometry discretisation, with linear element by element interpolations for the stretches and their conjugates. To illustrate the static condensation procedure, let us consider the mixed variational formulation with independent principal stretches whose linear system at an element level can be written as

$$\begin{bmatrix} \boldsymbol{K}_{\boldsymbol{x}\boldsymbol{x}} & \boldsymbol{0} & \boldsymbol{K}_{\boldsymbol{x}\mathcal{S}} \\ \boldsymbol{0} & \boldsymbol{K}_{\mathcal{A}\mathcal{A}} & \boldsymbol{K}_{\mathcal{A}\mathcal{S}} \\ \boldsymbol{K}_{\mathcal{S}\boldsymbol{x}} & \boldsymbol{K}_{\mathcal{S}\mathcal{A}} & \boldsymbol{0} \end{bmatrix} \begin{bmatrix} \Delta \boldsymbol{u} \\ \Delta \mathcal{A} \\ \Delta \mathcal{S} \end{bmatrix} = \begin{bmatrix} -\boldsymbol{R}_{\boldsymbol{x}} \\ -\boldsymbol{R}_{\mathcal{A}} \\ -\boldsymbol{R}_{\mathcal{S}} \end{bmatrix}, \tag{123}$$

In this case, the generalised displacement tangent operator obtained after static condensation for mixed variational formulation with independent principal stretches look like

$$\boldsymbol{K}_G = \boldsymbol{K}_{\boldsymbol{x}\boldsymbol{x}} + \boldsymbol{K}_{\boldsymbol{x}\mathcal{S}} \boldsymbol{K}^{-1}_{\mathcal{S}\mathcal{A}} \boldsymbol{K}_{\mathcal{A}\mathcal{A}} \boldsymbol{K}^{-1}_{\mathcal{A}\mathcal{S}} \boldsymbol{K}_{\mathcal{S}\boldsymbol{x}}, \tag{124a}$$

$$\boldsymbol{R}_G = \boldsymbol{R}_{\boldsymbol{x}} - \boldsymbol{K}_{\boldsymbol{x}\mathcal{S}} \boldsymbol{K}^{-1}_{\mathcal{S}\mathcal{A}} \left(\boldsymbol{R}_{\mathcal{A}} - \boldsymbol{K}_{\mathcal{A}\mathcal{A}} \boldsymbol{K}^{-1}_{\mathcal{A}\mathcal{S}} \boldsymbol{R}_{\mathcal{S}} \right), \tag{124b}$$

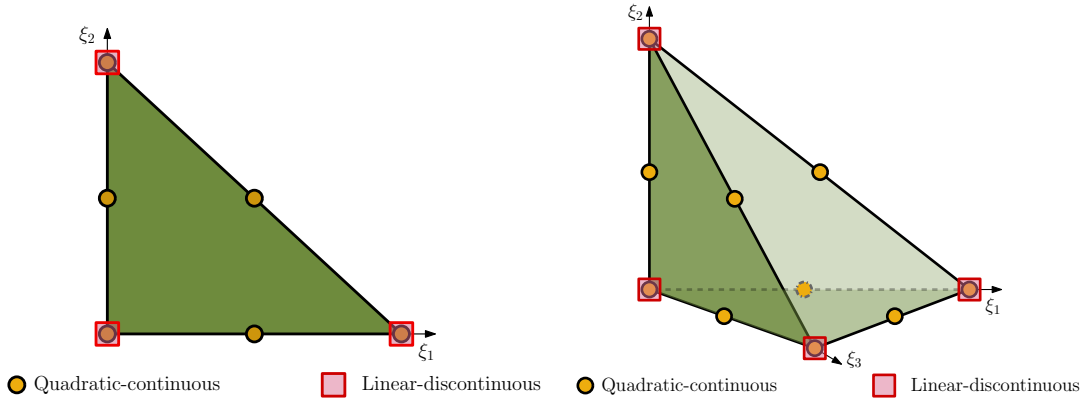

FIGURE 9 Mixed finite elements in 2 and 3 dimensions. Piece-wise continuous quadratic basis functions are used for displacements and piece-wise discontinuous linear basis functions for principal stretches and the corresponding Lagrange multipliers.

which can be assembled into a global linear system of equations as

$$\mathop{\mathsf{A}}\{\boldsymbol{K}_G\}\Delta\boldsymbol{x} = \mathop{\mathsf{A}}\{-\boldsymbol{R}_G\} \tag{125}$$

where A denotes assembly over elements. It is important to note that, given the linear shape functions for stretches and work conjugates for triangular and tetrahedral elements the $\boldsymbol{K}_{\mathcal{A}\mathcal{S}} = \boldsymbol{K}_{\mathcal{S}\mathcal{A}}$ matrix is the standard Galerkin mass matrix which is constant (can be computed at initialisation) and whose inverse can be found analytically. More specifically, for a given component λ_i and Σ_{λ_i} from the sets $\mathcal{A}$ and $\mathcal{S}$, respectively this matrix is simply given by

$$\boldsymbol{K}^{-1}_{\lambda_i\Sigma_{\lambda_i}} = \frac{3}{V^e}\begin{bmatrix} -3 & 1 & 1 \\ 1 & -3 & 1 \\ 1 & 1 & -3 \end{bmatrix}, \tag{126}$$

in 2-dimensions and by

$$\boldsymbol{K}^{-1}_{\lambda_i\Sigma_{\lambda_i}} = \frac{4}{V^e}\begin{bmatrix} -4 & 1 & 1 & 1 \\ 1 & -4 & 1 & 1 \\ 1 & 1 & -4 & 1 \\ 1 & 1 & 1 & -4 \end{bmatrix}, \tag{127}$$

in 3-dimensions where V^e is once again the volume of the element in the original configuration. Hence, after having solved for global displacement increments $\Delta\boldsymbol{x}$ at a given Newton-Raphson iteration, the increments for local (per-element) variables namely stretches $\Delta\mathcal{A}$ and stress conjugates $\Delta\mathcal{S}$ can be computed locally and efficiently through a few elementary matrix-multiplications as

$$\Delta\mathcal{A} = \boldsymbol{K}^{-1}_{\mathcal{A}\mathcal{S}}\left(-\boldsymbol{R}_{\mathcal{S}} - \boldsymbol{K}_{\mathcal{S}\boldsymbol{x}}\Delta\boldsymbol{x}^e\right), \tag{128a}$$

$$\Delta\mathcal{S} = \boldsymbol{K}^{-1}_{\mathcal{S}\mathcal{A}}\left(-\boldsymbol{R}_{\mathcal{A}} - \boldsymbol{K}_{\mathcal{A}\mathcal{A}}\Delta\mathcal{A}\right). \tag{128b}$$

This implies that the proposed mixed principal stretch formulation **does not require per-element matrix inversion or linear system solution**. As mentioned in the introduction, the solution strategy for this mixed finite elements is strikingly similar to local-global algorithms used in geometry processing applications[35,33] which solves for rotations locally and for displacements globally. However, as mentioned such algorithms are first order alternating/staggered approaches and cannot be recast as a second-order Newton-Raphson minimisation problem and from finite elements perspective they correspond to P1-P0 element which is known to have locking and accuracy issues for secondary variables. Hence, our scheme in essence, generalises over local-global approaches.

In general, given a semi-positive definite initial stiffness matrix $\boldsymbol{K}_{\boldsymbol{x}\boldsymbol{x}}$ and semi-positive definite matrices $\boldsymbol{K}_{\mathcal{A}\mathcal{A}}$ and $\boldsymbol{K}_{\mathcal{A}\mathcal{S}}$ the resulting generalised tangent matrix $\boldsymbol{K}_G$ is guaranteed to be semi-positive definite.

Algorithm 1 Procedure for computing stabilised tangent operators at a quadrature point

procedure GETENERGYFIRSTPIOLAPROJECTEDTANGENTS($\boldsymbol{F}$)
  Compute SVD $\boldsymbol{F} = \hat{\boldsymbol{U}}\boldsymbol{\Sigma}\hat{\boldsymbol{V}}^T$ ▷ Eqn. 3
  Compute energy $W(\mathcal{A})$ ▷ Eqn. 53
  Compute first Piola-Kirchhoff $\boldsymbol{P}$ ▷ Eqn. 26
  Compute analytical eigenvalues/vectors of the Hessian $\boldsymbol{H}_W$: $\bar{\lambda}_i^{\boldsymbol{H}_W}$ ▷ Eqns. 60-61
  Build the Hessian $\boldsymbol{H}_W^{\text{SPD}} \leftarrow \sum_i \max(\bar{\lambda}_i^{\boldsymbol{H}_W}, 0)\ \boldsymbol{e}_i \otimes \boldsymbol{e}_i$ ▷ Eqn. 59
  Build the constitutive tangent $\boldsymbol{C}_k^{\text{SPD}}$ ▷ Eqn. 62
  Compute analytical eigenvalues/vectors of the initial stiffness $\boldsymbol{C}_p$: $\bar{\lambda}_i^{\boldsymbol{C}_p}$ ▷ Eqns. 32-34, 14-15, 36
  Build the initial stiffness $\boldsymbol{C}_p^{\text{SPD}} \leftarrow \sum_{i=1}^{k} \max(\bar{\lambda}_i^{\boldsymbol{C}_p}, 0)[\boldsymbol{L}]_i \otimes [\boldsymbol{L}]_i + \sum_{i=1}^{k} \max(\bar{\lambda}_{i+k}^{\boldsymbol{C}_p}, 0)[\boldsymbol{T}]_i \otimes [\boldsymbol{T}]_i$. ▷ Eqn. 63
  Build the total tangent $\boldsymbol{C}^{\text{SPD}} \leftarrow \boldsymbol{C}_k^{\text{SPD}} + \boldsymbol{C}_p^{\text{SPD}}$
  return $\boldsymbol{C}^{\text{SPD}}$
end procedure

6 | COMPUTATIONAL ASPECTS

In this section, we discuss some of the key implementation aspects of the proposed framework. In particular, we outline: 1) A generalised Newton-Raphson procedure that encompasses standard Newton, Modified Newton and Projected Newton for the simulation of stabilised and non-stabilised nonlinear systems. 2) A line search technique to overcome stalls and blows-up during minimisation and finally 3) the choice of quadrature scheme to guarantee semi-positive definiteness for mixed and high order elements.

6.1 | Generalised Newton-Raphson with line search

As mentioned, the projected tangent operators can be seen as estimates (or proxies) to the real ones. Hence, it is also natural to assume that it is not necessary to evaluate and assemble the global system at every iteration of Newton. This procedure is typically called the Modified Newton-Raphson or in the case of semi-positive definite projection, the Modified Projected Newton-Raphson scheme. However, as opposed to Projected Newton which is a tight approximation of the tangent (if not the tangent itself) Modified Newton further loses the quadratic convergence of Newton-Raphson and typically converges much slower. For this reason, all the examples presented in the next section are performed either with Newton or Projected-Newton. Nevertheless, a generalised Newton-Raphson scheme can be formulated as shown in Algorithm 2. Mixed finite element implementations with discontinuous local variables typically require a post-processing step to solve for the local variables at every iteration of Newton which is shown in Algorithm 2.

Numerically, straight-forward application of Newton-Raphson is not sufficient to guarantee convergence without blows-up even in the context of tangent stabilisation as a given loading increment might cause too big of a jump in residuals. As recently reported in[44], running Projected Newton over a large-scale database of over 10000 meshes of extremely challenging industrial complexity suggests that a fully automated minimisation procedure is possible to pass such datasets with 100% success rate if Projected Newton is coupled with a line search technique. Line search is a well-known technique to overcome blows-up and non-convergence of Newton. Line search also helps ensure that every step of the iteration results in a flip-free configuration[32,44]. A standard backtracking line search scheme is shown in Algorithm 3 although more sophisticated schemes that explicitly check for element inversion do exist[32].

6.2 | Equal singular values, perturbation and convergence

The only time that equal singular-values can create numerical issue is while computing the initial stiffness matrix specifically the first three eigen-values of the initial stiffness in 3D (and the first one in 2D) that involve $\lambda_j - \lambda_k$ as shown in Eqns. 32-34. However, as mentioned earlier, for displacement-based formulations this issue can be completely circumvented and not even the usually employed L'Hôpital rule is necessary[76,30]. This is because for isotropic materials isotropy dictates symmetry in principal

Algorithm 2 Generalised Newton-Raphson procedure

procedure MINIMISE
  Initialise $\mathbf{F}, \mathbf{R}, \mathbf{K}$
  repeat ▷ Increment loop
    $\Delta\mathbf{F} \leftarrow$ `LoadFactor` * `ComputeExternalForces()`
    Get current load increment $\mathbf{F} \leftarrow \mathbf{F} + \Delta\mathbf{F}$
    while $||\mathbf{R}|| >$ threshold **do** ▷ Newton-Raphson loop
      if `RequiresTangentEvaluation` **then** ▷ Newton or Modified Newton
        Assemble global tangent operator $\mathbf{K} \leftarrow \bigwedge\{\boldsymbol{K}_G\}$ ▷ Newton or Projected Newton
      end if
      Assemble residuals $\mathbf{R} \leftarrow \bigwedge\{\boldsymbol{R}_G\}$
      Add external loads $\mathbf{R} \leftarrow \mathbf{R} + \mathbf{F}$
      Solve linear system $\mathbf{K}\Delta\boldsymbol{x} = -\mathbf{R}$
      Post-process mixed discontinuous variables $\mathcal{A}, \mathcal{S}$
      Obtain line search parameter $\alpha \leftarrow \mathcal{W}(\boldsymbol{x} + \alpha\Delta\boldsymbol{x})$ ▷ Line search
      Update geometry $\boldsymbol{x} \leftarrow \boldsymbol{x} + \alpha\Delta\boldsymbol{x}$
    end while
  until `LoadFactor` $= 1$
end procedure

Algorithm 3 Line search procedure

procedure LINESEARCH($\Delta\boldsymbol{x}$)
  Assemble energy $\mathcal{W}_0 \leftarrow \mathcal{W}(\boldsymbol{x})$
  Assemble residuals $\mathbf{R}_0$ at $\boldsymbol{x}$
  Compute curvature $\mathcal{R}_0 \leftarrow \mathbf{R}_0 \cdot \Delta\boldsymbol{x}$
  Initialise $\alpha \leftarrow 1,\ \alpha_{\min} \leftarrow 10^{-16},\ \rho \leftarrow 0.5,\ c_1 \leftarrow 10^{-4},\ c_2 \leftarrow 0.95$
  repeat
    Assemble energy $\mathcal{W}_\alpha \leftarrow \mathcal{W}(\boldsymbol{x} + \alpha\Delta\boldsymbol{x})$
    Assemble residuals $\mathbf{R}_\alpha$ at $\boldsymbol{x} + \alpha\Delta\boldsymbol{x}$
    Compute curvature $\mathcal{R}_\alpha \leftarrow \mathbf{R}_\alpha \cdot \Delta\boldsymbol{x}$
    if $\mathcal{W}_\alpha \leq \mathcal{W}_0 + c_1\alpha\mathcal{R}_0$ **then** ▷ Sufficient decrease condition
      break
    else if $\mathcal{R}_\alpha \leq c_2\mathcal{R}_0$ **then** ▷ Curvature condition
      break
    else
      $\alpha \leftarrow \rho\alpha$
    end if
    $k \leftarrow k + 1$
  until $k \geq$ `numMaxIterations` or $\alpha < \alpha_{\min}$
end procedure

stretches and using the analytical formula directly from Eqns. 32-34 results in expressions that cancels out the denominator. More concretely, in our formulation we symbolically find the initial stiffness eigen-values from the script presented in Fig. B1.

For the case of mixed principal stretch formulation however, the singular-values are independent variables and if they happen to be numerically close (or equal resulting in division by zero) perturbation of the deformation gradient would be required. Certainly, L'Hôpital rule also does not apply in this context. In such cases, we follow the recommendation by[30] by perturbing (adding terms to) two diagonal entries of $\boldsymbol{F}$ by 2ϵ and ϵ. Unlike,[30] we do not use ϵ and $-\epsilon$ style perturbation since in extreme cases it can inadvertently result in an $\boldsymbol{F}$ with negative Jacobian $\boldsymbol{J}$. We use $\epsilon = 10^{-6}$.

An interesting observation further cemented by the notion of tangent stabilisation is given that, we perturb principal stretches merely to compute the *eigenvalues* of the initial stiffness, we can also discard these eigenvalues if principal stretches are numerically equal and if away from the origin ($\boldsymbol{F} \neq \boldsymbol{I}$). This further dampens the Newton method however, experiments show that equal singular-values when $\boldsymbol{F} \neq \boldsymbol{I}$ occur rarely in select quadrature points. In our setting, we first perturb $\boldsymbol{F}$ if and only if at least two singular-values are equal and then re-perform the SVD. Further, if Projected Newton is employed (as opposed to standard Newton) *and* the corresponding eigenvalues of the initial stiffness are still too big $> 10^6$ due to the denominator we simply discard them.

6.3 | On the choice of quadrature rules

Integration techniques have been extensive studied in the context of mixed finite elements [77,78]. Crucially, in the setting of tangent stabilised elasticity with mixed variables, it is important to guarantee that the integrated tangent operators over the elements are semi-positive definite. While the procedure outlined for semi-positive definite projection is an essential step towards this, care should be taken during numerical integration specially in the case of high order and mixed elements as not all quadrature rules necessarily have positive weights [79,80]. This can at times have adverse effect and can yield stiffness matrices which are numerically not semi-positive definite despite the projection. In this regard, one good choice is the reduced quadrature rules for general polyhedral finite elements presented in [81] which have guaranteed positive weights and in addition provide the minimum number of integration points for cost-effective implementation. Algorithm 1 shows the procedure for computing semi-positive definite tangents at a given quadrature point.

7 | NUMERICAL EXAMPLES

In this section we present a series of benchmark examples to verify the correctness and robustness of various finite element discretisations presented in the previous sections. Our focus, is primarily on high order displacement-based and the 7-field (5-field in 2D) mixed principal stretch based implementations of large strain elasticity in principal stretches. Separate tests are performed in 2 and 3 dimensions since the formulations based on principal stretch are different for planar and volumetric cases.

7.1 | Patch test

We start with a standard three dimensional patch test in order to assess the correctness of the computational implementation. The patch test is a necessary condition for the convergence of finite elements. It demands that an arbitrary patch of assembled elements is able to reproduce a constant state of stress and strain if subjected to boundary conditions consistent with constant straining. We follow the patch test problem presented in references [6,4] where two meshes of $2 \times 2 \times 2 \times 6 = 48$ tetrahedral elements are considered one comprising of regular tetrahedra (undistorted) Fig. 10(a) and one where the middle node is moved randomly within the the volume (distorted) Fig. 10(b). The compressible Mooney-Rivlin material W_{MR} presented in Eqn. 68 is used for this example with parameters $\mu_1 = 20k$Pa, $\mu_2 = 40k$Pa and $\kappa = 8000k$Pa.

A homogeneous deformation mapping is then defined through a stretch $\Delta L/L = 0.5$ applied in the vertical direction Fig. 10(c) and zero Dirichlet boundary conditions elsewhere on the boundary in other directions. The objective is to then demonstrate that the same solution is obtained for both meshes. We observe a homogenous distribution of deformation gradient and principal stretch ($\lambda_{\max} = \lambda_1 = 1.5$) and a Cauchy stress of $\sigma_{zz} = 4166.666k$Pa. Identical results (within machine accuracy) are obtained for both meshes for the displacement-based and mixed principal stretch formulations hence, passing the patch test.

7.2 | Cook's membrane

In this example the properties of the two proposed finite element formulations are analysed and compared namely, the displacement-based FEM formulated in principal stretches and the mixed principal stretch based FEM.

The Cook's membrane is a well-known benchmark for testing finite element formulations [82]. Similar to the original benchmark, a 2-dimensional model is set up but additionally a 3-dimensional model is also prepared. Three levels of mesh refinement (4×4, 8×8 and 16×16) on the geometry is considered with triangular and tetrahedral meshes, respectively as shown in Fig. 11. Refinements across the thickness are 2, 4 and 8 elements across the thickness for the volume mesh. The planar meshes have 32,

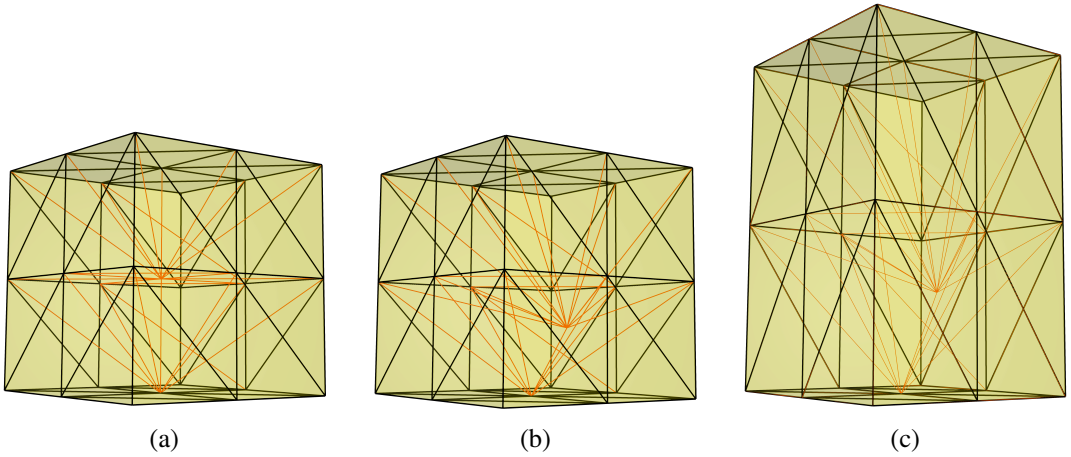

FIGURE 10 Three dimensional patch test. (a) view of undistorted mesh in the reference configuration. (b) view of distorted mesh in the reference configuration. (c) deformed geometry after stretching of $\Delta L/L = 0.5$.

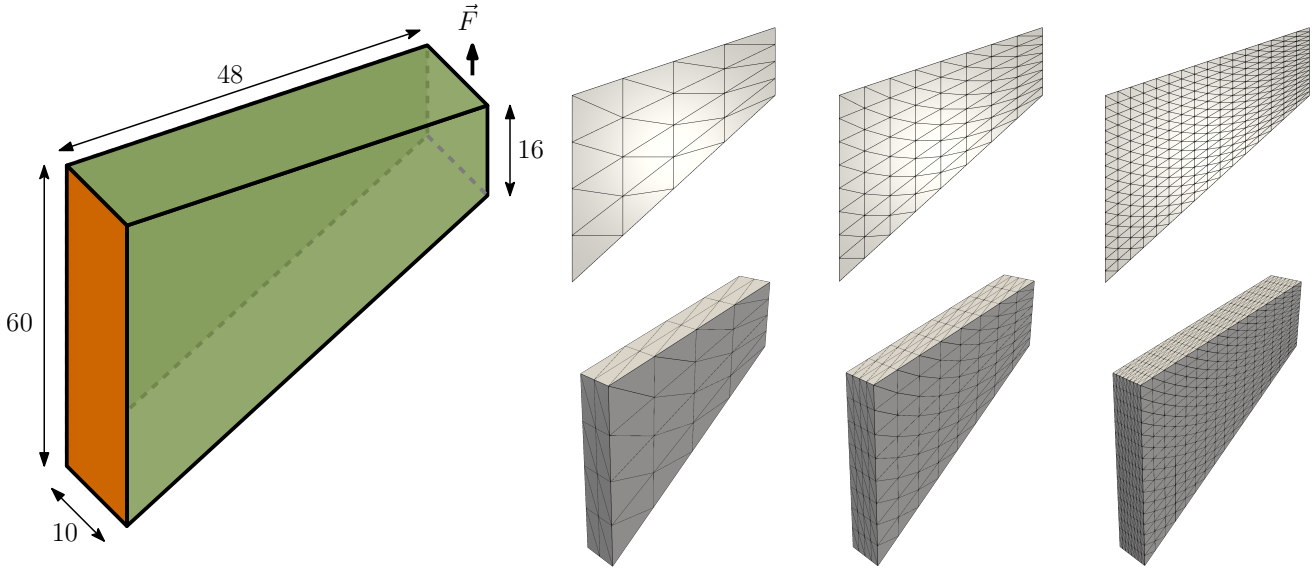

FIGURE 11 Cook type cantilever problem showing geometry of the problem and boundary conditions, where the dark orange plate is fixed and a parabolic upwards shear stress distribution is applied on its right end. The corresponding 2D and 3D meshes for the 3 levels of refinement are shown on the right.

128 and 512 elements, respectively and volume meshes have 142, 804 and 4605 elements, respectively. Customary to performing this benchmark and to test correctness of the proposed formulations we used a Poisson's ratio of $\nu = 0.45$ and Young's modulus of $E = 250$ using the Mooney-Rivlin material W_{MR} presented in Eqns. 68-69 and calibrated the material parameters accordingly. A shearing force of $F = 50$N was applied on the right wall as shown in Fig. 11. For this example, unless otherwise stated, we used the non-stabilised (standard) tangents for all formulations.

In Fig. 12, we first show the convergence of Newton-Raphson for both formulations. Quadratic convergence is attained for both formulations. To pinpoint the superiority of the mixed principal stretch formulations, we proceed by showing the contour plots of various quantities. The contour plot of vertical u_y displacement is shown in Fig. 13 for the coarsest mesh in both 2D and 3D cases. As expected displacement distribution is smooth for both formulations.

We further show the distribution of mixed/secondary (in the case displacement-based formulation post-processed) variables namely the principal stretch λ_1 for the 3D case in Fig. 16. To highlight the superior nature of mixed formulation over

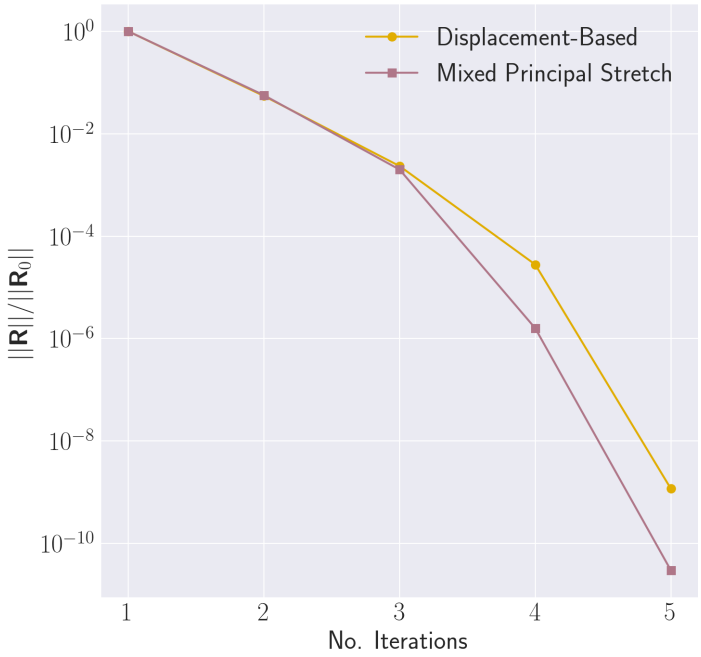

FIGURE 12 Quadratic convegrence of Newton-Raphson for P2 displacement-based and P2-P1 mixed principal stretch formulations.

displacement-based, in all cases the post-processed/secondary variables are not smoothed out over nodes. The discontinuous and rather patchy nature of principal stretch over the mesh is evident for displacement-based formulation.

To assess the correctness of the mixed implementation we further show the distribution of stress namely, principal first Piola-Kirchhoff stress Σ_{λ_2} and Cauchy stress σ_{xx} for 2D in Figs. 14-15 and von Mises for 3D in Fig. 17. For all three refinement levels a smooth distribution of stress is observed (certainly, barring the stress concentration region near the left fixity) for the mixed formulation with no evident signs of spurious oscillations whereas the displacement-based formulation once again exhibits a poorer behaviour. It is important to note that, for the case of the mixed principal stretch formulation the principal stretches and hence the stretch tensor ($\boldsymbol{U}$) are meant to be more accurate compared to the displacement-based formulation since they are primary variables but the rotation tensor ($\boldsymbol{R}$) is still computed from the geometry and hence, $\boldsymbol{F}$ in general may not show the same superior behaviour. The realisation however is that, most relevant quantities in structural/stress analysis can be described in terms of principal stresses. For instance, the von Mises stress can be computed from the principal components of the Cauchy stress tensor $\boldsymbol{\sigma}$. Noting the standard push-forward operation for obtaining $\boldsymbol{\sigma}$ and further using the SVD we have

$$\boldsymbol{\sigma} = J^{-1}\boldsymbol{P}\boldsymbol{F}^T = J^{-1}\hat{\boldsymbol{U}}\boldsymbol{\Lambda}_p\hat{\boldsymbol{V}}^T\hat{\boldsymbol{V}}\boldsymbol{\Lambda}\hat{\boldsymbol{U}}^T = J^{-1}\hat{\boldsymbol{U}}\boldsymbol{\Lambda}_p\boldsymbol{\Lambda}\hat{\boldsymbol{U}}^T. \tag{129}$$

and hence the principal components of $\boldsymbol{\sigma}$ in 3D are obtained as

$$\sigma_1 = (\lambda_2\lambda_3)^{-1}\Sigma_{\lambda_1}, \quad \sigma_2 = (\lambda_1\lambda_3)^{-1}\Sigma_{\lambda_2}, \quad \sigma_3 = (\lambda_1\lambda_2)^{-1}\Sigma_{\lambda_3}, \tag{130}$$

which only involves principal stretches and their conjugates which are all primary variables in our mixed finite element implementation. The von Mises stress is then computed as

$$\sigma_v = \frac{1}{\sqrt{2}}\sqrt{(\sigma_1-\sigma_2)^2+(\sigma_1-\sigma_3)^2+(\sigma_2-\sigma_3)^2}.$$

Analogous to $\boldsymbol{F}$ however, Cauchy stress $\boldsymbol{\sigma}$ itself involves both derivatives of geometry and principal stretches/conjugate stretches. However, as seen in Fig. 15 the Cauchy stress distribution is much smoother for the mixed formulation compared to the

		Displacement-based FEM			Mixed Principal Stretch FEM		
		Coarse	Medium	Fine	Coarse	Medium	Fine
Point A: [48, 60, 0]	u_x	-18.0897	-18.654	-18.9248	-18.0809	-18.6562	-18.9259
	u_y	18.4975	18.5486	18.5242	18.521	18.5535	18.5257
	λ_1	1.05006	1.06941	1.08156	1.16568	1.17428	1.18101
	λ_2	0.957398	0.948891	0.940271	0.880102	0.871776	0.866168
	σ_{xx}	-2.98121	3.1957	3.54528	4.62047	2.21644	0.652022
	σ_{xy}	0.765008	2.0772	2.25651	3.01326	4.72001	4.67003
	σ_{yy}	12.8962	23.4382	27.336	49.7846	50.1418	50.9005
Point B: [24, 37, 0]	u_x	-1.49532	-1.5709	-1.60289	-1.49831	-1.57207	-1.60362
	u_y	6.36149	6.47789	6.52421	6.36757	6.47977	6.52495
	λ_1	1.10307	1.10707	1.10949	1.10714	1.11059	1.11143
	λ_2	0.956301	0.929619	0.918239	0.911696	0.908994	0.908097
	σ_{xx}	37.3827	14.0868	4.84931	-4.84169	-4.30294	-4.04916
	σ_{xy}	6.42152	8.83305	10.1938	8.86428	10.1757	10.9095
	σ_{yy}	58.4818	38.6709	30.5633	24.2553	24.0265	23.4736

TABLE 1 Comparison of displacements and Cauchy stress components at multiple points for planar Cooks membrane problem for P2 displacement-based and P2-P1 mixed principal stretch formulations. The variation of stresses is sparse for displacement-based FEM but in a tighter range for mixed principal stretch FEM.

displacement-based formulation. Additionally, we compare with other popular high order elements namely Q2 hexahedral elements and show Cauchy stress $\boldsymbol{\sigma}$ in Fig. 18. We can observe that, for the same refinement level P2-P1 mixed formulation has indeed a more smoother distribution of stress, although the results of Q2 elements is closer to P2-P1 mixed elements compared to P2 elements.

Finally, to quantify the results, we highlight and compare convergence of displacements (u_x, u_y, u_z), principal stretches (λ_1, λ_2, λ_3) and all components of Cauchy stress σ_{ij} at multiple points in the geometry in Table 1 for 2D and in Table 2 for 3D case. The tabulated values show the oscillatory nature of stresses for the displacement-based formulation whereas the stresses for the mixed formulation seem in a more tighter range.

7.3 | Compression of a square plate

The goal of this example is to study the effect of tangent stabilisation and show its performance characteristics.

Generally, it is not considered a good practice to remove the negative eigen-modes from the initial stiffness matrix as it can change the deformation profile drastically. Moreover, since, most hyperelastic energies used in engineering simulation are non-convex, initial stiffness stabilisation essentially implies favouring solvability and convergence over finding the global minimum since the results obtained with stabilised/modified initial stiffness could very well correspond to a local minimum. However, tangent stabilisation can be exercised cautiously based on the underlying energy used. The goal here is certainly not speed but rather automation of nonlinear simulation workflow although in complex cases projected Newton with tangent stabilisation can result in fewer total iteration than standard Newton as it does not require a high number of load increments.

Inspired by [30], in this section, we conduct a series of studies by determining the minimum number of load increments required by the standard Newton-Raphson technique and its counterpart tangent stabilised Projected Newton without relying on line search or load control techniques. We report convergence patterns, total number of iterations across all load increments and in general the success/failure (convergence/non-convergence) of each method. This study is designed to shed light on the performance of Projected Newton algorithm which has not been studied in the engineering simulation community although such comparisons appear in computer graphics literature [18,20,44].

For the purpose of this study, we use the nearly incompressible Mooney-Rivlin model described in Eqns. 73-74 with shearing modulus of $\mu = 1$ and a Poisson's ratio of $\nu = 0.495$. More specfically, we consider $\mu_2 = 0$ and $\eta = 1$. Polyconvexity of the energy under such setting is well-known [50,62].

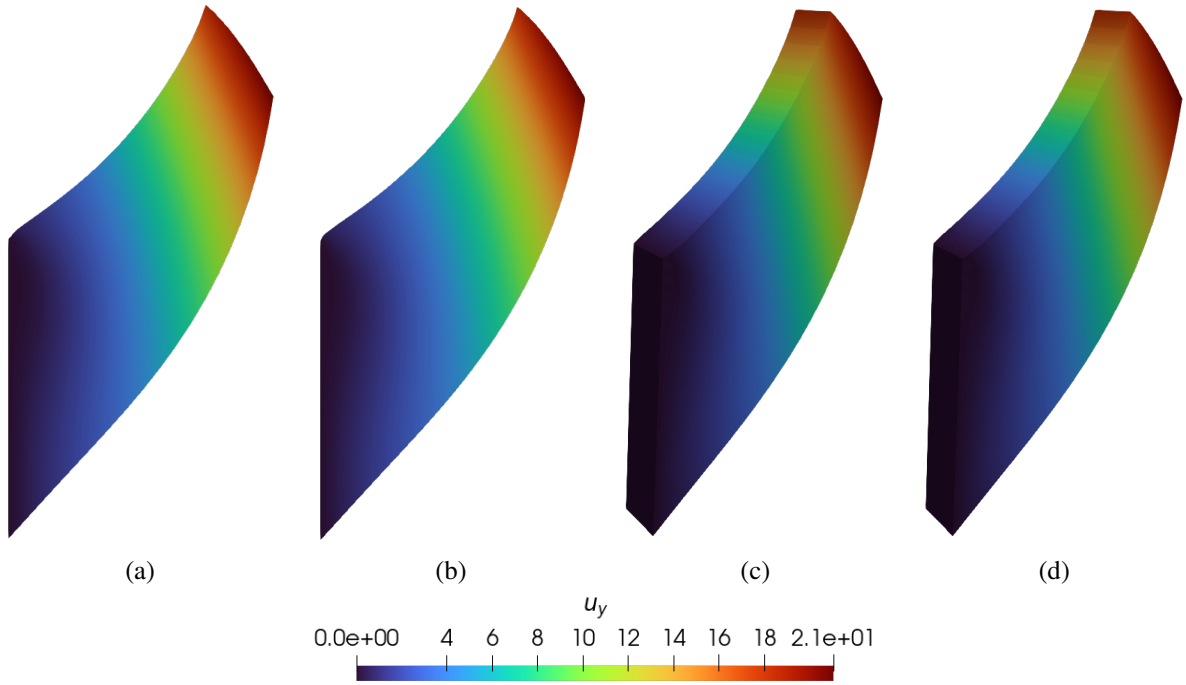

FIGURE 13 Contour plot of vertical displacement u_y for the coarsest mesh in 2-dimensions (a,b) and 3-dimensions (c,d). Plots (a) and (c) are for P2 displacement-based formulation and plots (b) and (d) for P2-P1 mixed principal stretch formulation. Displacement distribution is smooth for both formulations as expected.

We first consider a square plate of $50 \times 50mm^2$ as shown in Fig. 19 with four levels of mesh refinement to gain additional insight into any differences in behaviour of Newton-Raphson (NR) and Projected-Newton (PN) techniques. The study pertains compressing half of the plate with an imposed downward displacement of $25mm$. For now, we limit our study to displacement-based formulation as the same findings carry over naturally to mixed formulations.

Fig. 20 shows the convergence pattern of NR and PN for the coarsest mesh ($6 \times 6 \times 2$) across all load increments. We fix the residual tolerance to 10^{-3} which is rather tight for engineering accuracy and report normalised residual $||\mathbf{R}||/||\mathbf{R}_0||$ for clearer comparison and to avoid irregular jumps in the plots. NR required at least 20 equal load increments to successfully converge without any line search or load control techniques being employed while PN achieved convergence in only 2 equal load increments albeit with significantly different convergence pattern. We avoided employing automatic load controls and line search in all cases to highlight the true difference between NR and PN, although PN with line search converges even with a single load increment. The total number of iterations for the coarsest mesh was slightly higher for PN compared to NR ((88 vs 76).

Figs. 21, 22 and 23 show the convergence for the remaining refinement levels. As the mesh resolution increases both NR and PN required further loading increments. However, PN's total number of iterations increased significantly with mesh refinement but with successful convergence. On the other hand, for the finest refinement level, NR failed to converge regardless of the load increments. We experimented increasing the number of equal load increments all the way to 1000 and verified that all intermediate number of load increments also resulted in non-convergence. This a classic case where due to compression the area next to the loading zone experiences buckling as shown in Fig. 25. It is clear that, PN successfully resolves this deformation scenario.

The relative difference in the final deformed geometry between PN and NR is shown in Table 3 which is negligible. However, as observed, the superlinear convergence of PN results from roughly the same to 3.4 times more iterations. It should be noted that the increased number of iterations for PN is due to the load being applied in a much more rapid fashion than NR. In Fig. 24 we increase the number of increments for PN to 20 and observe that in the first few increments (potentially linear regime) PN maintains the performance of NR. In general, the performance is hugely subsided by the fact that enables using fast Cholesky solvers. In Fig. 29 we compare the performance of PN with NR in terms of total simulation time and find that while it is still

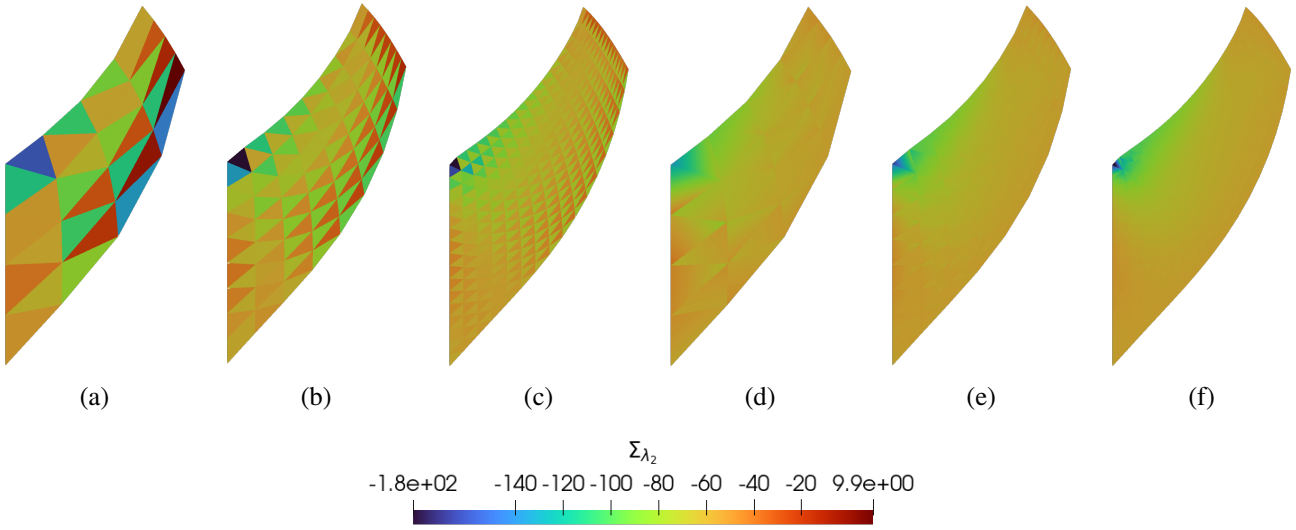

FIGURE 14 Contour plot of first Piola-Kirchhoff principal stress Σ_{λ_2} for planar Cooks membrane problem for three refinement levels using P2 displacement-based formulation (a,b,c) and P2-P1 mixed principal stretch formulation (d,e,f). For both cases, distribution profiles are not smoothed on purpose to showcase the discontinuous nature of secondary variables.

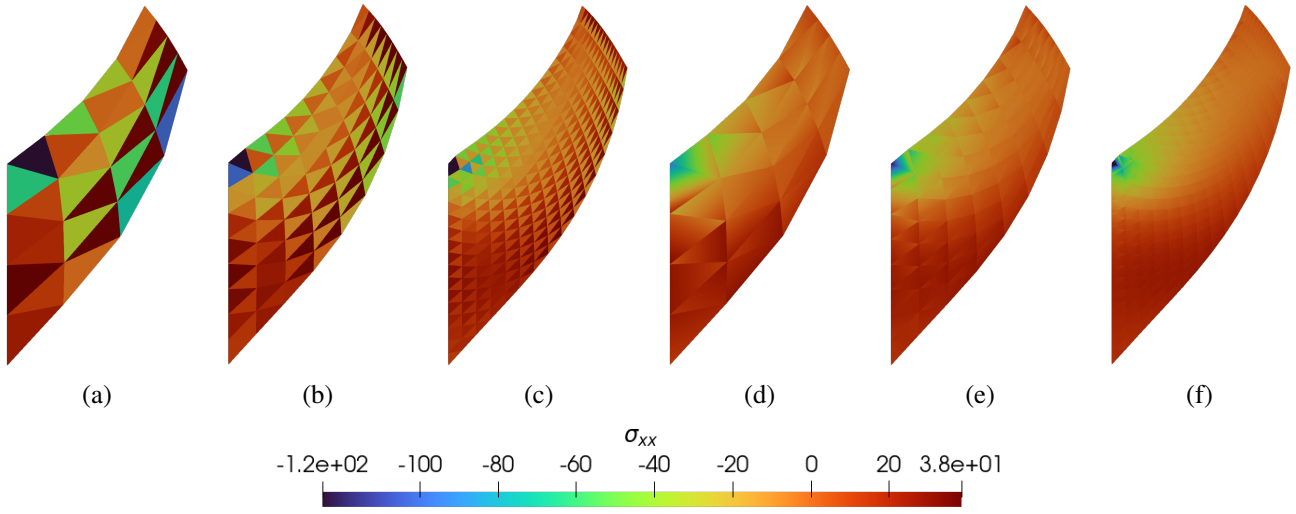

FIGURE 15 Contour plot of Cauchy stress σ_{xx} for planar Cooks membrane problem for three refinement levels using P2 displacement-based formulation (a,b,c) and P2-P1 mixed principal stretch formulation (d,e,f). The introduction of 2 Lagrange multipliers namely $\Sigma_{\lambda_1}, \Sigma_{\lambda_2}$ is enough for our mixed formulation to produce a smoother variation of stress. Distribution profiles are not smoothed on purpose.

slower than NR, the slow-down is not as high ($\sim 2.5\times$). Moreover, convergence of PN can also be accelerated with line search techniques that smartly choose the increment factor[12].

7.4 | Inhomogeneous tension test

The goal of this example is

1. Show the impact of tangent stabilisation in the context of mixed formulations.

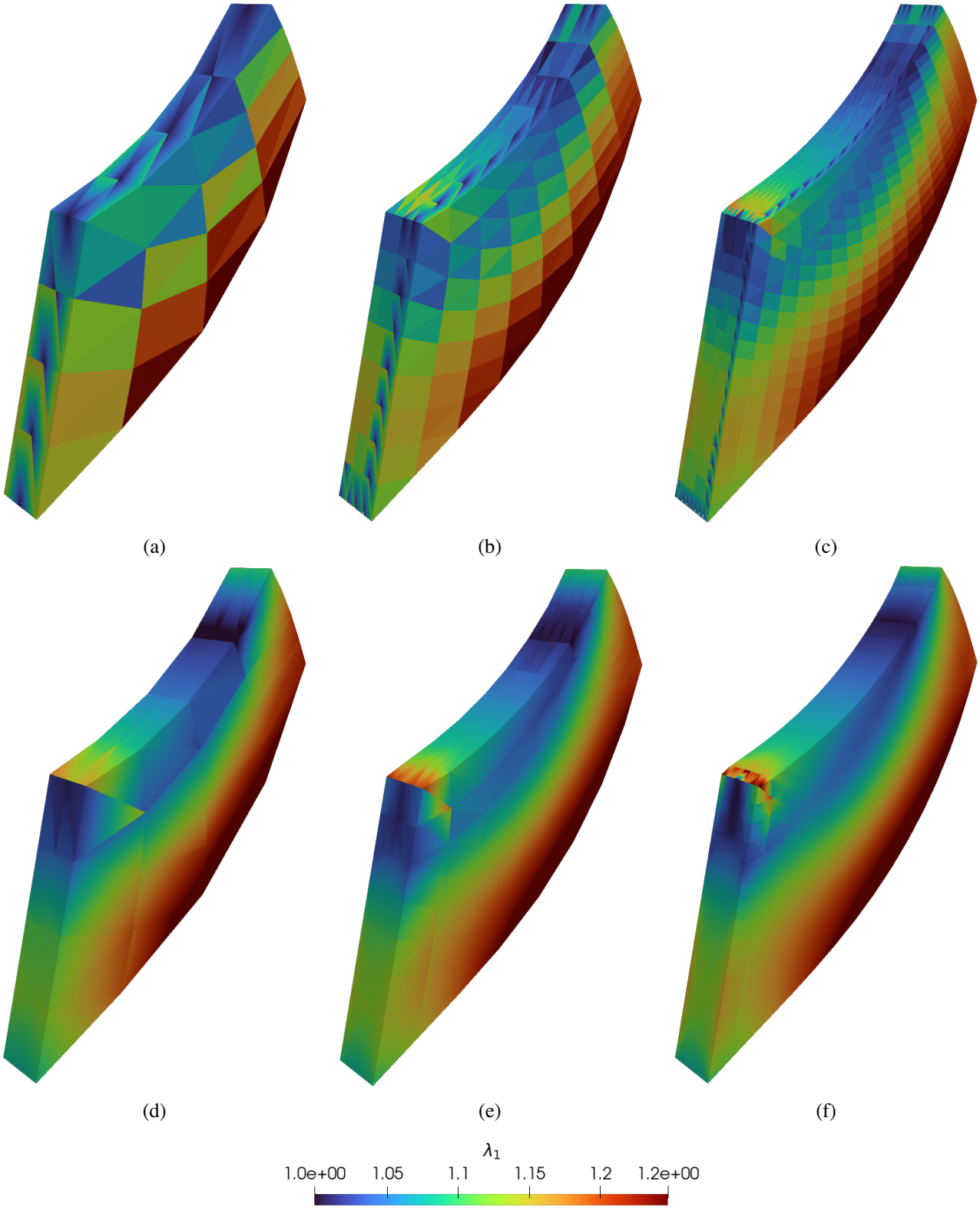

FIGURE 16 Contour plot of principal stretch λ_1 for 3-dimensional Cooks membrane problem for three refinement levels using P2 displacement-based formulation (a,b,c) and P2-P1 mixed principal stretch formulation (d,e,f). For both cases, distribution profiles are not smoothed on purpose to showcase the discontinuous nature of secondary variables.

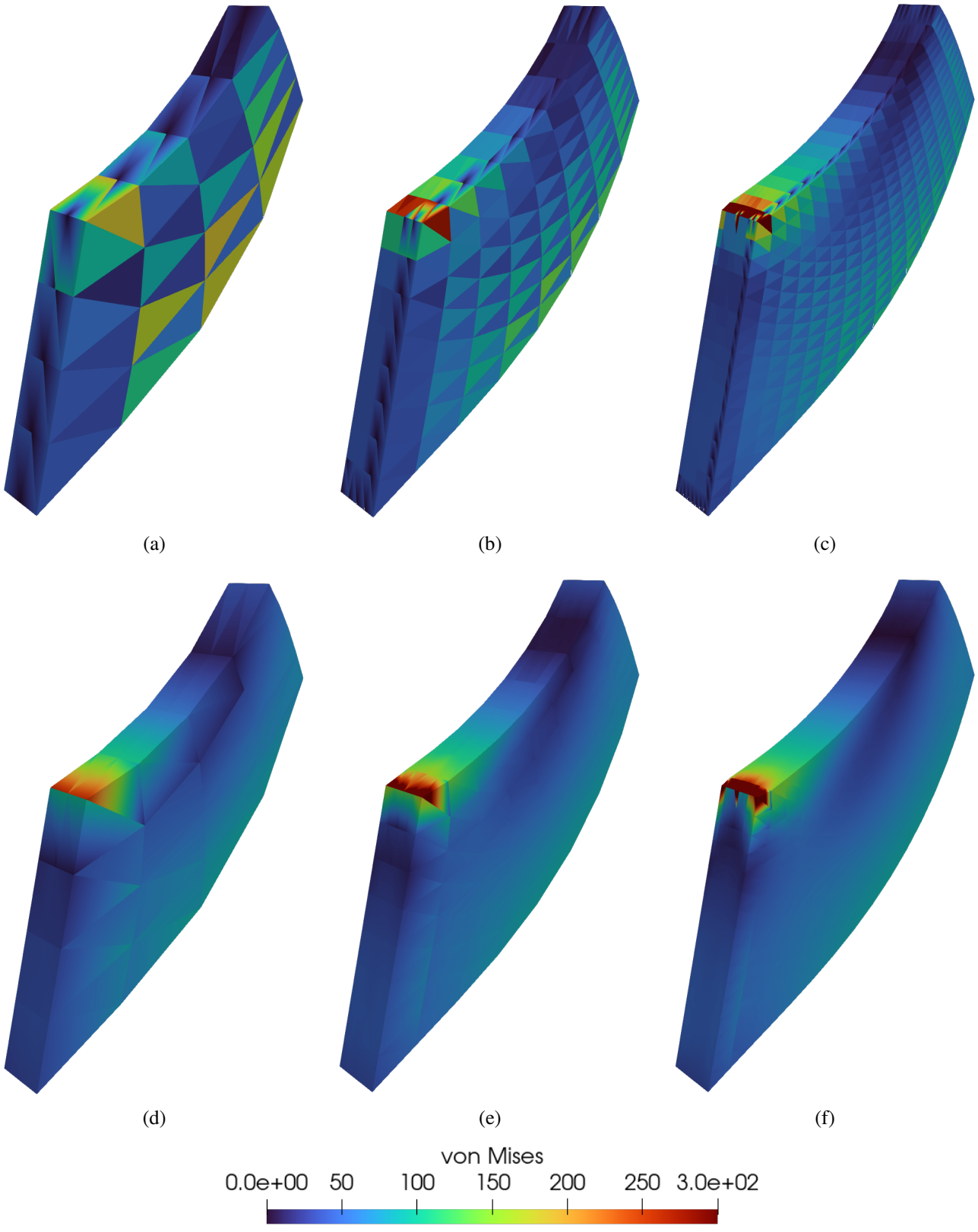

FIGURE 17 Contour plot of von Mises stresses for 3-dimensional Cooks membrane problem for three refinement levels using P2 displacement-based formulation (a,b,c) and P2-P1 mixed principal stretch formulation (d,e,f). For the case of mixed formulation, the von Mises stress can be computed using mixed variables only which highlights the advantage of the proposed mixed principal stretch FEM. Distribution profiles are not smoothed.

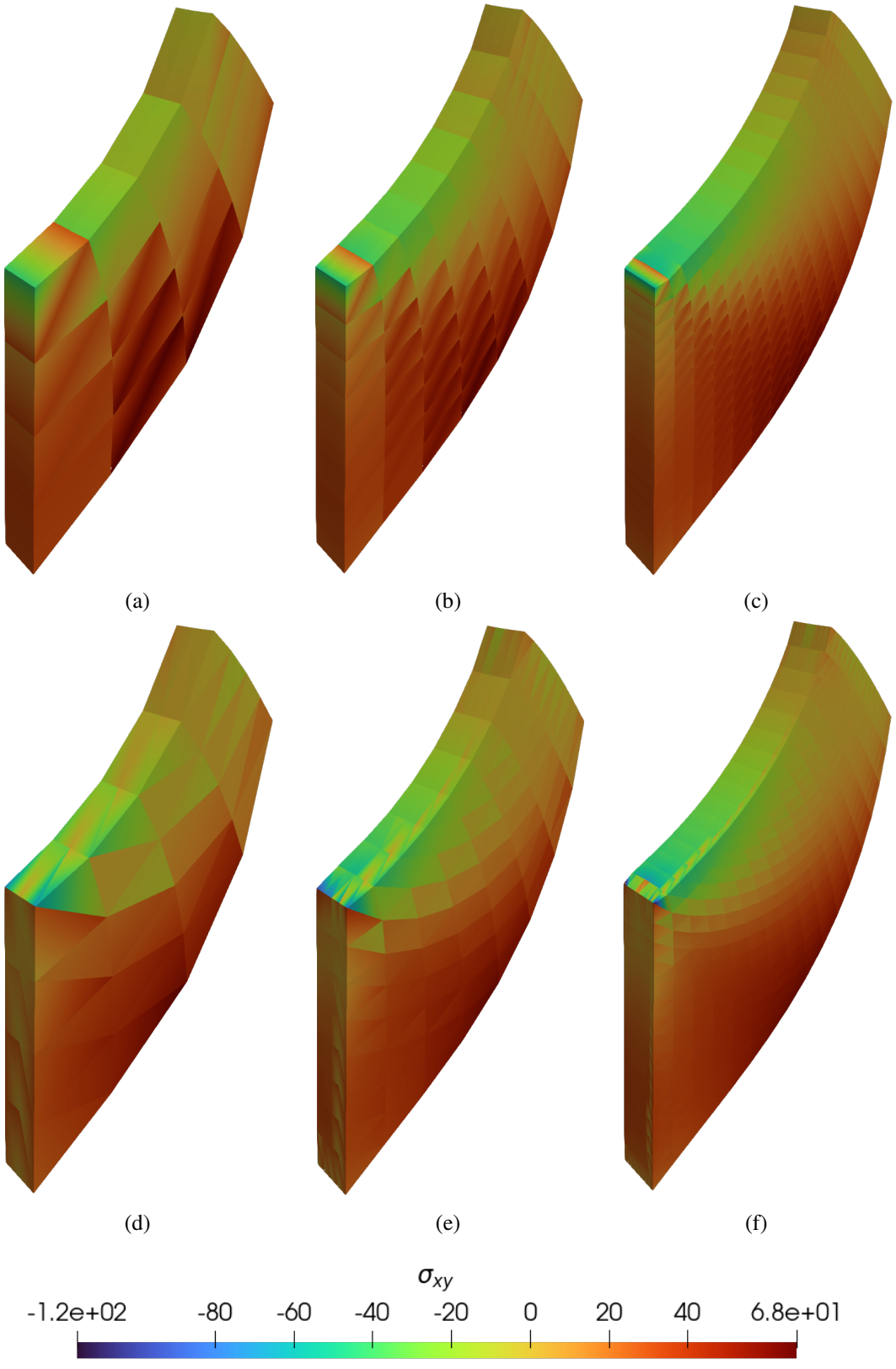

FIGURE 18 Further comparison of P2-P1 mixed formulation (d,e,f) **with Q2 (parabolic hexahedral) elements** (a,b,c) for three refinement levels for Cauchy stress σ_{xy}. Note that, Cauchy stress $\boldsymbol{\sigma} = J^{-1}\hat{\boldsymbol{U}}\boldsymbol{\Lambda}_p\boldsymbol{\Lambda}\hat{\boldsymbol{U}}^T$ involves both derivatives of geometry (post-processed) and mixed variables. For a fixed refinement level, P2-P1 mixed formulation shows a smoother profile compared to Q2 elements. Distribution profiles are not smoothed.

		Displacement-based FEM			Mixed Principal Stretch FEM		
		Coarse	Medium	Fine	Coarse	Medium	Fine
Point A: [48, 60, 0]	u_x	-21.23	-21.5418	-21.6486	-21.2607	-21.5567	-21.6519
	u_y	19.8214	19.9173	19.9401	19.8326	19.9211	19.9417
	u_z	-0.234599	-0.209553	-0.195644	-0.243519	-0.208968	-0.194938
	λ_1	1.08266	1.0527	1.06679	1.06989	1.09438	1.0988
	λ_2	1.0361	1.00815	0.999095	1.07142	0.973984	0.970233
	λ_3	0.864915	0.940944	0.94379	0.839045	0.956605	0.956059
	σ_{xx}	-37.3125	2.46007	5.28387	-42.0459	9.95598	7.93569
	σ_{xy}	-29.9033	4.25165	5.91717	-40.5827	10.8578	10.7548
	σ_{xz}	-3.33556	-3.50633	-3.4009	1.07802	-1.23533	-1.27275
	σ_{yy}	-38.5959	16.3511	26.6437	43.65	43.8297	45.7656
	σ_{yz}	4.56012	-0.398905	-0.919542	0.779728	-1.26402	-1.75086
	σ_{zz}	5.47231	-20.3437	-13.5446	-2.80004	1.12104	0.651516
Point B: [24, 37, 0]	u_x	-1.86424	-1.97141	-2.00875	-1.86823	-1.97512	-2.01018
	u_y	7.14304	7.26162	7.29798	7.1524	7.2667	7.29979
	u_z	-0.13473	-0.132667	-0.120607	-0.138432	-0.131928	-0.1204
	λ_1	1.13136	1.16329	1.1233	1.1156	1.12127	1.1218
	λ_2	0.965105	0.954615	0.975788	0.977205	0.974364	0.973872
	λ_3	0.877189	0.876938	0.907411	0.920512	0.92594	0.925987
	σ_{xx}	-70.279	-48.3941	-25.7772	-19.4195	-5.78394	-6.94213
	σ_{xy}	16.9076	30.9788	24.101	12.3959	20.8654	21.6144
	σ_{xz}	-4.25	-6.48631	-2.34568	-2.46309	-3.80133	-1.52709
	σ_{yy}	14.3856	31.6463	32.5247	43.1635	48.2317	45.3826
	σ_{yz}	1.8213	3.05463	1.56433	1.21919	1.88441	1.25944
	σ_{zz}	-45.7941	-38.2061	-12.8017	-5.22654	-0.639664	0.0217264

TABLE 2 Comparison of convergence of displacements and stress components at multiple points for volumetric Cooks membrane problem for P2 displacement-based and P2-P1 mixed principal stretch formulations. The variation of stresses is sparse for displacement-based FEM but in a tighter range for mixed principal stretch FEM.

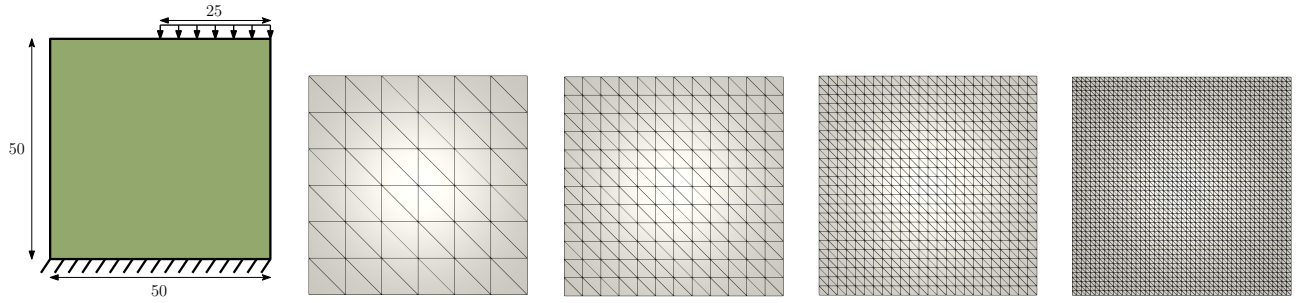

(a) (b) (c) (d) (e)

FIGURE 19 Geometry, boundary conditions and different mesh refinements considered for the square plate.

2. Show the performance mixed principal formulation in the nearly incompressible regime.

For this example, we use the inhomogeneous tension test[30] on a unit cube of volume 1unit^3 to assess the performance of tangent stabilisation in 3D and in the context of mixed formulations. We further use the incompressible Mooney-Rivlin model but since our formulation is not directly for incompressibility we consider a Poisson's ratio $\nu = 0.499$ to test the performance mixed principal stretch formulation in the nearly incompressible regime. A stretching force of $F = 3$unit is applied on one face and the opposite face is fixed. Three refinement levels were used with 694, 2992, 23936 parabolic tetrahedral elements, respectively 27.

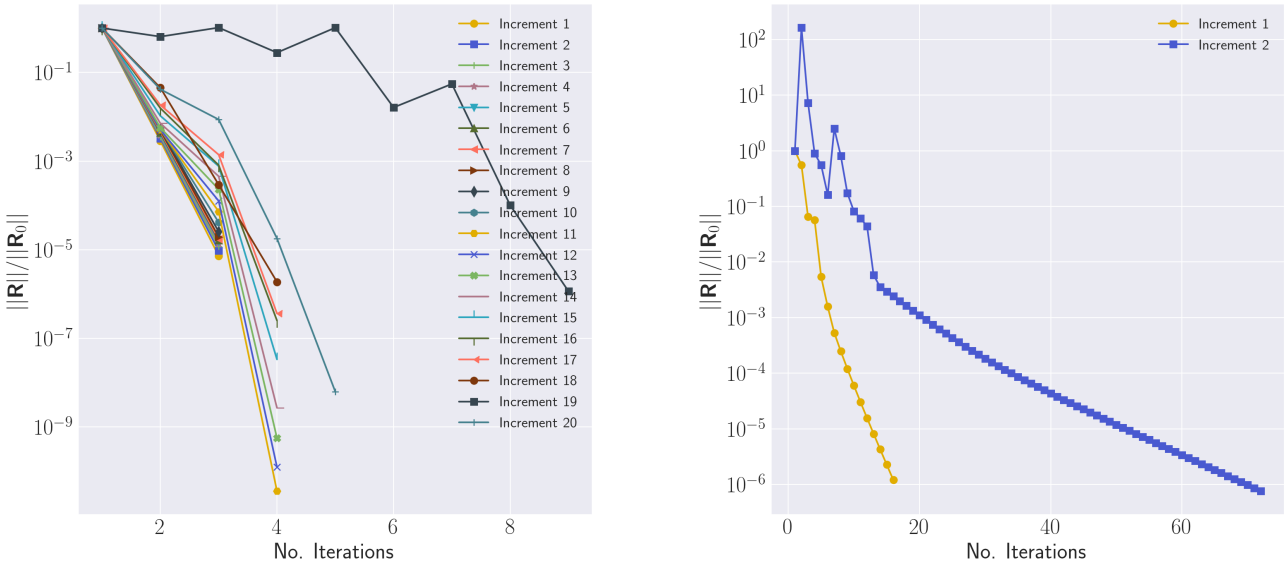

FIGURE 20 Convergence pattern of standard Newton-Raphson (NR) vs Projected Newton (PN) (with constitutive tangent and initial stiffness stabilisation) for square plate mesh ($6 \times 6 \times 2$) from Fig. 19 for a fixed residual tolerance of 10^{-3} across all load increments. We report normalised residual $||\mathbf{R}||/||\mathbf{R}_0||$ for clearer comparison and to avoid irregular jumps in the plots. No line search or load control techniques is activated in either case to highlight the true difference between NR and PN. NR required a minimum of 20 increments to achieve convergence and PN 2 increments. Across all increments, NR convergence is quadratic while PN is superlinear. Total number of iterations - NR: 76, PN: 88.

Method / Resolution	$6 \times 6 \times 2$	$12 \times 12 \times 2$	$24 \times 24 \times 2$	$48 \times 48 \times 2$
Newton Raphson (NR)	20 (76)	20 (80)	22 (90)	✗
Projected Newton (PN)	2 (88)	4 (172)	6 (306)	7 (637)
$\|\|\boldsymbol{x}_{PN} - \boldsymbol{x}_{NR}\|\|/\|\|\boldsymbol{x}_{NR}\|\|$	2.061e-06	9.498e-07	1.506e-06	-

TABLE 3 Comparison of NR and PN in terms of number of increments (total number of iterations), and the L^2 norm of difference in the final deformed configuration. A fixed residual tolerance of 10^{-3} was used for both NR and PN. PN required from roughly the same to 3.4 times more iterations but succeeded in all cases including the buckling case. The increased number of iterations however is subsided by the ability to switch from LU to Cholesky-based solver. No load control techniques were employed.

In Fig. 27 we compare the performance of NR and PN with mixed formulation under a nearly incompressible regime. While the system does not experience buckling in this case the initial stiffness matrix still goes indefinite as can be seen in Fig. 6. The convergence of PN in this case is very similar to PN as shown in Fig. 26 differing at most by one extra iteration. In Fig. 29 we compare the performance of PN with NR in terms of total simulation time and find that PN is actually marginally faster in this case (by about 15-20%) due to the switch from LU to Cholesky solver.

A natural question then arises: how is our analytically constructed tangents different than numerically decomposing the tangent operators using standard eigenvalue decomposition techniques. This question is answered in Fig. 30 where we show that in our settings, tangent operators are by design constructed in an already “eigen-decomposed" form whereas numerical eigen-decomposition ensues additional cost. If this decomposition is done in the spirit of our analytical construction that is, on per-quadrature bases (using a dense eigen solver) than the computational cost is increased by at least a factor of 2 in 2D and a factor of 4 in 3D, consistently. If the eigen decomposition is performed on the global sparse linear system then the computational cost increases cubically and in 3D it results in over an order of magnitude difference in total simulation time. As a matter of

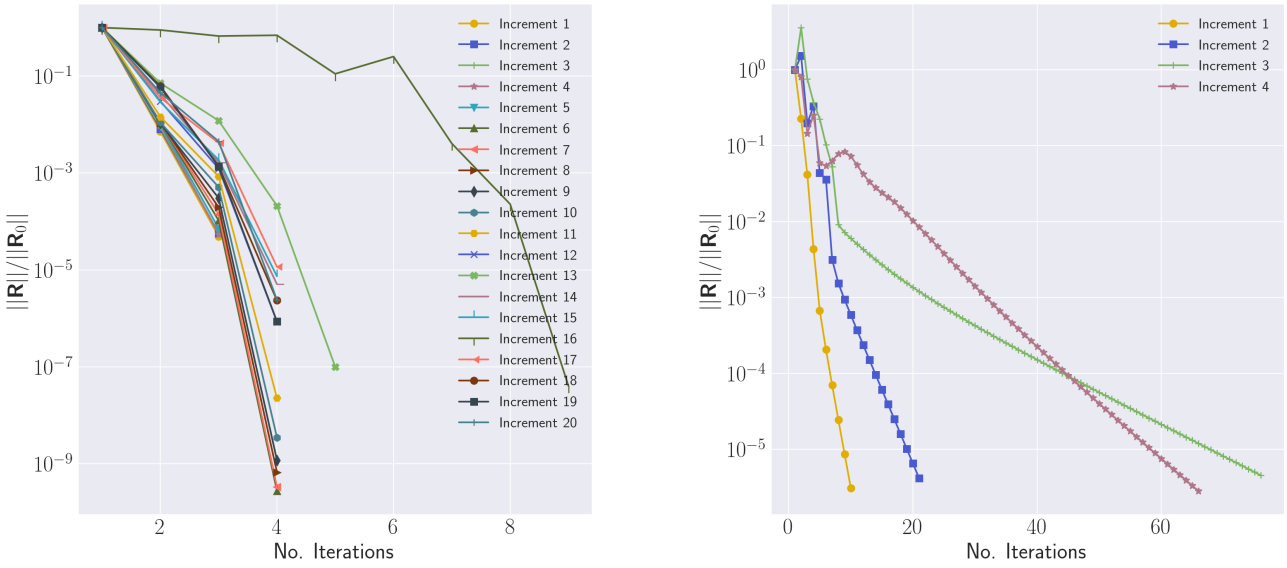

FIGURE 21 Convergence pattern of standard NR vs PN for square plate mesh ($12 \times 12 \times 2$) from Fig. 19 for a fixed residual tolerance of 10^{-3} across all load increments. We track normalised residual $||\mathbf{R}||/||\mathbf{R}_0||$. No line search or load control techniques is activated. NR required a minimum of 20 increments to achieve convergence and PN 4 increments. Total number of iterations - NR: 80, PN: 172.

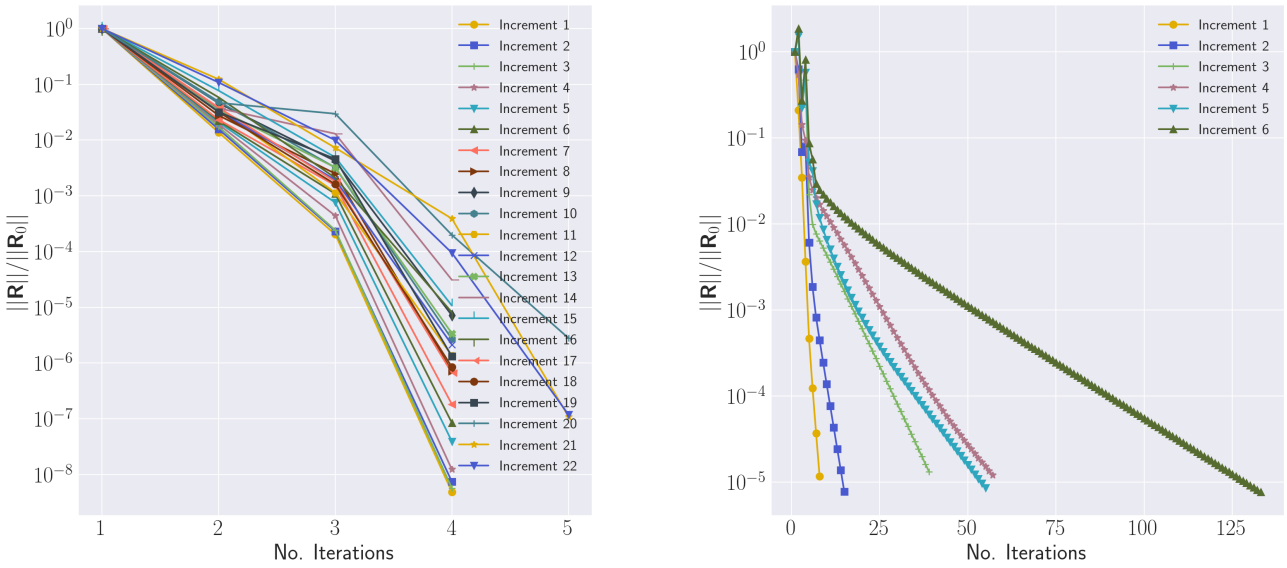

FIGURE 22 Convergence pattern of standard NR vs PN for square plate mesh ($12 \times 12 \times 2$) from Fig. 19 for a fixed residual tolerance of 10^{-3} across all load increments. We track normalised residual $||\mathbf{R}||/||\mathbf{R}_0||$. No line search or load control techniques is activated. NR required a minimum of 20 increments to achieve convergence and PN 6 increments. Total number of iterations - NR: 90, PN: 306.

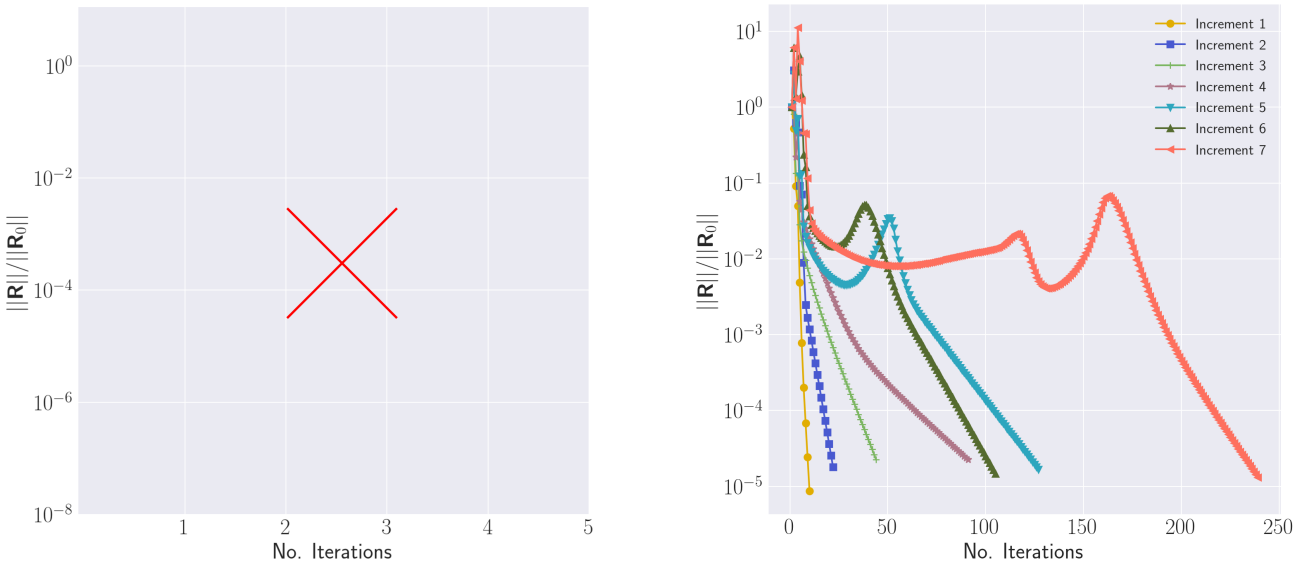

(a) (b)

FIGURE 23 Convergence pattern of standard NR vs PN for square plate mesh ($48 \times 48 \times 2$) from Fig. 19 for a fixed residual tolerance of 10^{-3} across all load increments. We track normalised residual $||\mathbf{R}||/||\mathbf{R}_0||$. No line search or load control techniques is activated. **NR failed regardless of load increments** (we experimented till 1000 increments), and PN required 7 increments. Total number of iterations - NR: ✗ PN: 637.

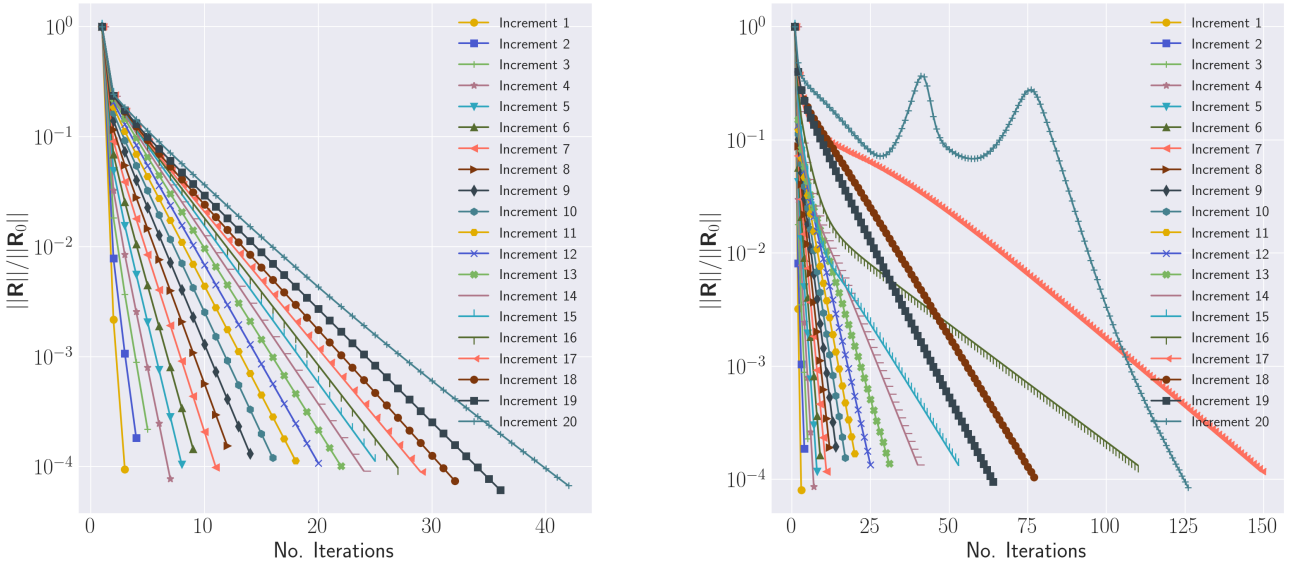

(a) (b)

FIGURE 24 Effect of number of load increments on convergence of PN: using the same load increments as NR for PN generally improves per increment convergence of PN, although such high number of load increments are unnecessary for PN. In the first few increments (potentially linear regime) PN maintains the quadratic convergence of NR. Plots show convergence for square plate problem with the two finest refinement levels.

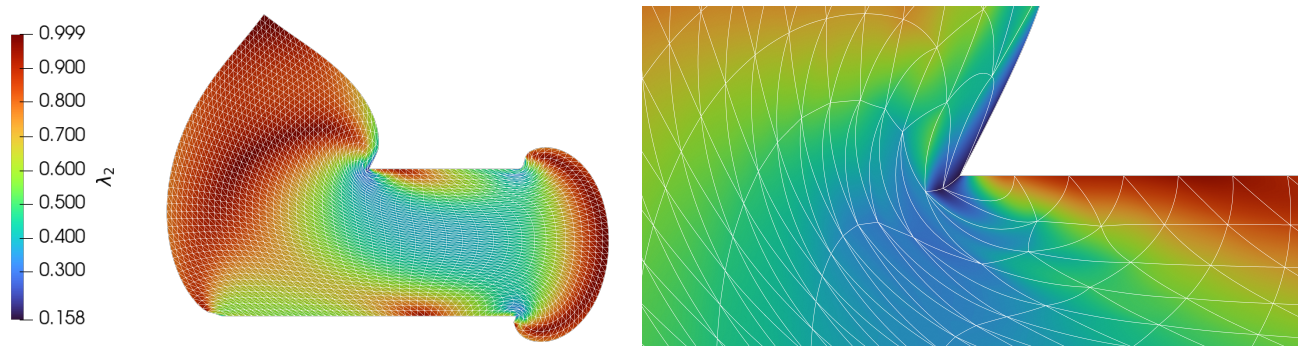

(a) (b)

FIGURE 25 Final deformed configuration for square plate with the finest mesh ($48 \times 48 \times 2$) solved using PN. NR fails for this resolution due to buckling as shown in the zoomed plot (b). Smoothed distribution of λ_2 obtained with P2 displacement-based formulation.

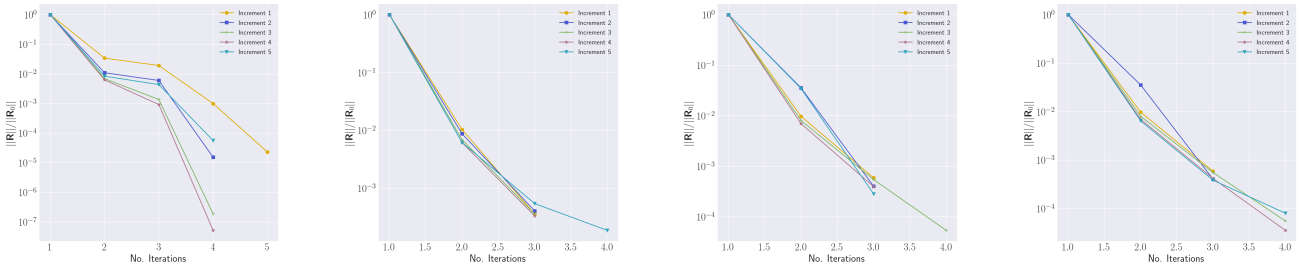

(a) (b) (c) (d)

FIGURE 26 Tangent stabilisation in the context mixed principal stretch formulation: Convergence of NR (a,c) vs PN (b,d) for inhomogeneous tension test using both displacement-based (a,b) and mixed principal stretch formulations (c,d) (7-field formulation) using 5 increments and a fixed residual 10^{-3} without any automatic control technique. If the system does not experience buckling, PN can maintain the performance of NR.

fact, computing the eigen-decomposition of the global linear system becomes forbiddingly time consuming for meshes used in practice. For this study, we used the dense eigen-decomposition `Eigen::SelfAdjointSolver` from the Eigen math library for per-quadrature projection and `SymEigsShiftSolver` from Spectra library. Also note that, numerical eigen-decomposition algorithms are iterative and tolerance-bound. Our experiments show that even with a tight tolerance $< 10^{-14}$ they often further impact the convergence of Newton. In that, numerically Projected Newton requires more Newton iterations compared to our analytically Projected Newton; see[44] for a detailed investigation.

Fig. 27 shows the distribution of deformation for the finest refinement level. It is interesting to observe that, the mixed principal stretch formulation produces a smooth stretch distribution (and hence a smooth Jacobian $J = \lambda_1\lambda_2\lambda_3$ distribution, although we did not show this as $J \approx 1$ and the distribution seemed less revealing) in nearly incompressible regime. The displacement-based formulation on the other hand, produces an overtly patchy distribution even after smoothing the processed Jacobian.

Noting this, we stress test the mixed formulation further in Fig. 28 by pushing the Poisson's ratio all the way to $\nu = 0.499999$ and show that the distribution of all three principal stretches are smooth at the limit of incompressibility.

7.5 | Buckling of a simple 2-dimensional column

We next show an example of simple buckling case that highlights a particular difference between PN and NR in practice. As shown in Fig. 31 a column is pressed vertically but with different structured and unstructured parabolic meshes. Canonical

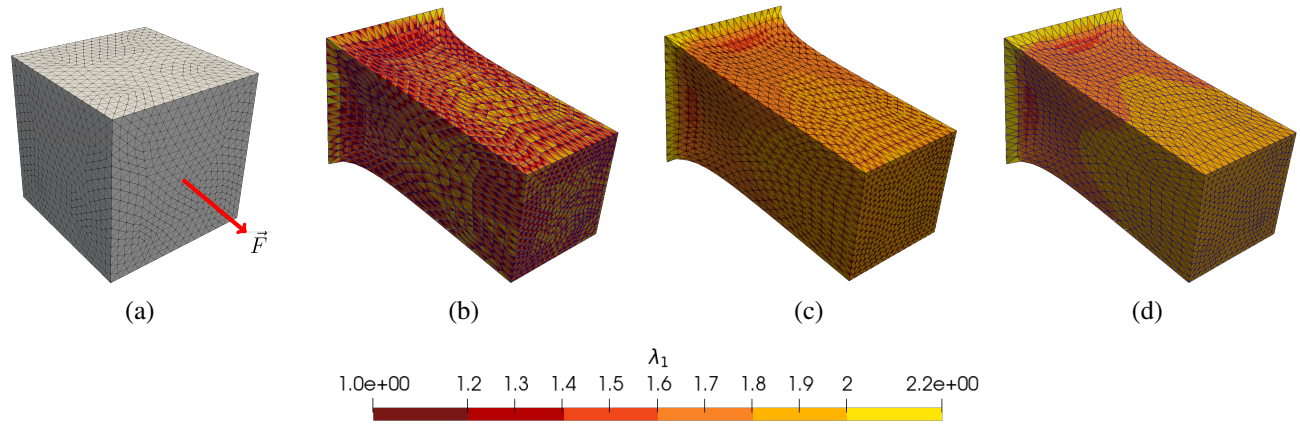

FIGURE 27 Mixed principal stretch formulation in nearly incompressible regime *with* tangent stabilisation: Initial and deformed configurations for the inhomogeneous tension test obtained with displacement-based (b, c) and mixed principal stretch (d) formulations using PN showing distribution of stretch λ_1 for nearly incompressible Mooney-Rivlin model with $\nu = 0.499$. For displacement-based formulation both non-smooth (b) and smoothed (c) stretch profiles are now shown indicating its extremely poor performance in the nearly incompressible regime. On the other hand, plot (d) confirms that PN (i.e. tangent stabilisation) has no impact on the accuracy of mixed variables with mixed principal stretch formulation.

benchmark parameters and dimensions are used for this example: Dimension $2 \times 20\text{unit}^2$, bottom fixed with an imposed displacement of 10unit downward; nearly incompressible Mooney-Rivlin model with $\alpha = 1$ and $\nu = 0.495$. For structured quad meshes NR does not produce the buckled profile using either displacement Q2 or mixed formulation Q2-Q1, Fig. 31(a,b). With a parabolic triangular meshes however, NR produces two different profiles depending on the displacement and mixed formulation Fig. 31(c,d). Due to enhanced stability, PN however, produces the same deformation profile regardless of the mesh and formulation employed Fig. 31(e,f,g,h).

Notice that, we have also employed the Q2-Q1 element using the mixed principal stretch formulation for this example which successfully worked for this problem. However, we leave a more thorough investigation of this element to future work.

7.6 | Pinch and pull-out of cylindrical shell

Pinch and pullout analysis of cylindrical shells is routinely performed as popular nonlinear buckling benchmarks for shell structures[83]. The setup of the problem is in Fig. 32 with thickness $h = 1mm$, radius $R = 100mm$, length $L = 200mm$, Young's modulus $E = 3 \times 10^4 N/mm^2$, and Poisson's ratio $\nu = 0.3$. In line with the standard benchmarks which use a NeoHookean model, the compressible Mooney-Rivlin model is employed in our setting by considering a zero cofactor-related material parameter i.e. $\mu_2 = 0$. While it is customary to consider 1/4th or 1/8th of the geometric model due to symmetry, the entire geometry is meshed in our case with 7100 parabolic tetrahedral elements, Fig. 32. The first study pertains applying a pinching force at the tip of the cylinder and tracking the response, Fig. 32(a). As can be seen from Fig. 33 PN with a single load increment is able to capture the correct and well-known buckling profile for this benchmark. Given that the entire load is applied at once, instead of "load vs displacement" curve we show "residual vs displacement" over all iterations of PN, Fig. 33(c). We also show the evolution of deformation over iteration in Fig. 33(d). For this example we finally activated the line search technique presented in Algorithm 3 but limited the minimum allowed step size to $\alpha = 0.1$. For the second problem, we apply a pull-out force radially on two sides of the cylinder and track the response, Fig. 32(b). As can be seen from Fig. 34 PN with a single load increment is again able to capture the correct and well-known buckling profile for this benchmark. Residual vs displacement and the evolution of deformation over all iterations of PN is shown in Fig. 34(c,d). For this example the system snaps at the onset of loading but PN with line search is able to successfully resolve this.

Finally, to showcase the robustness of our principal stretch-based tangent stabilisation, we simulate the pull-out of a thin semi-spherical elastomeric sheet using 10 increments of PN without employing any load control and path-following techniques and without employing the line search algorithm in Fig. 35. We use two meshes: one coarse Q2 hexahedral mesh and one fine P2 tetrahedral mesh using displacement-based formulation and the same material parameters as in the previous two examples but

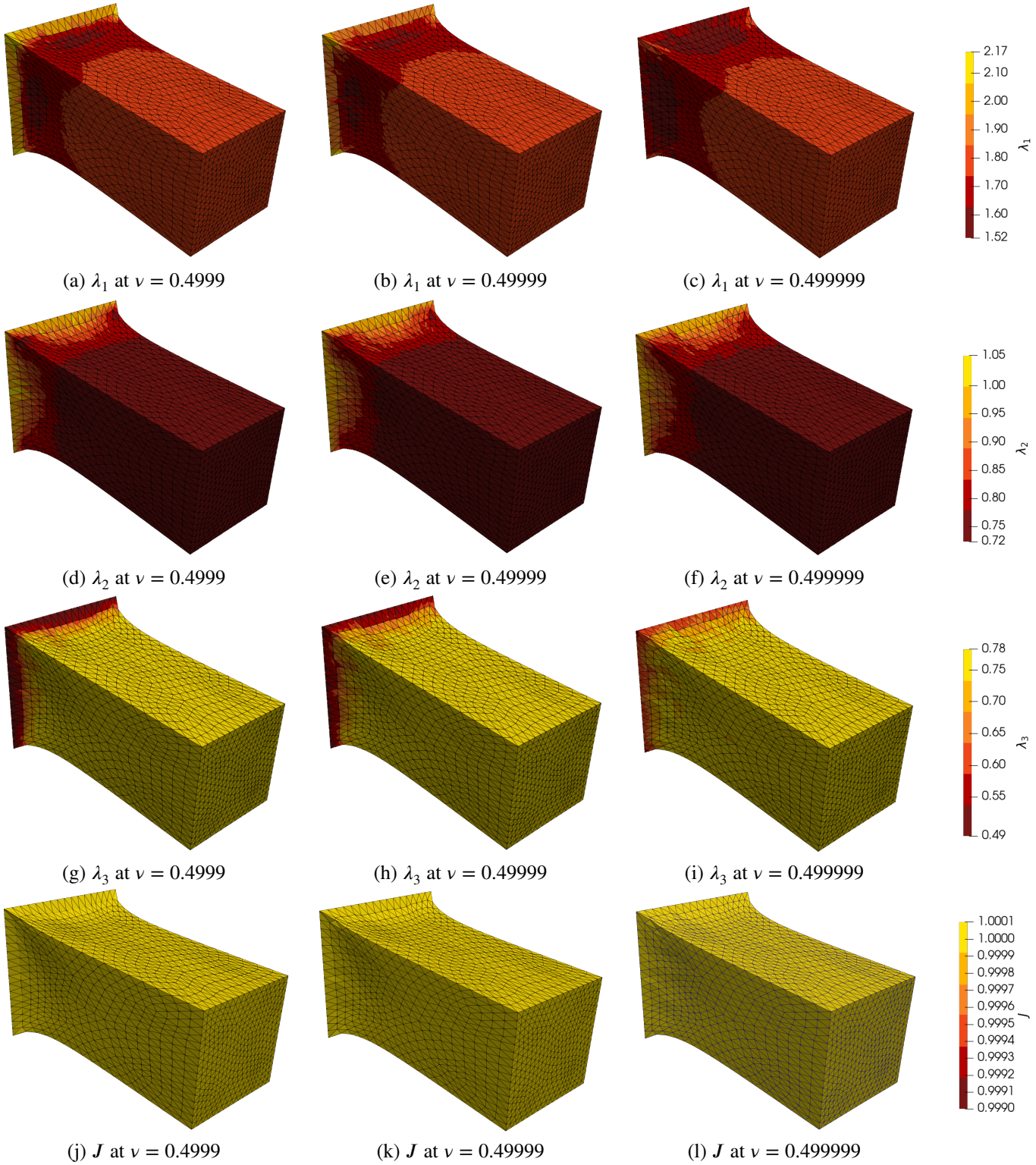

(a) λ_1 at $\nu = 0.4999$ (b) λ_1 at $\nu = 0.49999$ (c) λ_1 at $\nu = 0.499999$

(d) λ_2 at $\nu = 0.4999$ (e) λ_2 at $\nu = 0.49999$ (f) λ_2 at $\nu = 0.499999$

(g) λ_3 at $\nu = 0.4999$ (h) λ_3 at $\nu = 0.49999$ (i) λ_3 at $\nu = 0.499999$

(j) J at $\nu = 0.4999$ (k) J at $\nu = 0.49999$ (l) J at $\nu = 0.499999$

FIGURE 28 Mixed principal stretch formulation at the limit of incompressibility: The independent treatment of principal stretches that make up the Jacobian $J = \lambda_1\lambda_2\lambda_3$ offers enough flexibility for volumetric-locking-free analyses at the limit of incompressibility. Plots show (not-smoothed) distribution of the three principal stretches and the Jacobian J for Poisson's ratio $\nu = 0.4999$, $\nu = 0.49999$ and $\nu = 0.499999$.

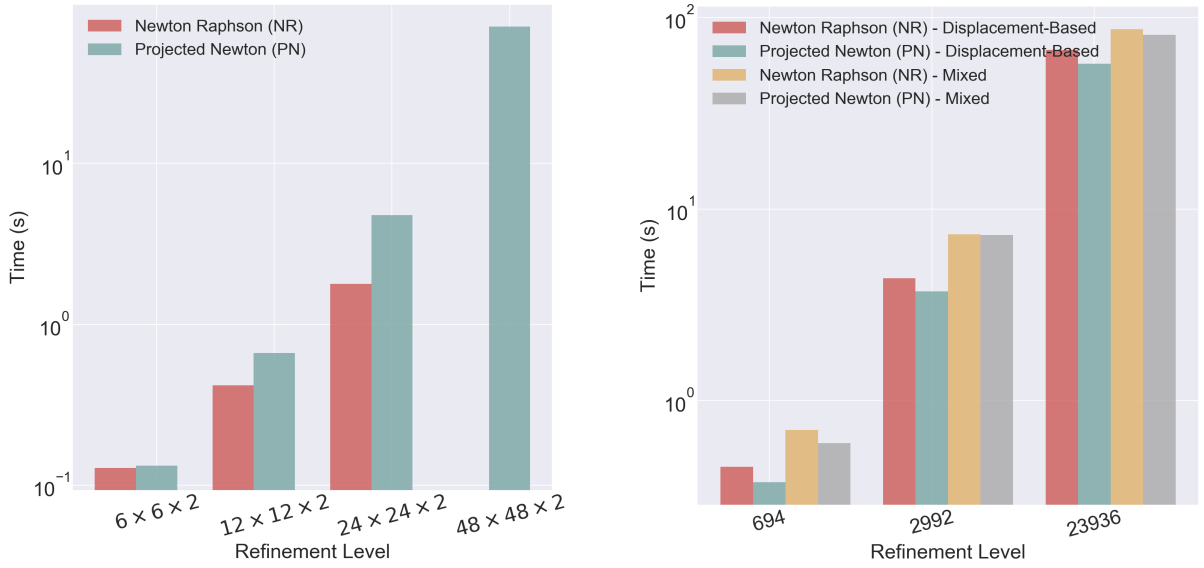

FIGURE 29 Comparison of total simulation time between NR and PN for (a) 2-dimensional square plate using displacement-based FEM, and (b) 3-dimensional inhomogeneous tension test using both displacement-based and mixed principal stretch FEMs. **Unlike NR, PN enables use of faster linear solvers**. Pardiso LU solver is used for NR and Pardiso LLT for PN.

increase the Poison's ratio to $\nu = 0.45$ and use the nearly incompressible Mooney-Rivlin model instead. While our framework is capable of simulating even higher order elements with competitive performance[84,17,21] it is well-known that for nonlinear elasticity problems parabolic meshes offer the best trade-off between cost and accuracy[85]. Certainly, with refinements, finer wrinkle patterns appear.

7.7 | Rigid simulations

Finally, we show the application of mixed rigid formulation presented in Section 4.2.1 in Fig. 36 with a bar hitting a rigid mechanical wheel simulated using Neumann boundary conditions. The wheel geometry and mesh is obtained from the publicly-available dataset Thingi10k and consequently the polynomial order of the mesh is increased to P2. The simulation is performed with displacements-based formulation by progressively increasing the shear modulus and compared to the rigid formulation. We note that, while our formulation has linear treatment of variables λ_is and Σ_{λ_i}s it still requires a parabolic mesh. Alternate and efficient formulations for stiff materials exist, for cases where engineering accuracy is not desired[3].

8 | CONCLUDING REMARKS

A new computational framework for large strain elasticity in principal stretches has been proposed in this work. Distinct from existing literature, the proposed formulation is based directly on the principal stretches of the deformation gradient rather than their squares i.e. eigenvalues of Cauchy-Green strain tensor which is archetypal in large strain elasticity formulations. The point of departure for our formulation is the recently developed stretch tensor invariants of Smith. B.[20] whose ingredients facilitate a systematic formulation of large strain elasticity in principal stretches.

The proposed formulation offers multiple novel features:

- Tangent elasticity and initial stiffness operators are by design constructed in a spectrally-decomposed form in that, their eigenvalues and eigenmatrices are derived analytically.

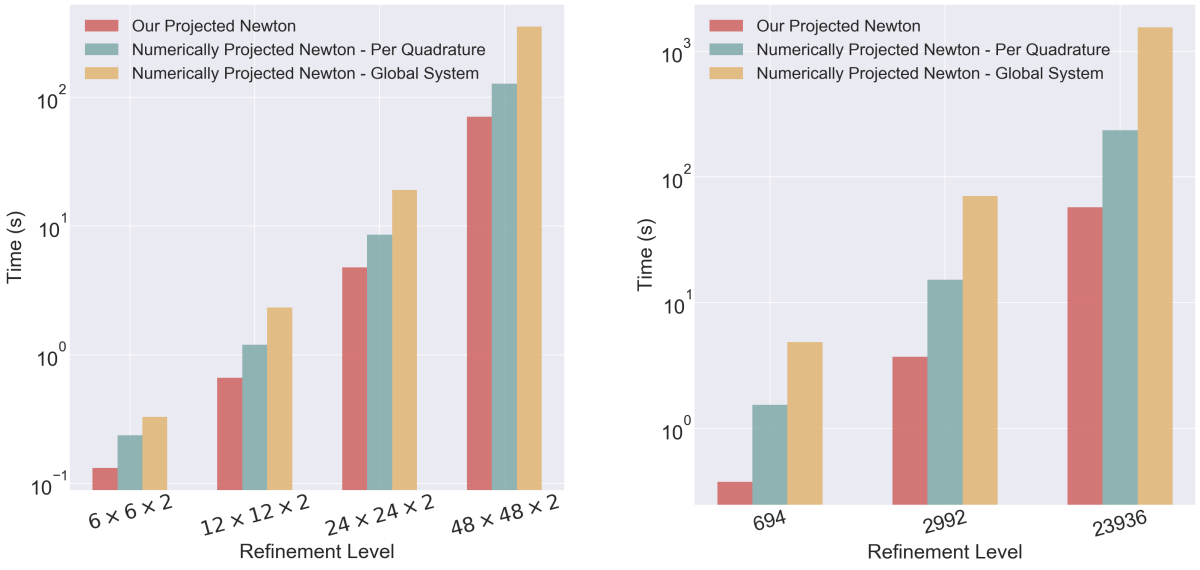

FIGURE 30 Timing comparison our proposed analytically constructed stabilised tangents with both local (per-quadrature; dense matrices) and global (sparse matrix) numerical eigen-decomposition of tangent matrices. Local numerical eigen-decomposition is up to 2× slower in 2D and over 4× in 3D while global numerical eigen-decomposition has over 10× the computational overhead and becomes forbiddingly time-consuming in practice. The two plots are for (a) 2-dimensional square plate test, and (b) 3-dimensional inhomogeneous tension test.

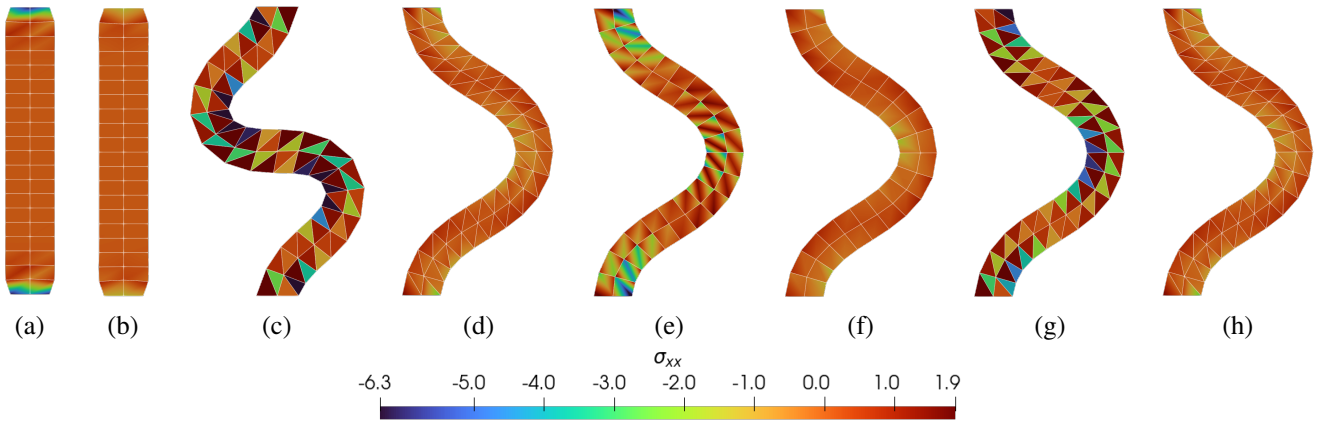

FIGURE 31 Tangent stabilisation makes simulations more stable since it prunes bifurcations. Figure shows pressing a bar with structured and unstructured meshes using NR (a,b,c,d) and PN (e,f,g,h). NR produces different profiles while PN produces the same profile regardless of the mesh or formulation used. (a) Q2 NR (b) Q2-Q1 NR (c) P2 NR (d) P2-P1 NR (e) Q2 PN (f) Q2-Q1 PN (g) P2 PN (h) P2-P1 PN.

- As a result, convexity conditions are postulated in terms of these newly found eigenvalues which happen to be closely related to the hypothesis of Ball [1].
- Therefore, this novel finding opens the door for utilising convex minimisation algorithms for isotropic hyperelasticity and in designing automated Newton-style algorithms via closed-form tangent stabilisation. In this context, a flavour of Projected Newton (PN) has been proposed and critically studied in this work.

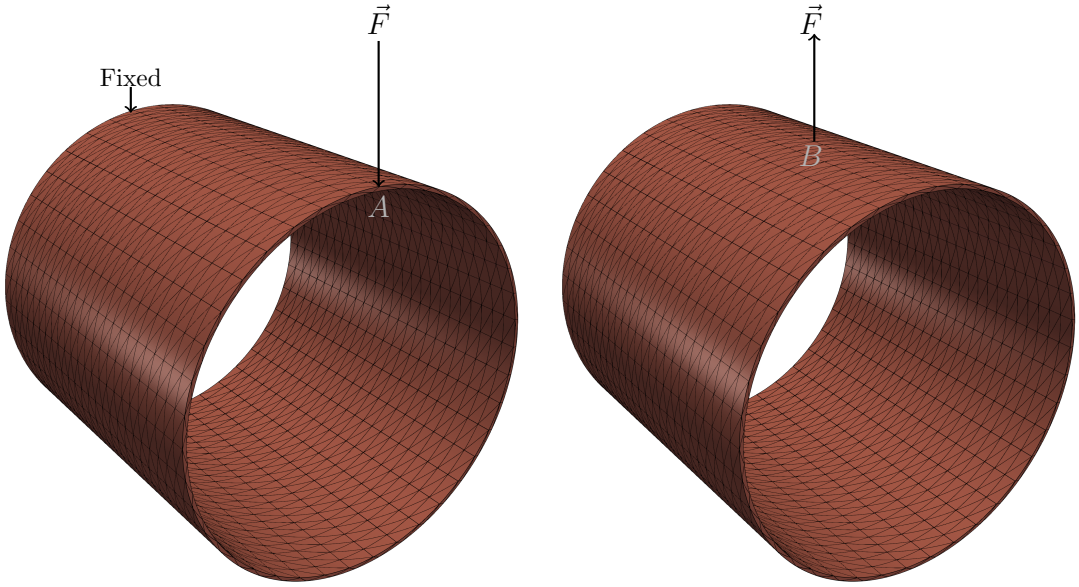

(a) Pinch (b) Pull-out

FIGURE 32 Geometry of cylindrical shell used for pinch and pull-out buckling analysis with thickness $h = 1mm$, radius $R = 100mm$, and length $L = 200mm$.

- Furthermore, formulating isotropic elasticity directly in terms of principal stretches facilitates the design of mixed Hu-Washizu variational formulations for compressible, nearly incompressible, truly incompressible, inextensible, rigid and stiff material models. This is done by treating principal stretches as independent variables and enforcing principal stretch-stress compatibility through additional Lagrange multipliers.

- Consequently, the proposed framework offers a general-purpose computational pipeline for locking-free and stress-accurate analyses of deformable objects as well as hybrid deformable-rigid simulations.

Our computational framework offers a “first step" implementation of the proposed ideas detailed above and there is certainly room for further research particularly in the context of engineering analysis. Firstly, compared to the well-known implementations of nonlinear solid mechanics specially in industry, our framework introduces additional computational cost emanating from Singular-Value-Decomposition (SVD) of deformation gradient per quadrature point. While, in 2-dimension we have observed that this additional step is often immeasurable (since SVD in $\mathbb{R}^2$ can be computed analytically) in 3-dimensions however, this introduces about 10-20% overhead. We use the fastest known implementation of SVD in $\mathbb{R}^3$ which is based on Jacobi conjugation and quaternions. It should be noted however, that other implementations of elasticity in principal stretches also report a similar overhead [30]. Furthermore, this operation is embarrassingly parallel if computed in batch-mode across all quadrature points [86]. We intend to explore this in future work.

The tangent stabilisation strategy and the subsequent Projected Newton (PN) minimisation algorithm discussed in detail in this work offers a robust mechanism for nonlinear analysis of solids and in particular provide an alternative to path-following and arc-length based techniques used in industry. Our experiments show that for engineering simulation purposes PN offers from roughly the same computational time to 2.5× slower compared to standard Newton-Raphson for a fixed accuracy. This cost is often largely subsided due to the ability to switch to faster linear solvers such as Cholesky and conjugate gradient methods. In turn however, PN offers robustness in simulation and convergence irrespective of mesh resolution and mesh quality. We note that, our tangent stabilisation is analytical and in fact comes cost-free and as discussed alternate numerical stabilisation techniques are forbiddingly time-consuming and impractical. Moreover, unlike Newton-Raphson, the convergence of PN deteriorates closer to the solution. It is possible to explore appropriate blending techniques that combine the benefit of both algorithms [19]. Additionally, we note that, away from engineering simulations and particularly in computer graphics and geometry processing PN has been successfully applied for well over a decade now for myriads of applications and constitutes the backbone of many optimisation tools [14,15,59,22].

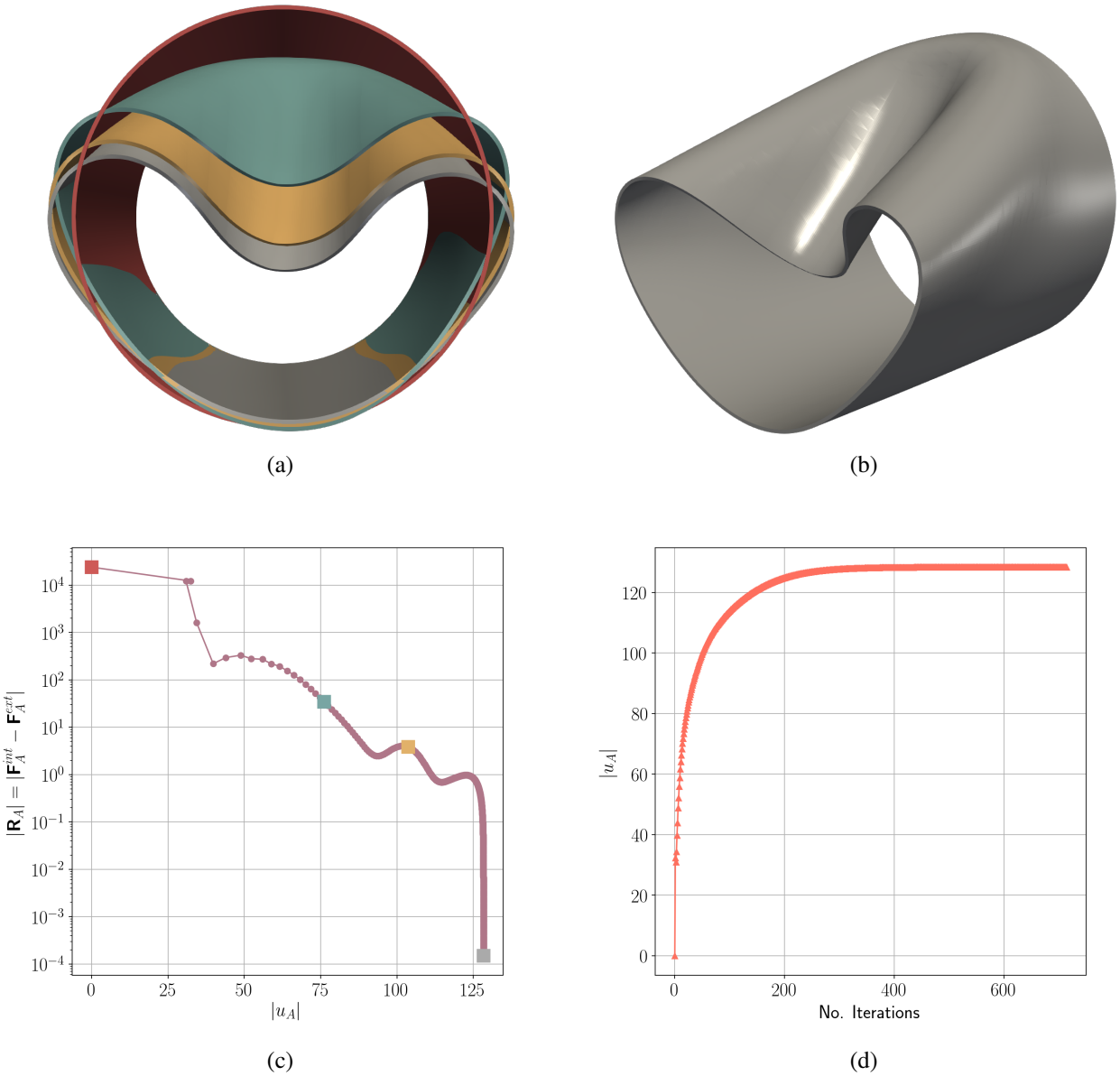

FIGURE 33 Deformed configuration of cylindrical shell for pinching problem at various iterations of PN using a single load increment. The buckled profile obtained with PN matches well the configuration obtained with path-following techniques[83]. Given that, the entire load is applied at once, instead of “load vs displacement" we track “residual vs displacement" over all iterations of PN.

Another issue typically encountered in principal stretch formulations is the case of equal or numerically similar singular-values. For displacement-based formulations (of any FE order), our implementation can completely circumvent this issue as isotropy dictates symmetry in principal stretches and we can analytically and rather symbolically (as shown in Fig. B1) evaluate the initial stiffness matrix. For the case of mixed formulations however, this remains an issue since neither analytic substitution is possible nor L’Hôpital rule applies. Although rare, numerical perturbation is required when such an issue is encountered. At times, this issue is exacerbated as principal stretches that are numerically very close but still above a threshold can cause a huge jump in the evaluation of initial stiffness. In such cases as discussed, we can either resubstitute the analytical formula assuming a displacement-based formulation or in the case of PN clamp the corresponding initial stiffness eigenvalues. In either case, this further dampens Newton algorithm which impacts convergence.

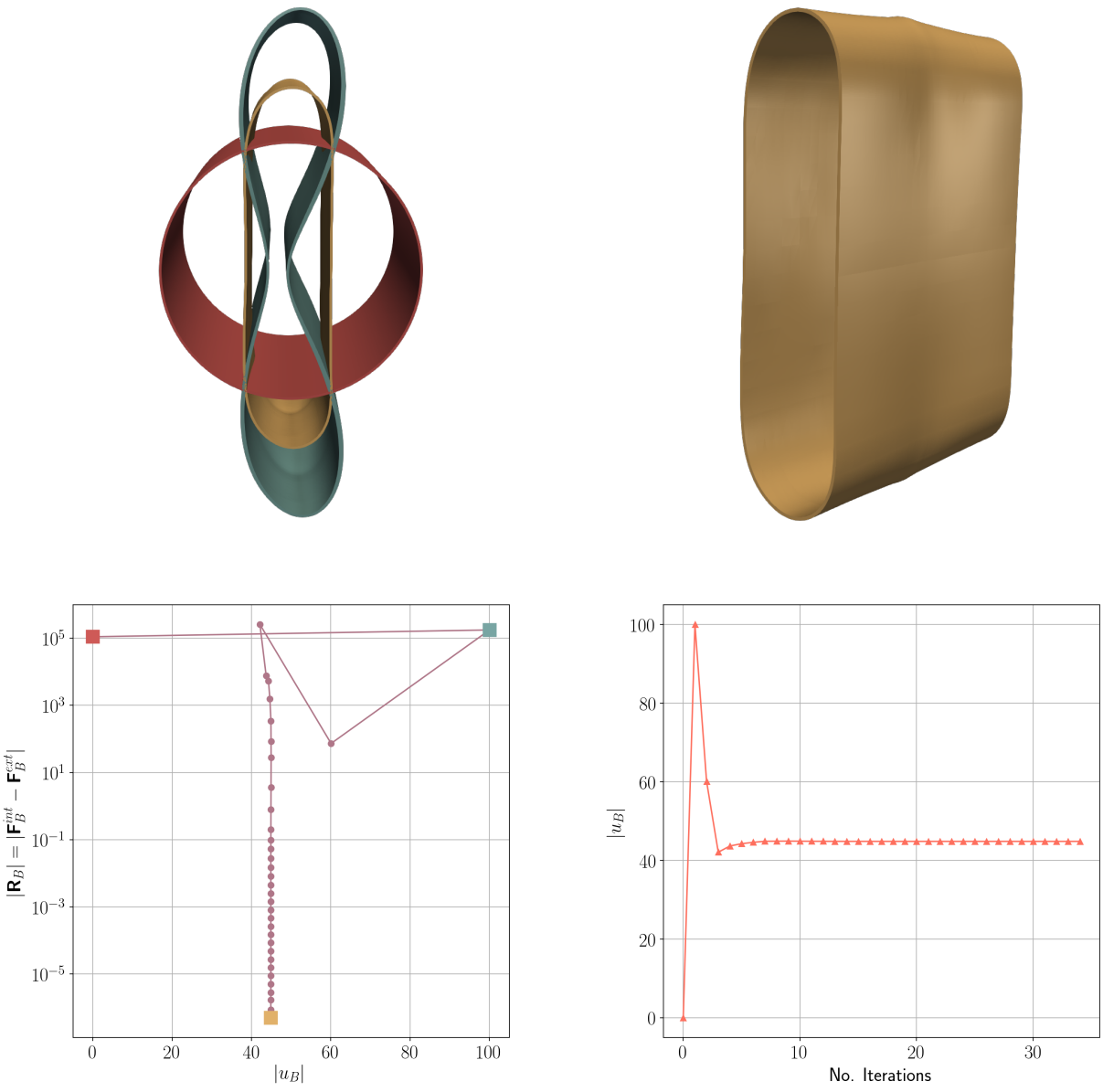

FIGURE 34 Deformed configuration of cylindrical shell for pull-out problem at various iterations of PN using a single load increment. The buckled profile obtained with PN matches well the configuration obtained with path-following techniques[83]. Given that, the entire load is applied at once, instead of “load vs displacement" we track “residual vs displacement" over all iterations of PN.

Finally, in the context of PN, maintaining injectivity or an inversion-free map becomes more important. While this often also happens with standard Newton-Raphson the issue is a lot more pronounced with PN. This is due to the fact that, PN offers numerical solvability even in physically hard and infeasible scenarios. For this reason, using coercive energies that tend to infinity as the element inverts such as incompressible models are mainly recommended. The combination of load increments (progressive loading) and line search alleviates this issue to a great extent. The line search algorithm used in our implementation is a standard backtracking algorithm and more sophisticated line search schemes exist that geometrically check for element inversion and limit the magnitude of descent to the largest possible inversion-safe step size[32,87]. Further investigation in the context of engineering analysis specially while using high order and mixed formulations is needed to determine the extent of feasibility of such algorithms.

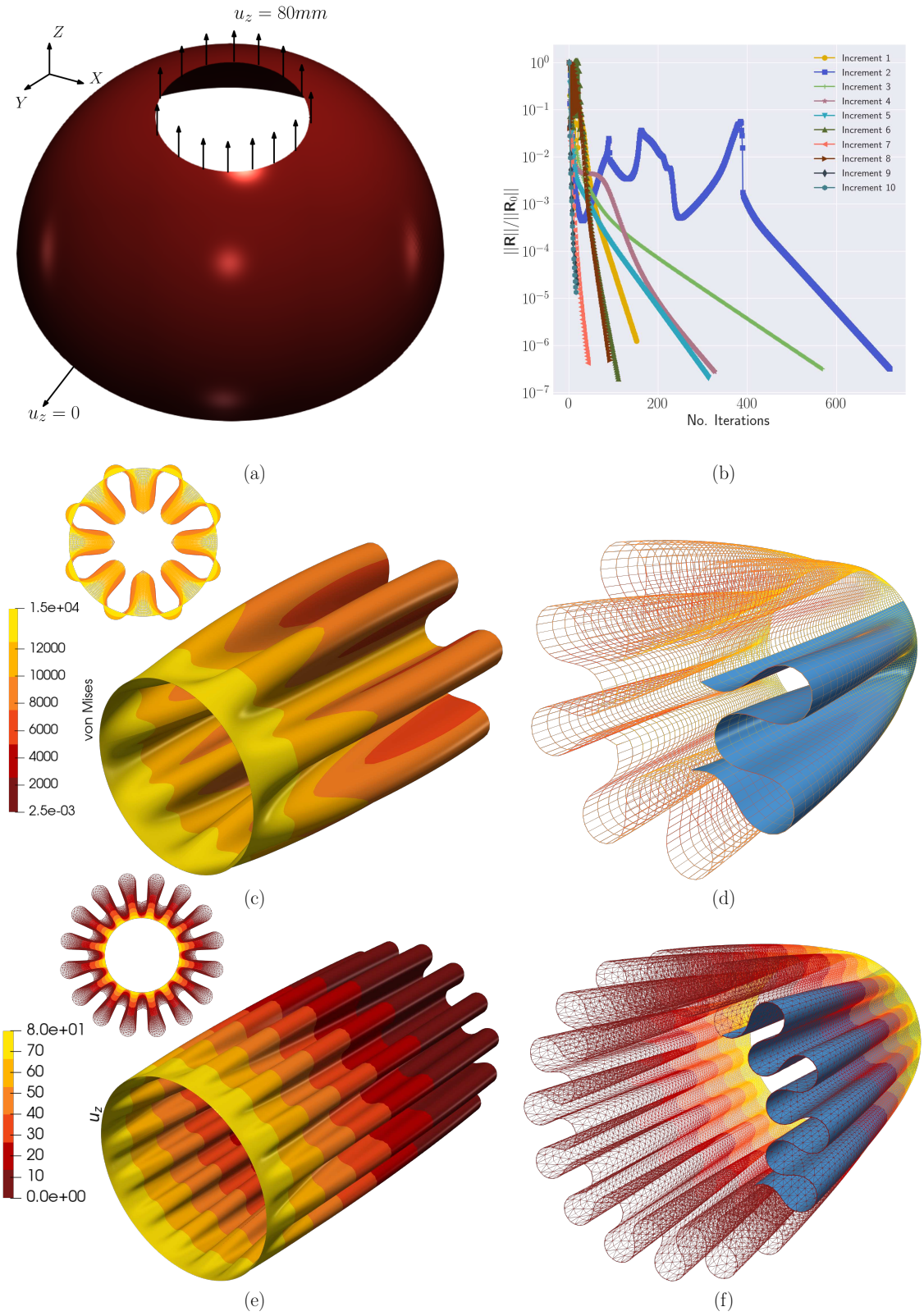

FIGURE 35 Coarse and fine wrinkles of an elastomeric sheet under extreme 2× pull-out simulated using the high order displacement-based formulation with Q2 and P2 elements: using Newton with stabilised tangents without employing any path following techniques or line search. a) Geometry and boundary conditions: sphere radius $r = 100mm$, height $L = 80mm$ and thickness $h = 0.1mm$; the base is fixed only in Z direction (allowed to slide in XY plane) and a displacement of $u_z = 80mm$ is applied at the top, c,d) rear and front views of deformed Q2 mesh showing smoothed von Mises stress, e,f) rear and front views of deformed P2 mesh showing u_z, and b) convergence of PN across all increments for Q2 mesh.

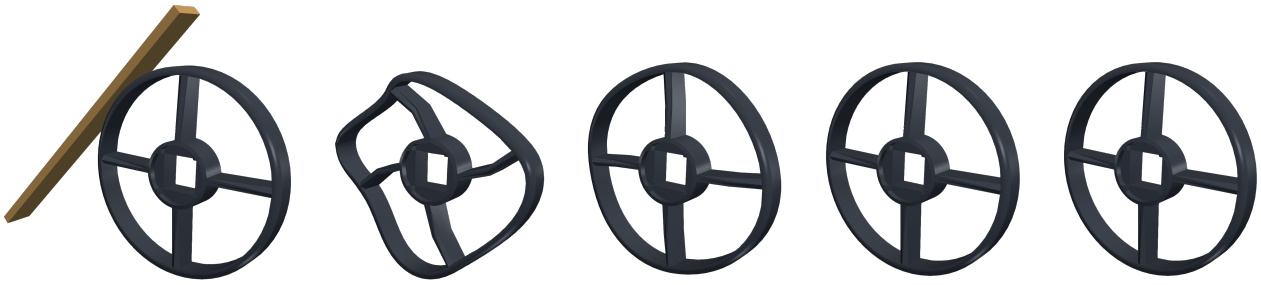

(a) Initial Configuration (b) 3 GPa (c) 30 GPa (d) 300 GPa (e) Rigid

FIGURE 36 Simulation of a bar hitting a rigid wheel: using displacement-based FEM with various shear moduli (b,c,d) and mixed rigid formulation (e).

ACKNOWLEDGEMENT

The first author thanks Brent Meranda manager of the Meshing & Abstraction, Simulation and Test Solutions, Siemens Digital Industries Software. The second author acknowledges the financial support through the contract 21132/SF/19, Fundaciòn Sèneca, Regiòn de Murcia (Spain), through the program Saavedra Fajardo. Second author is funded by Fundaciòn Sèneca (Murcia, Spain) through grant 20911/PI/18. The fourth author acknowledges the financial support received through the European Training Network ProTechtion (Project ID: 764636).

CONFLICT OF INTEREST

The authors declare no potential conflict of interests.

□

APPENDIX

A PROOF OF CONVEXITY CONDITIONS IN PRINCIPAL STRETCHES

The convexity conditions in Eqns. 47-48 are new in the sense that they are postulated in terms of the eigenvalues of the initial stiffness component $\boldsymbol{C}_p$ of the elasticity tensor (terms related with first derivatives of W) and in terms of the eigenvalues of the constitutive component $\boldsymbol{C}_k$ of the elasticity tensor (terms related with second derivatives of W). This is very convenient from a computational standpoint, specially when designing stabilisation strategies as those described throughout sections 3.2 and 3.3. However, the conditions derived in our corollaries are inevitably connected with the hypothesis established by Ball[1]. According to the latter work, provided that $W(\mathcal{A})$ is convex in its arguments, symmetric and monotonically increasing with respect to each of its arguments, then its equivalent expression $e(\boldsymbol{F})$ would be convex with respect to $\boldsymbol{F}$. If $W(\mathcal{A})$ meets these conditions (i.e. ***convexity***, ***symmetry*** and ***monotonically increasing***), it automatically satisfies the conditions stated in our previous corollaries. The objective of the following derivations is indeed to prove that, provided that $W(\mathcal{A})$ meets the requirements of ***convexity***, ***symmetry*** and ***monotonically increasing***, then the boxed conditions in Corollary 1 and 2 are automatically satisfied. Regarding the conditions involving the second derivatives in the boxes above, these follow from the ***convexity*** of W with respect to its arguments. Furthermore, it is trivial to see that the ***monotonically increasing*** behaviour of $W(\mathcal{A})$, which entails $\Sigma_{\lambda_i} := \frac{\partial W}{\partial \lambda_i} \geq 0$, automatically leads to the fulfillment of conditions of the type

$$\frac{\Sigma_{\lambda_i} + \Sigma_{\lambda_j}}{\lambda_i + \lambda_j} \geq 0, \qquad i \neq j. \tag{A1}$$

Finally, the ***convexity*** and ***monotically increasing*** nature of $W(\mathcal{A})$ automatically satisfy the remaining type of conditions, namely

$$\frac{\Sigma_{\lambda_i} - \Sigma_{\lambda_j}}{\lambda_i - \lambda_j} \geq 0, \qquad i \neq j. \tag{A2}$$

In order to see that, we will consider the case $i = 1$ and $j = 2$, for the three-dimensional case. Symmetry of $W : \mathbb{R}^3 \to \mathbb{R}$, $W = W(\lambda_1, \lambda_2, \lambda_3)$, entailed by the underlying isotropy of the material, requires that

$$W(a,b,c) = W(b,a,c); \qquad W(a,b,c) = W(c,b,a); \qquad W(a,b,c) = W(a,c,b), \tag{A3}$$

where it is implicitly stated that

$$W(a,b,c) = W(\lambda_1, \lambda_2, \lambda_2)\big|_{\lambda_1=a, \lambda_2=b, \lambda_3=c} \tag{A4}$$

Furthermore, symmetry of $W(\lambda_1, \lambda_2)$ has also implications on its first partial derivatives, as the following result also holds

$$\frac{\partial W(a,b,c)}{\partial \lambda_1} = \frac{\partial W(b,a,c)}{\partial \lambda_2}; \qquad \frac{\partial W(a,b,c)}{\partial \lambda_1} = \frac{\partial W(c,b,a)}{\partial \lambda_3}; \qquad \frac{\partial W(a,b,c)}{\partial \lambda_2} = \frac{\partial W(a,c,b)}{\partial \lambda_3} \tag{A5}$$

where it is implicitly stated that

$$\frac{\partial W(a,b,c)}{\partial \lambda_1} = \frac{\partial W(\lambda_1, \lambda_2, \lambda_3)}{\partial \lambda_1}\bigg|_{\lambda_1=a, \lambda_2=b, \lambda_3=c} \tag{A6}$$

Notice that any of the equalities A5 can be easily proven from the definition of partial derivative. For brevity, we only show $A5_a$

$$\frac{\partial W(a,b,c)}{\partial \lambda_1} = \lim_{h\to 0} \frac{W(a+h,b,c) - W(a,b,c)}{h} = \lim_{h\to 0} \frac{W(b,a+b,c) - W(b,a,c)}{h} = \frac{\partial W(b,a,c)}{\partial \lambda_2} \tag{A7}$$

The inequality associated definition of convexity in equation 43 also holds whenever it is divided by a positive number. For convenience, we chose $(a-b)^2$, i.e.

$$\frac{\big(\boldsymbol{\nabla} W(\mathcal{A}_1) - \boldsymbol{\nabla} W(\mathcal{A}_2)\big) \cdot \big(\mathcal{A}_1 - \mathcal{A}_2\big)}{(a-b)^2} \geq 0 \tag{A8}$$

Taking $\mathcal{A}_1 = (a,b,c)$ and $\mathcal{A}_2 = (b,a,c)$ into (A8) yields

$$\frac{\big(\boldsymbol{\nabla} W(\mathcal{A}_1) - \boldsymbol{\nabla} W(\mathcal{A}_2)\big) \cdot \big(\mathcal{A}_1 - \mathcal{A}_2\big)}{(a-b)^2} = \frac{\left(\frac{\partial W(a,b,c)}{\partial \lambda_1} - \frac{\partial W(b,a,c)}{\partial \lambda_1} - \frac{\partial W(a,b,c)}{\partial \lambda_2} + \frac{\partial W(b,a,c)}{\partial \lambda_2}\right)}{a-b} \geq 0 \tag{A9}$$

Use of the symmetry condition in A5 into the second and fourth terms on the right hand side of equation A9, enables to equivalently re-write A9 as

$$\frac{\big(\boldsymbol{\nabla} W(\mathcal{A}_1) - \boldsymbol{\nabla} W(\mathcal{A}_2)\big) \cdot \big(\mathcal{A}_1 - \mathcal{A}_2\big)}{(a-b)^2} = \frac{\left(\frac{\partial W(a,b,c)}{\partial \lambda_1} - \frac{\partial W(a,b,c)}{\partial \lambda_2} - \frac{\partial W(a,b,c)}{\partial \lambda_2} + \frac{\partial W(a,b,c)}{\partial \lambda_1}\right)}{a-b} = 2\frac{\left(\frac{\partial W(a,b,c)}{\partial \lambda_1} - \frac{\partial W(a,b,c)}{\partial \lambda_2}\right)}{a-b} \geq 0 \tag{A10}$$

As a result, since above equation A10 is satisfied $\forall a, b, c \in \mathbb{R}$, we can finally conclude that

$$\frac{\left(\frac{\partial W(\lambda_1,\lambda_2,\lambda_3)}{\partial \lambda_1} - \frac{\partial W(\lambda_1,\lambda_2,\lambda_3)}{\partial \lambda_2}\right)}{\lambda_1 - \lambda_2} \geq 0 \Rightarrow \frac{\Sigma_{\lambda_1} - \Sigma_{\lambda_2}}{\lambda_1 - \lambda_2} \geq 0. \tag{A11}$$

B ANALYTIC EIGENSYSTEM OF REAL SYMMETRIC 3×3 SYSTEM

The analytic eigensystem of Hessian $\boldsymbol{H}_W$ for the 2-dimensional case was presented in Eqns. 60-61. Given its real symmetric nature, the eigensystem of Hessian $\boldsymbol{H}_W$ can also be obtained in closed-form in 3-dimensions. More specifically, rewriting $\boldsymbol{H}_W$

in the form

$$\boldsymbol{H}_W = \begin{bmatrix} \frac{\partial^2 W}{\partial \lambda_1 \partial \lambda_1} & \frac{\partial^2 W}{\partial \lambda_1 \partial \lambda_2} & \frac{\partial^2 W}{\partial \lambda_1 \partial \lambda_3} \\ & \frac{\partial^2 W}{\partial \lambda_2 \partial \lambda_2} & \frac{\partial^2 W}{\partial \lambda_2 \partial \lambda_3} \\ sym & & \frac{\partial^2 W}{\partial \lambda_3 \partial \lambda_3} \end{bmatrix} = \begin{bmatrix} a & d & f \\ & b & e \\ sym & & c \end{bmatrix} \tag{B12}$$

The eigenvalues can be computed as (c.f. Deledalle et. al.[58])

$$\bar{\lambda}_1^{\boldsymbol{H}_W} = a + b + c - 2\sqrt{x_1}\cos(\frac{\phi}{3}), \tag{B13a}$$

$$\bar{\lambda}_2^{\boldsymbol{H}_W} = a + b + c + 2\sqrt{x_1}\cos(\frac{\phi - \pi}{3}), \tag{B13b}$$

$$\bar{\lambda}_3^{\boldsymbol{H}_W} = a + b + c + 2\sqrt{x_1}\cos(\frac{\phi + \pi}{3}), \tag{B13c}$$

where ϕ is given by

$$\phi = \begin{cases} \text{atan}\left(\frac{\sqrt{4x_1^3 - x_2^2}}{x_2}\right) & \text{if } x_2 > 0 \\ \frac{\pi}{2} & \text{if } x_2 = 0 \\ \text{atan}\left(\frac{\sqrt{4x_1^3 - x_2^2}}{x_2}\right) + \pi & \text{if } x_2 < 0 \end{cases} \tag{B14}$$

where

$$x_1 = a^2 + b^2 + c^2 + 3(d^2 + e^2 + f^2) - ab - ac - bc, \tag{B15a}$$

$$x_2 = -(2a - b - c)(2b - a - c)(2c - a - b) + 9\left((2a - b - c)e^2 + (2b - a - c)f^2 + (2c - a - b)d^2\right) - 54def. \tag{B15b}$$

The eigenvectors are given by

$$\boldsymbol{e}_1 = [\frac{\bar{\lambda}_1^{\boldsymbol{H}_W} - c - em_1}{f}, m_1, 1]_n^T, \quad \boldsymbol{e}_2 = [\frac{\bar{\lambda}_2^{\boldsymbol{H}_W} - c - em_2}{f}, m_2, 1]_n^T, \quad \boldsymbol{e}_3 = [\frac{\bar{\lambda}_3^{\boldsymbol{H}_W} - c - em_3}{f}, m_3, 1]_n^T, \tag{B16}$$

where

$$m_1 = \frac{d(c - \bar{\lambda}_1^{\boldsymbol{H}_W}) - ef}{f(b - \bar{\lambda}_1^{\boldsymbol{H}_W}) - de}, \quad m_2 = \frac{d(c - \bar{\lambda}_2^{\boldsymbol{H}_W}) - ef}{f(b - \bar{\lambda}_2^{\boldsymbol{H}_W}) - de}, \quad m_3 = \frac{d(c - \bar{\lambda}_3^{\boldsymbol{H}_W}) - ef}{f(b - \bar{\lambda}_3^{\boldsymbol{H}_W}) - de}. \tag{B17}$$

References

1. Ball JM. Convexity conditions and existence theorems in nonlinear elasticity. *Archive for Rational Mechanics and Analysis* 1976; 63(4): 337-403.

2. Podio-Guidugli P, Caffarelli GV. Extreme elastic deformations. *Archive for Rational Mechanics and Analysis* 1991; 115: 311–328. doi: https://doi.org/10.1007/BF00375278

3. Lan L, Kaufman DM, Li M, Jiang C, Yang Y. Affine Body Dynamics: Fast, Stable and Intersection-Free Simulation of Stiff Materials. *ACM Trans. Graph.* 2022; 41(4). doi: 10.1145/3528223.3530064

4. Bonet J, Gil AJ, Ortigosa R. A computational framework for polyconvex large strain elasticity. *Computer Methods in Applied Mechanics and Engineering* 2015; 283: 1061-1094.

5. Bonet J, Gil AJ, Ortigosa R. On a tensor cross product based formulation of large strain solid mechanics. *International Journal of Solids and Structures* 2016; 84: 49-63.

2D Eigensystem

```
from sympy import *

def GetFirstPiolaAndTangentsEigenSystemSymbolically(W):
    """Given energy W expressed in terms of singular values
    of F: (l1, l2) returns principal components of first
    Piola-Kirchhoff and analytic eigenvalues of initial
    stiffness and Hessian operators"""

    # ------------------------------------------------#
    # First Piola-Kirchhoff stress tensor [P = U * sigmaP * V^T]
    sigmaP = zeros(2,1)
    sigmaP[0] = diff(W, l1)
    sigmaP[1] = diff(W, l2)
    # ------------------------------------------------#

    # ------------------------------------------------#
    # Initial stiffness eigenvalues
    lambdasIS = zeros(2,1)
    lambdasIS[0] = (diff(W, l1) - diff(W, l2)) / (l1 - l2)
    lambdasIS[1] = (diff(W, l1) + diff(W, l2)) / (l1 + l2)
    # ------------------------------------------------#

    # ------------------------------------------------#
    # Hessian matrix
    Hw = zeros(2,2)

    Hw[0,0] = diff(W, l1, 2)
    Hw[1,1] = diff(W, l2, 2)

    Hw[0,1] = diff(diff(W, l1), l2)

    Hw[1,0] = Hw[0,1]

    # Get its eigenvalues
    lambdasHw = Hw.eigenvals().items()
    # ------------------------------------------------#

    return sigmaP, lambdasIS, lambdasHw
```

3D Eigensystem

```
from sympy import *

def GetFirstPiolaAndTangentsEigenSystemSymbolically(W):
    """Given energy W expressed in terms of singular values
    of F: (l1, l2, l3) returns principal components of first
    Piola-Kirchhoff and analytic eigenvalues of initial
    stiffness and Hessian operators"""

    # ------------------------------------------------#
    # First Piola-Kirchhoff stress tensor [P = U * sigmaP * V^T]
    sigmaP = zeros(3,1)
    sigmaP[0] = diff(W, l1)
    sigmaP[1] = diff(W, l2)
    sigmaP[2] = diff(W, l3)
    # ------------------------------------------------#

    # ------------------------------------------------#
    # Initial stiffness eigenvalues
    lambdasIS = zeros(6,1)
    lambdasIS[0] = (diff(W, l2) - diff(W, l3)) / (l2 - l3)
    lambdasIS[1] = (diff(W, l1) - diff(W, l3)) / (l1 - l3)
    lambdasIS[2] = (diff(W, l1) - diff(W, l2)) / (l1 - l2)
    lambdasIS[3] = (diff(W, l2) + diff(W, l3)) / (l2 + l3)
    lambdasIS[4] = (diff(W, l1) + diff(W, l3)) / (l1 + l3)
    lambdasIS[5] = (diff(W, l1) + diff(W, l2)) / (l1 + l2)
    # ------------------------------------------------#

    # ------------------------------------------------#
    # Hessian matrix
    Hw = zeros(3,3)

    Hw[0,0] = diff(W, l1, 2)
    Hw[1,1] = diff(W, l2, 2)
    Hw[2,2] = diff(W, l3, 2)

    Hw[0,1] = diff(diff(W, l1), l2)
    Hw[0,2] = diff(diff(W, l1), l3)
    Hw[1,2] = diff(diff(W, l2), l3)

    Hw[1,0] = Hw[0,1]
    Hw[2,0] = Hw[0,2]
    Hw[2,1] = Hw[1,2]

    # Get its eigenvalues
    lambdasHw = Hw.eigenvals().items()
    # ------------------------------------------------#

    return sigmaP, lambdasIS, lambdasHw
```

FIGURE B1 Symbolic code for obtaining Piola-Kirchhoff and eigensystem of tangent operators in 2D and 3D.

6. Schröder J, Wriggers P, Balzani D. A new mixed finite element based on different approximations of the minors of deformation tensors. *Computer Methods in Applied Mechanics and Engineering* 2011; 200(49–52): 3583–3600.

7. Kraus A, Wriggers P, Viebahn N, Schröder J. Low order locking–free mixed finite element formulation with approximation of the minors of the deformation gradient. *International Journal for Numerical Methods in Engineering* 2019; 120: 1011–1026.

8. Ansys. https://www.ansys.com/; 2022.

9. Abaqus FEA. https://www.3ds.com/products-services/simulia/products/abaqus/; 2022.

10. Crisfield MA. *Nonlinear Finite Element Analysis of Solids and Structures: Essentials*. Chichester, West Sussex, United Kingdom: John Wiley & Sons . 1996.

11. Souza Neto E. A. d, Perić D, Owen DRJ. *Computational Methods for Plasticity: Theory and Applications*. Chichester, West Sussex, United Kingdom: John Wiley & Sons. first ed. 2008.

12. Nocedal J, Wright SJ. *Numerical Optimization*. New York, NY: Springer. second ed. 2006

13. Kovalsky SZ, Galun M, Lipman Y. Accelerated Quadratic Proxy for Geometric Optimization. *ACM Trans. Graph.* 2016; 35(4). doi: 10.1145/2897824.2925920

14. Teran J, Sifakis E, Irving G, Fedkiw R. Robust Quasistatic Finite Elements and Flesh Simulation. In: SCA '05. Association for Computing Machinery; 2005; New York, NY, USA: 181–190

15. Stomakhin A, Howes R, Schroeder C, Teran JM. Energetically Consistent Invertible Elasticity. In: Lee J, Kry P., eds. *Eurographics/ ACM SIGGRAPH Symposium on Computer Animation*The Eurographics Association; 2012

16. Gargallo-Peiró A, Roca X, Peraire J, Sarrate J. Optimization of a regularized distortion measure to generate curved high-order unstructured tetrahedral meshes. *International Journal for Numerical Methods in Engineering* 2015; 103(5): 342–363.

17. Poya R, Sevilla R, Gil AJ. A unified approach for a posteriori high-order curved mesh generation using solid mechanics. *Computational Mechanics* 2016; 58(3): 457–490. doi: 10.1007/s00466-016-1302-2

18. Shtengel A, Poranne R, Sorkine-Hornung O, Kovalsky SZ, Lipman Y. Geometric Optimization via Composite Majorization. *ACM Trans. Graph.* 2017; 36(4). doi: 10.1145/3072959.3073618

19. Zhu Y, Bridson R, Kaufman DM. Blended Cured Quasi-Newton for Distortion Optimization. *ACM Trans. Graph.* 2018; 37(4).

20. Smith B, Goes FD, Kim T. Analytic Eigensystems for Isotropic Distortion Energies. *ACM Trans. Graph.* 2019; 38(1). doi: 10.1145/3241041

21. Poya R, Gil AJ, Ortigosa R, Sevilla R, Bonet J, Wall WA. A curvilinear high order finite element framework for electromechanics: From linearised electro-elasticity to massively deformable dielectric elastomers. *Computer Methods in Applied Mechanics and Engineering* 2018; 329: 75-117. doi: https://doi.org/10.1016/j.cma.2017.09.020

22. Kim T, Eberle D. Dynamic Deformables: Implementation and Production Practicalities (Now with Code!). In: SIGGRAPH '22. Association for Computing Machinery; 2022; New York, NY, USA

23. Hilber HM, Hughes TJR, Taylor RL. Improved numerical dissipation for time integration algorithms in structural dynamics. *Earthquake Engineering and Structural Dynamics* 1977; 5: 282-292.

24. Chung J, Hubert GM. A time integration algorithm for structural dynamics with improved numerical dissipation: The generalized-alpha method. *ASME Journal of Applied Mechanics* 1993; 60: 371-375.

25. Toulorge T, Geuzaine C, Remacle JF, Lambrechts J. Robust untangling of curvilinear meshes. *Journal of Computational Physics* 2013; 254: 8–26.

26. Garanzha V, Kaporin IE. Regularization of the barrier variational method of grid generation. *Computational Mathematics and Mathematical Physics* 1999; 39(9): 1426-1440.

27. Su JP, Fu X, Liu L. Practical Foldover–Free Volumetric Mapping Construction. *Computer Graphics Forum* 2019; 38.

28. Miehe C. Aspects of the formulation and finite element implementation of large strain isotropic elasticity. *International Journal for Numerical Methods in Engineering* 1994; 37(12): 1981–2004. doi: https://doi.org/10.1002/nme.1620371202

29. Xu H, Sin F, Zhu Y, Barbič J. Nonlinear Material Design Using Principal Stretches. *ACM Trans. Graph.* 2015; 34(4). doi: 10.1145/2766917

30. Connolly S, Mackenzie D, Gorash Y. Isotropic hyperelasticity in principal stretches: explicit elasticity tensors and numerical implementation. *Comput Mech* 2019; 64: 1273–1288. doi: https://doi.org/10.1007/s00466-019-01707-1

31. Zhu Y. Eigen Space of Mesh Distortion Energy Hessian. 2021. doi: https://arxiv.org/pdf/2103.08141.pdf

32. Smith J, Schaefer S. Bijective parameterization with free boundaries. *ACM Trans. Graphs.* 2015; 34: 1–9. doi: 10.1145/2766947

33. Rabinovich M, Poranne R, Panozzo D, Sorkine-Hornung O. Scalable Locally Injective Mappings. *ACM Trans. Graph.* 2017; 36(2). doi: 10.1145/2983621

34. Sorkine O, Alexa M. As-rigid-as-possible surface modeling. In: SGP 2007. Eurographics Association; 2007: 109–116.

35. Liu L, Zhang L, Xu Y, Gotsman C, Gortler SJ. A Local/Global Approach to Mesh Parameterization. In: SGP '08. Eurographics Association; 2008; Goslar, DEU: 1495-1504.

36. Trusty T, Kaufman DM, Levin DIW. Mixed Variational Finite Elements for Implicit, General-Purpose Simulation of Deformables. *CoRR* 2022; abs/2202.00183.

37. Chapelle D, Bathe K. The inf–sup test. *Computers and Structures* 1993; 47(4): 537-545. doi: https://doi.org/10.1016/0045-7949(93)90340-J

38. Brezzi F, Bathe KJ. A discourse on the stability conditions for mixed finite element formulations. *Computer Methods in Applied Mechanics and Engineering* 1990; 82(1): 27-57. Proceedings of the Workshop on Reliability in Computational Mechanicsdoi: https://doi.org/10.1016/0045-7825(90)90157-H

39. Auricchio F, Beirao da Veiga L, Lovadina C, Reali A. A stability study of some mixed finite elements for large deformation elasticity problems. *Computer Methods in Applied Mechanics and Engineering* 2005; 194(9): 1075-1092. doi: https://doi.org/10.1016/j.cma.2004.06.014

40. Auricchio F, Beirao da Veiga L, Lovadina C, Reali A. The importance of the exact satisfaction of the incompressibility constraint in nonlinear elasticity: mixed FEMs versus NURBS-based approximations. *Computer Methods in Applied Mechanics and Engineering* 2010; 199(5): 314-323. Computational Geometry and Analysisdoi: https://doi.org/10.1016/j.cma.2008.06.004

41. Auricchio F, Veiga dLB, Brezzi F, Lovadina C. *Mixed Finite Element Methods*: 1-53; John Wiley and Sons, Ltd . 2017

42. Boer dR. *Vektor- und Tensorrechnung für Ingenieure*. Springer . 1982.

43. Bonet J, Gil AJ, Lee CH, Aguirre M, Ortigosa R. A first order hyperbolic framework for large strain computational solid dynamics. Part I: Total Lagrangian isothermal elasticity. *Computer Methods in Applied Mechanics and Engineering* 2015; 283: 689-732.

44. Poya R, Ortigosa R, Kim T. Geometric Optimisation Via Spectral Shifting. *ACM Trans. Graph.* 2023; 42(3). doi: 10.1145/3585003

45. Simo JC, Taylor RL. Quasi-incompressible finite elasticity in principal stretches. continuum basis and numerical algorithms. *Computer Methods in Applied Mechanics and Engineering* 1991; 85(3): 273–310. doi: https://doi.org/10.1016/0045-7825(91)90100-K

46. Miehe C. Computation of isotropic tensor functions. *Communications in Numerical Methods in Engineering* 1993; 9(11): 889–896. doi: https://doi.org/10.1002/cnm.1640091105

47. Chen YC, Wheeler L. Derivatives of the stretch and rotation tensors. *Journal of Elasticity* 1993; 32: 175–182.

48. Rosati L. Derivatives and Rates of the Stretch and Rotation Tensors. *Journal of Elasticity* 1999; 56: 213–230.

49. Gil AJ, Ortigosa R. A new framework for large strain electromechanics based on convex multi-variable strain energies: Variational formulation and material characterisation. *Computer Methods in Applied Mechanics and Engineering* 2016; 302: 293 - 328. doi: http://dx.doi.org/10.1016/j.cma.2015.11.036

50. Hartmann S, Neff P. Polyconvexity of generalized polynomial-type hyperelastic strain energy functions for near-incompressibility. *International Journal of Solids and Structures* 2003; 40: 2767–2791.

51. Dacorogna B. *Direct Methods in the Calculus of Variations*. 78. Springer. 2nd ed. 2008

52. Horák M, Gil AJ, Ortigosa R, Kružík M. A polyconvex transversely-isotropic invariant-based formulation for electromechanics: Stability, minimisers and computational implementation. *Computer Methods in Applied Mechanics and Engineering* 2023; 403: 115695. doi: https://doi.org/10.1016/j.cma.2022.115695

53. Martin RJ, Voss J, Ghiba ID, Sander O, Neff P. The Quasiconvex Envelope of Conformally Invariant Planar Energy Functions in Isotropic Hyperelasticity. *Journal of Nonlinear Science* 2020; 30: 2885–2923.

54. Ghiba ID, Martin RJ, Neff P. Rank-one convexity implies polyconvexity in isotropic planar incompressible elasticity. *Journal de Mathématiques Pures et Appliquées* 2018; 116: 88-104. doi: https://doi.org/10.1016/j.matpur.2018.06.009

55. Ortigosa R, Gil AJ, Bonet J, Hesch C. A computational framework for polyconvex large strain elasticity for geometrically exact beam theory. *Computational Mechanics* 2016; 57(2): 277–303.

56. Gil AJ, Ortigosa R, Lee CH. A computational framework for large strain nearly and truly incompressible electromechanics based on convex multi-variable strain energies. *Computer Methods in Applied Mechanics and Engineering* 2016; 310: 297 - 334. doi: http://dx.doi.org/10.1016/j.cma.2016.06.025

57. Golub GH, Van Loan CF. *Matrix Computations*. Baltimore, USA: Johns Hopkins Studies in Mathematical Sciences. 4th ed. 2012.

58. Deledalle CA, Denis L, Tabti S, Tupin F. Closed-form expressions of the eigen decomposition of 2x2 and 3x3 Hermitian matrices. *Research Report, Universite de Lyon* 2017.

59. Smith B, Goes FD, Kim T. Stable Neo-Hookean Flesh Simulation. *ACM Trans. Graph.* 2018; 37(2). doi: 10.1145/3180491

60. Garanzha V, Kudryavtseva LN, Utyuzhnikov S. Variational method for untangling and optimization of spatial meshes. *J. Comput. Appl. Math.* 2014; 269: 24-41.

61. Fu XM, Liu Y, Guo B. Computing Locally Injective Mappings by Advanced MIPS. *ACM Trans. Graph.* 2015; 34(4). doi: 10.1145/2766938

62. Garanzha V, Kaporin I, Kudryavtseva L, Protais F, Ray N, Sokolov D. Foldover-Free Maps in 50 Lines of Code. *ACM Trans. Graph.* 2021; 40(4). doi: 10.1145/3450626.3459847

63. Lévy B, Petitjean S, Ray N, Maillot J. Least Squares Conformal Maps for Automatic Texture Atlas Generation. *ACM Trans. Graph.* 2002; 21(3): 362–371. doi: 10.1145/566654.566590

64. Neff P, Jeong J. A new paradigm: the linear isotropic Cosserat model with conformally invariant curvature energy. *ZAMM - Zeitschrift für Angewandte Mathematik und Mechanik* 2009; 89: 107-122.

65. Hormann K, Greiner G. MIPS: An Efficient Global Parametrization Method. In: ; 2000: 153–162.

66. Cervera M, Chiumenti M, Codina R. Mixed stabilized finite element methods in nonlinear solid mechanics: Part I: Formulation. *Computer Methods in Applied Mechanics and Engineering* 2010; 199(37): 2559-2570. doi: https://doi.org/10.1016/j.cma.2010.04.006

67. Brooks AN, Hughes TJ. Streamline upwind/Petrov-Galerkin formulations for convection dominated flows with particular emphasis on the incompressible Navier-Stokes equations. *Computer Methods in Applied Mechanics and Engineering* 1982; 32(1): 199-259. doi: https://doi.org/10.1016/0045-7825(82)90071-8

68. Hughes TJ, Franca LP, Balestra M. A new finite element formulation for computational fluid dynamics: V. Circumventing the babuška-brezzi condition: a stable Petrov-Galerkin formulation of the stokes problem accommodating equal-order interpolations. *Computer Methods in Applied Mechanics and Engineering* 1986; 59(1): 85-99. doi: https://doi.org/10.1016/0045-7825(86)90025-3

69. Elguedj T, Hughes T. Isogeometric analysis of nearly incompressible large strain plasticity. *Computer Methods in Applied Mechanics and Engineering* 2014; 268: 388-416. doi: https://doi.org/10.1016/j.cma.2013.09.024

70. Schröder J, Viebahn N, Wriggers P, Auricchio F, Steeger K. On the Stability Analysis of Hyperelastic Boundary Value Problems Using Three- and Two-Field Mixed Finite Element Formulations. *Comput. Mech.* 2017; 60(3): 479âĂŞ492. doi: 10.1007/s00466-017-1415-2

71. Lee CH, Gil AJ, Bonet J. Development of a cell centred upwind finite volume algorithm for a new conservation law formulation in structural dynamics. *Computers and Structures* 2013; 118: 13-38. Special Issue: UK Association for Computational Mechanics in Engineeringdoi: https://doi.org/10.1016/j.compstruc.2012.12.008

72. Bonet J, Bhargava P. A uniform deformation gradient hexahedron element with artificial hourglass control. *International Journal for Numerical Methods in Engineering* 1995; 38(16): 2809-2828. doi: https://doi.org/10.1002/nme.1620381608

73. Simo JC, Armero F. Geometrically non-linear enhanced strain mixed methods and the method of incompatible modes. *International Journal for Numerical Methods in Engineering* 1992; 33(7): 1413-1449. doi: https://doi.org/10.1002/nme.1620330705

74. Simo J, Armero F, Taylor R. Improved versions of assumed enhanced strain tri-linear elements for 3D finite deformation problems. *Computer Methods in Applied Mechanics and Engineering* 1993; 110(3): 359-386. doi: https://doi.org/10.1016/0045-7825(93)90215-J

75. de Souza Neto E, Peric D, Dutko M, Owen D. Design of simple low order finite elements for large strain analysis of nearly incompressible solids. *International Journal of Solids and Structures* 1996; 33(20): 3277-3296. doi: https://doi.org/10.1016/0020-7683(95)00259-6

76. Bonet J, Gil AJ, Wood RD. *Nonlinear Solid Mechanics for Finite Element Analysis: Statics*. Cambridge, UK: Cambridge University Press. 3rd ed. 2016.

77. Hughes TJR. *The Finite Element Method, Linear Static and Dynamic Analysis*. Englewood Cliffs, New Jersey: Prentice-Hall . 1987.

78. Malkus DS, Hughes TJ. Mixed finite element methods – Reduced and selective integration techniques: A unification of concepts. *Computer Methods in Applied Mechanics and Engineering* 1978; 15(1): 63-81. doi: https://doi.org/10.1016/0045-7825(78)90005-1

79. Hesthaven JS, Warburton T. *Nodal discontinuous Galerkin methods: algorithms, analysis, and applications*. Springer Science & Business Media . 2007.

80. Williams D, Shunn L, Jameson A. Symmetric quadrature rules for simplexes based on sphere close packed lattice arrangements. *Journal of Computational and Applied Mathematics* 2014; 266: 18-38. doi: https://doi.org/10.1016/j.cam.2014.01.007

81. Witherden F, Vincent P. On the identification of symmetric quadrature rules for finite element methods. *Computers & Mathematics with Applications* 2015; 69(10): 1232 - 1241.

82. Cook RD. Improved Two-Dimensional Finite Element. *Journal of the Structural Division* 1974; 100(9): 1851-1863. doi: 10.1061/JSDEAG.0003877

83. Sze K, Liu X, Lo S. Popular benchmark problems for geometric nonlinear analysis of shells. *Finite Elements in Analysis and Design* 2004; 40(11): 1551-1569. doi: https://doi.org/10.1016/j.finel.2003.11.001

84. Poya R, Gil AJ, Ortigosa R. A high performance data parallel tensor contraction framework: Application to coupled electro-mechanics. *Computer Physics Communications* 2017; 216: 35 - 52. doi: https://doi.org/10.1016/j.cpc.2017.02.016

85. Schneider T, Hu Y, Gao X, Dumas J, Zorin D, Panozzo D. A Large-Scale Comparison of Tetrahedral and Hexahedral Elements for Solving Elliptic PDEs with the Finite Element Method. *ACM Trans. Graph.* 2022; 41(3). doi: 10.1145/3508372

86. Chen R, Weber O. GPU-accelerated locally injective shape deformation. *ACM Trans. Graph.* 2017; 36(6): 1 - 13. doi: 10.1145/3130800.3130843

87. Li M, Ferguson Z, Schneider T, et al. Incremental Potential Contact: Intersection-and Inversion-Free, Large-Deformation Dynamics. *ACM Trans. Graph.* 2020; 39(4). doi: 10.1145/3386569.3392425